3D Islet Assay Development and SAR of Chromenones for Beta-Cell Replenishment

by

Sean McCarty

A dissertation submitted in partial fulfillment
of the requirements for the degree of
Doctorate Of Philosophy
(Medicinal Chemistry)
in the University of Michigan
2023

Doctoral Committee:

Professor Zachary J. Sexton, Co-Chair
Professor Martin Clasby, Co-Chair
Professor Tim Cernak
Professor Peter J. Scott

Sean M. McCarty

smmccar@umich.edu

ORCID iD: 0000-0002-6542-0474

Dedication

This dissertation is dedicated to the person I have most looked up to in life. She was a pioneer of her time, pushing beyond the boundaries of society and of herself to ambitiously pursue life. She courageously undertook new opportunities to help and improve the lives of others all around her. Her mark on this world will far outlive herself and I hope to live a life as fulfilling as the one she has made for herself. To formidably intelligent, caring, and inspiring matriarch. To my grandmother, Margaret McCarty, know that your spirit will always live on in the work that I, and the rest of your family, continue to pursue.

Acknowledgements

While this dissertation is dedicated to my grandmother, who promised she would live long enough to see me graduate, the most important people to acknowledge in its completion are my parents. It is because of them that I was able to have the experiences that led me down this path, and because of their sacrifices that I have had the opportunities to embark on those experiences. Furthermore, they have supported me even as I have made decisions that they may not have understood at the time.

Next, we need to acknowledge that no one gets to where they are on their own. For me specifically, a vast network of people has helped me get here. Thank you, Dr. Jonny Sexton, for being my advisor and mentor over the last five years. Thank you, Dr. Martin Clasby, for helping mentor me through the chemistry aspects of this project. I am also grateful for the mentorship my other committee members, Dr. Cernak and Dr. Scott, have provided me with. I want to thank Mother Tracey for managing and facilitating our lab and for guiding and supporting me as I have grown during this process. Just as importantly, thank you to the now Dr. Jesse Wotring and Dr. Charles Zhang, to the future Dr. Sophia Meyer and Dr. Khadija Shafiq, and Dr. Reid Fursmidt, and to Ben Halligan. I loved working alongside all of you over the course of this PhD and you all have made the experience a truly once in a lifetime one. A special thank you to my fiancée, Abby, for pushing me to be the best version of myself and for supporting me through the last two years of this journey.

And finally, I would like to acknowledge all students who have come before me, on which this work is built. To those who come after me, I hope you can find inspiration in my work and a word of advice. While our work is remembered by our successes, your journey will be defined by mediocrity and how you work through it. When you've completed your experiments to the best of your ability, an unwanted result is not a failure. Null and unwanted results are expected; however, the only true failures in research are repeating your mistakes instead of learning from them. Each result a step forward, a path explored, and possibly a sign to look in a different direction. If it were easy, someone else would have already done it.

Table of Contents

List of Tables

List of Figures

List of Abbreviations

2D	two-dimensional
3D	three-dimensional
AF	autofocus
Arx	Aristaless related homeobox
ATP	adenosine triphosphate
AUC	area under the curve
BSA	bovine serum albumin
CDK	cyclin-dependent kinases
cDNA	copy DNA
CK1	casein kinase 1
CLK	cdc-like kinases
CMGC	kinase family composing of CDKs, MAPKs, GSKs, and CLKs
cmpd	compound
CO2	carbon dioxide
COL1A1	collagen type 1 alpha 1
DAPI	4′,6-diamidino-2-phenylindole, a blue-fluorescent DNA stain
DCM	dichloromethane

DIO	diet induced obesity
Dmnt1	DNA (cytosine-5)-methyltransferase 1
DMSO	dimethylsulfoxide
DYRK1A	dyal specificty tyrosine-phosphorylation-regulated kinase 1A
E47	transcription factor 3
EDU	5-Ethynyl-2′-deoxyuridine
ELISA	enzyme-linked imunosorbent assay
ER	endoplasmic reticulum
EtOAc	Ethylacetate
EtOH	ethanol
FBS	fetal bovine serum
FITC	fluorescein isothiocyanate
FLuc	Firefly luciferase
FUCCI	fluorescence ubiquitination-based cell cycle indicator
GCG	Glucagon
GFP	green fluorescent protein
GHRL	ghrelin and obestatin prepropeptide
Gluc	Gaussia luciferase
GSIS	Glucose stimulated insulin secretion
GSK	Glycogen synthase kinase
GSK3B	Glycogen synthase kinase-3 beta
HBA	hydrogen bond acceptor

HBD	hydrogen bond donor
HCS	High-content screening
HEPES	4-(2-hydroxyethyl)-1-piperazineethanesulfonic acid
Hex	hexanes
HNF	Hepatocyte Nuclear Factor
HPLC	High pressure liquid chromatography
hr	hour
HTRF	Homogeneous Time Resolved Fluorescence
HTS	High-throughput Screening
ID	identification
IE	islet equivalent
IFN	interferon
IL-1	interluken 1
Ins	insulin
INS1	insulin gene
iPSC	induced pluriupotent stem cells
Ki67	Antigen Kiel 67
KNN	K-nearest neighbors algorithm
KRT19	Keratin19
LC	liquied chromatography
luc	luciferase
MALDI-TOF	Matrix Assisted Laser Desorption/Ionization-Time of Flight

MAP4K4 mitogen-activated protein kinase kinase kinase kinase 4

MAPK mitogen-activated protein kinase

MDRC Michigan Diabetes Research Center

MeOH Methanol

mg milligram

min minute

MIP Maximum intensity projection

ML Machine Learning

mL milliliter

mM millimolar

MOA mechanism of action

MS mass spectrometry

MW molecular weight

NA not available

NEAA non-essential amino acids

NeuroD1 neuronal differentiation 1

NFkB nuclear factor kappa b

NIH National Institute of Health

Nkx6.1 NK-6 homeobox 1 gene gene

nLuc nanoluciferase

oC degrees Celcius

P/S penstrep

PBS phosphate buffered saline

PCA	principle component analysis
PDX1	pancreatic and duodenal homeobox 1 gene
PK	pharmacokinetics
ppm	parts per million
PPY	pancreatic polypeptide gene
PRSS1	Protease, serine 1 gene
Q-TOF	quadrapole time-of-flight
RFP	red fluorescent protein
RLuc	renella luciferase
Rot	rotatatable bonds
RPMI	Roswell Park Memorial Institute
RT	Room temperature
SAR	structure-activity relationship
SST	somatostatin
T1D	Type-1 Diabetes
T2D	Type-2 Diabetes
T2DM	Type-2 Diabetes Mellitus
TAg	T antigen
TNF	tumor necrosis factor
TR-	
FRET	Time-resolved fluorescence
t-SNE	t-distributed Stochastic Neighbor Embedding
TXNIP	thioredoxin0interacting protein

ug	microgram
uL	microliter
uM	micromolar
UM	university of michigan
UPLC	ultrahigh pressure liquid chromatography
VGF	nerve groth factor inducible
via	viability
YFP	yellow fluorescence protein
Z'	Z prime

Abstract

Diabetes poses a global health crisis affecting individuals across age groups and backgrounds, with a prevalence estimate of 700 million people worldwide by 2045. Current therapeutic strategies primarily rely on insulin therapy or hypoglycemic agents, which fail to address the root cause of the disease - the loss of pancreatic insulin-producing beta-cells. Therefore, bioassays that recapitulate intact islets are needed to enable drug discovery for beta-cell replenishment, protection from beta-cell loss, and islet-cell interactions. Standard cancer insulinoma beta-cell lines MIN6 and INS-1 have been used to interrogate beta-cell metabolic pathways and function but are not suitable for studying proliferative effects. Screening using primary human/rodent intact islets offers a higher level of physiological relevance to enhance diabetes drug discovery and development. However, the three-dimensionality of intact islets have presented challenges in developing robust, high-throughput assays to detect beta-cell proliferative effects. Established methods rely on either dissociated islet cells plated in 2D monolayer cultures for imaging or reconstituted pseudo-islets formed in round bottom plates to achieve homogeneity. These approaches have significant limitations due to the islet cell dispersion process. To address these limitations, we have developed a robust, intact pancreatic islet imaging platform in 384-well format that is capable of detecting diabetes-relevant endpoints including beta-cell proliferation, chemoprotection, and islet spatial morphometrics. We were then able to apply our method to a preliminary *in vivo* study of a new scaffold for beta-cell modulation. Islets were isolated from the pancreata of mice after a week of exposure of our compound, GNF-9228. This method proved to be a drastic improvement over classical histological analysis for *in vivo* beta-cell proliferation and encouraged us to pursue a structure-

activity relationship campaign to improve the physical properties of our lead compound. Subsequent work led to the evaluation of over seventy compounds in bio various assays. Additionally, we were able to leverage existing scRNA seq data from Type 2 diabetes samples to evaluate our compound’s effects on the human kinome.

Chapter 1
High Throughput Assays for the Discovery of Small Molecule Modulators of Beta-Cell Function

1.1 Introduction

Diabetes is a global health crisis affecting over 537 million people worldwide. It is quickly becoming one of the most pressing health concerns of our time. By 2030, experts predict that more than 643 million people could be diagnosed with pre-diabetes or insulin-dependent type-II diabetes mellitus. The cost of dealing with diabetes-related health problems is currently approaching a staggering one trillion dollars globally. In the United States, on average, each person impacted by diabetes spent about $11,779 on related health expenses in 2021.[1] When it comes to managing T2D, current therapeutic strategies combine a mix of lifestyle changes and medications, including both non-insulin drugs and insulin treatments. These approaches help control blood glucose homeostasis, but they do not address the loss of beta-cell mass, the root cause of the disease.

The beta-cell performs a distinct physiological role as the sole cell type within the body to secrete insulin. In concert with the alpha cells, the endocrine cell system within the pancreas governs glucose homeostasis. The progression of T2D is correlated with an average of 30% loss in beta-cell mass (24-60%), which ultimately leads to the disruption of glycemic regulation.[2] The precise mechanistic underpinnings leading to this cellular attrition have only been partially

elucidated. The prevailing hypothesis suggested that beta-cell loss emanated from apoptosis, triggered by the stress of heightened insulin production to overcome the resistance posed by insulin-resistant tissues and glucolipotoxicity.[3] However, recent advancements have unveiled an alternative perspective; suggesting that a subset of the diminished beta-cell population maybe undergoing a regressive transition toward an fetal state, marked by an inability to produce and secrete insulin.[4,5] Significant effort has been made to discover and develop drug-like molecules with the ability to protect or restore beta-cell mass and function.

The implementation of high throughput screening (HTS) has been pivotal in the search for these agents. Within HTS, expansive libraries of chemical compounds are subjected to rapid evaluation through molecularly-targeted or phenotypic bioassays. These chemical libraries, derived via parallel or combinatorial synthesis, can encompass millions of compounds. Execution of these assays occurs within standardized well plates containing 96, 384, or 1536 wells. Although the adaptation to a reduced scale yields a lower cost per data point, it requires a higher level of precision as volumes decrease to the order of a few microliters per well. In tandem with the miniaturization of bioassays to accommodate the plate format, the integration of automation emerges as an indispensable tool, affording enhanced reproducibility and expediting logistics management.[6] While limited in number, several insulin expressing and glucose-responsive cell lines have been developed, but a select set of immortalized rodent insulinoma cell lines have facilitated diabetes screening in general.[7,8] This review aims to summarize the current methods employed in cell-based high throughput screening for small molecule modulators of beta-cell mass and function.

1.2 Luciferase Based Viability Assays

Luciferase assays, a heavily used assay technology, are regularly leveraged to explore gene expression in reporter cell systems, assess cell viability, and explore other relevant endpoints. Highlighting its widespread use, nearly 22% of the 4,000 assays recorded in the PubChem database utilize the luminescence detection method, a statistic consistent with reports over a decade ago.[9] The key to this assay is the luminescence-producing oxidation of luciferin by the luciferase enzyme – a reaction necessitating ATP, thereby serving as an effective measure of cell viability. The simplicity of luciferase assays is what makes it a prime choice for HTS.

Research groups have adopted luciferase assays to identify compounds that alter the viability of beta-cells. In one example from 2009, a modified mouse beta-cell line, R7T1, was used to screen about 850,000 compounds.[10] The cells were immortalized using the SV40 T antigen oncoprotein (TAg) which induced cell cycle arrest upon tetracycline withdrawal. This system helped pinpoint compounds that could trigger the reentry into the cell cycle and proliferation, determined via a CellTiter-Glo readout. Results from this screen led to the subsequent discovery that a combination of DYRK1A and GSK-3B inhibition can stimulate beta-cell proliferation.[11,12]

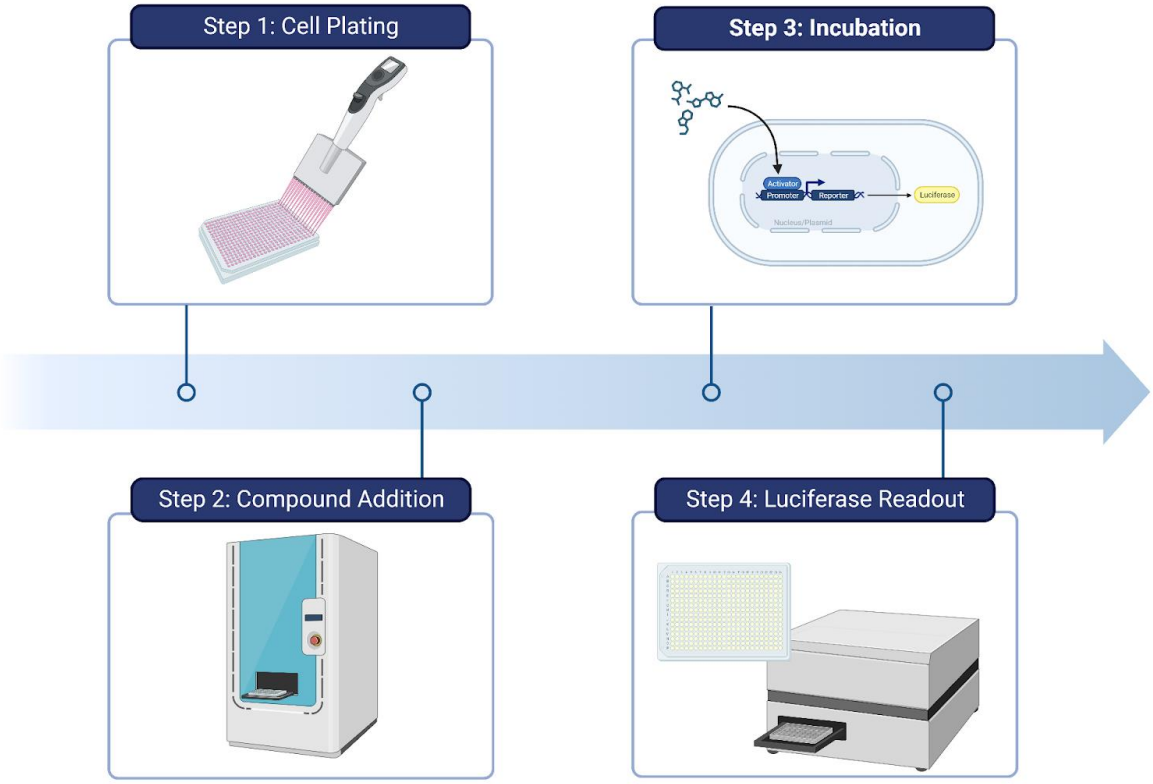

Figure 1. Workflow for high-throughput luciferase assays. **Step 1:** Cells are plated in 384 or 1536-well plates. **Step 2:** Compounds are added to each well using a liquid handling device. Often controls are present in the first and last columns of each plate. **Step 3:** Cells are allowed to incubate with the compounds for an optimized amount of time to allow for changes in luciferase expression. **Step 4:** Luciferase content is quantified using a kit and a plate reader. Created with BioRender.com.

It is theorized that the high level of circulating glucose and lipids, persistent over the course of T2D, induces beta-cell apoptosis.[13] Recent research endeavors have constructed a cell based glucolipotoxicity model to facilitate screening for protective molecules.[14,15] In this innovative assay, immortalized beta-cell lines are exposed to high concentrations of glucose exceeding 25 mM and simultaneously challenged with palmitate. Conveniently palmitate can be pre-complexed with fatty acid free BSA at various ratios for seamless addition during screening. The primary readouts for this assay were cell viability, using either an XTT assay or

CellTiterGlo. Miniaturization to a 1536-well format has permitted the screening of over 300,000 compounds.

In the context of Type 1 Diabetes (T1D), a condition characterized by beta-cell loss through an autoimmune mediated pathway, a similar approach was applied to establish an HTS model. A cytokine induced beta-cell apoptosis model was developed using an immortalized rat insulinoma cell line, exposed to a cocktail of cytokines. These cells were exposed to a cocktail composed of 10 ng/mL IL-1, 50 ng/mL IFN-gamma, and 25 ng/mL TNF-alpha; a mixture known to induce beta-cell death. Following the addition of compounds and a 48-hour incubation period, beta-cell viability was measured using CellTiter-Glo.[16] This pilot screen, comprising of 2240 compounds, led to the understanding that GSK-3B inhibitors were also effective at preventing beta-cell apoptosis.

A more targeted approach for luciferase screening involves the creation of a genetically encoded promoter reporter system. This system, with the luciferase sequence alongside with a target gene promoter, can be integrated into cells. When these cells express the target gene, they concurrently synthesize luciferase. The subsequent light emission observed when luciferin is added to these cells offers a measurement of the gene expression level. Two examples that have been used in this fashion for high throughput screening in the context of diabetes are MYC and Nkx6.1.

The MYC proteins have long been recognized as crucial drivers of cell growth. HepG2 cells, a hepatocyte line, were transfected with a luciferase reporter under the control of the

human MYC promoter. While HepG2 cells aren't an endocrine cell line, they were chosen because they yielded the most robust luciferase responses. Among 100,000 compounds screened, only 86 made it to testing in primary rat islets. Ultimately, Harmine, a DYRK1A inhibitor that has since gained prominence in the field, was the sole compound from the screen to validate in an islet assay.[17]

A cDNA screen conducted in a hamster insulinoma cell line unveiled the impactful role of homeobox genes on beta-cell function.[18] Further investigation efforts focused on the homeobox domain protein Nkx6.1, revealing its influence on beta-cell replication and its regulation of glucose-stimulated insulin secretion (GSIS). Additionally, it was found to promote beta-cell survival via the production of the VGF peptide.[19–21] Leveraging this promising target, a screen encompassing 630,000 compounds was executed, utilizing a luciferase reporter for the VGF promoter in the 832/13 rat insulinoma cell line.[22] This extensive screening process yielded three lead molecules, each containing the ability to induce beta-cell proliferation, enhance GSIS, and protect against apoptosis.

While luciferase-based screening is cost effective and efficient for high throughput screening, it is widely acknowledged for its susceptibility to assay interference. One study investigating 360,000 compounds in PubChem found that 12% inhibited FLuc.[23] Likewise, compounds dubbed "luciferase stabilizers" can increase the luminescence signal through the formation of stable adducts with ATP, leading to false positives.[24] Small molecules that have linear, planar structures have the highest likelihood of causing assay interference. In this light, newer analogs of Fluc, such as NLuc, RLuc, or TLuc, exhibit reduced interference. Meanwhile,

it's worth noting that cytosolic ATP levels have been observed to increase during apoptosis, introducing another potential source of interference in luciferase viability assays.[25] To mitigate such challenges, carefully choosing orthogonal assays that do not rely on a luciferase readout is key, as they provide an effective method to filter out assay interference compounds. Often times, simply using the same screening method but with the utilization of ATP-independent RLuc can be sufficient to filter out both false positives and negatives in expression assays, thus enhancing the efficacy and accuracy of the screening process.[26] In fact, the Dual-Luciferase Reporter Assay uses sequential reads from FLuc and RLuc in the same cell lysate to overcome potential assay interference.[27] The development of NanoLuc has provided a luciferase that is smaller in size, drastically brighter, and less prone to compound interference.[28]

1.3 Glucose Stimulated Insulin Secretion (GSIS)

The transition from healthy to diabetic involves the deterioration of several beta-cell functions, one of which is the first phase insulin release response following postprandial increase in blood glucose.[29] This was underscored by two longitudinal studies that identified changes in acute insulin response as the primary determinant of glucose tolerance.[30,31] However, until recently, large-scale screening for molecules that can modulate this process has been exceptionally difficult. A typical GSIS assay requires a starvation period before introducing glucose. This, coupled with multiple wash steps, makes this assay system particularly cumbersome for high-throughput screening. After glucose stimulation, insulin levels in the supernatant are measured; however, there are a limited number of cell lines that are glucose responsive , many of which lose that ability over time which poses an added difficulty.[31] Historically, quantification of insulin relied on ELISA assays. While highly sensitive, they are time consuming, expensive and can have issues with high variability. Nevertheless, recent

advances in proximity luminescence and fluorescence technologies have led to the emergence of high throughput, cost effective assay kits to enable higher-throughput interrogation of insulin production and secretion. Another challenge in performing high quality GSIS assays is the avoidance of cell disruption/lysis during sampling of the media for insulin quantitation. Beta-cells contain large quantities of insulin and only secrete a small fraction; therefore any cell disruption can cause significant increases in insulin content. Therefore, slow and careful aspiration of media from cell plates, ideally using liquid handling robotics, can greatly reduce noise in the insulin readout by avoiding cell disruption.

An improvement in assay technologies is the use of homogeneous "mix and read" assays where reagents are added, and the signals are detected directly. Homogeneous proximity biosensor assays have become a prominent tool for insulin detection in GSIS experiments. One notable tool that has emerged is a luminescence-based assay kit known as AlphaLisa(Perkin Elmer). With this assay technology, donor and acceptor beads are coated with anti-analyte antibodies. Upon simultaneous binding of both beads to the analyte, in this case insulin, they are brought into proximity. The subsequent activation of the donor beads using a 680 nm wavelength triggers a singlet oxygen reaction sequence with the nearby acceptor bead, which in turn emits light at 620 nm. Notably, this system can be miniaturized to require only 1 uL of analyte and is compatible with a 1536-well format. Despite its remarkable sensitivity, the AlphaLisa encounters certain limitations. The primarily limitation is its irreversible chemical reaction which leads to diminished signal upon sequential reads and may suffer interference from ambient light.[32]

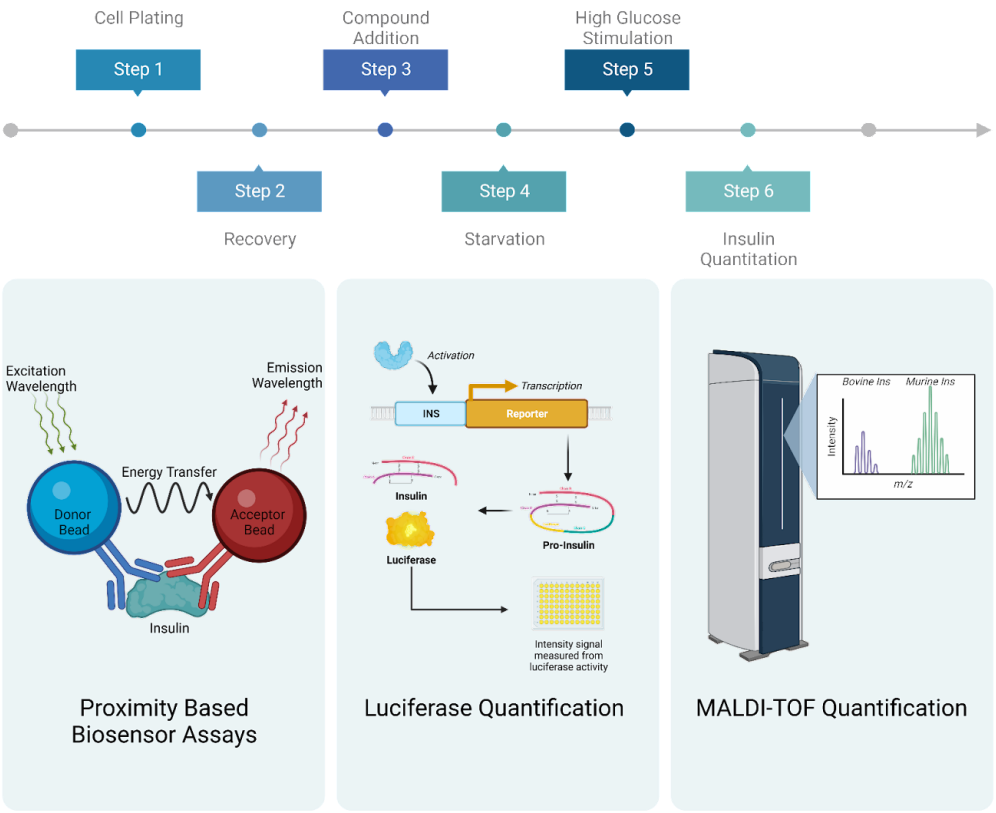

Figure 2. Top: General workflow for GSIS assays. Cells are plated in 384-well format and let recover, generally overnight. Compounds are added and the cells are allowed to incubate for an optimized amount of time. Cells are then starved of glucose before being stimulated with a buffer containing a high concentration of glucose. The buffer is removed, and various methods can be used to quantitate the amount of insulin released during glucose stimulation. **Bottom:** The three main methods of high-throughput insulin quantification. Created with BioRender.com.

An alternative approach is offered by time-resolved fluorescence resonance energy transfer (TR-FRET) assays. With execution and cost similar to AlphaLisa, these assays implement a proximity-based fluorescence readout, as opposed to luminescence. The adoption of long-lived fluorophores minimizes background noise stemming from buffers, proteins, or chemical compounds present in the sample mixture. Several commercially available kits offer this technology such as Perkin Elmer's Lance, Invtrogen's Lanthascreen, and CisBio's HTRF platform. Particularly intriguing is the potential to use the HTRF assay system in a 3456-well format, paving the path for ultra-high-throughput screening campaigns.[33] However, it is

important to consider that these technologies are not entirely free form assay interference. Such disturbance primarily leads to a reduction in assay signal due to mechanisms including absorbance, quenching, light capture, and disruption of affinity components. Overcoming these may require deploying strategies like product spiking or orthogonal assays to mitigate interferences.[34]

In a concerted effort to drive down the cost of insulin secretion assays, several groups have pioneered similar luciferase-based insulin secretion assays. The defining feature of these systems is the fusion of *Gaussia* luciferase and the C-peptide portion of mouse proinsulin, based on previous work where GFP was fused with the proinsulin protein to facilitate imaging.[35] Intrinsic to the insulin secretion process, the C-peptide of mouse proinsulin is cleaved within beta-cell vesicles. It is then co-released with insulin during exocytosis. Since C-peptide and insulin are released concurrently, a luminescence readout can be achieved using the supernatant. Cell lines from both mouse (MIN6) and rat (INS-1E) that stably expressed the reporter were developed, with rigorous validation efforts confirming a strong correlation between luciferase activity and insulin content.[36,37] Expanding the reach of this method, the system was successfully miniaturized to 1536-well format. This was achieved by performing the glucose starvation and wash steps while the cells were suspended, prior to plating. One example of the implementation of this system is the screening of more than 1100 plant extracts for their ability to modulate insulin secretion.[38]

The recent work of Delannoy et al. presents a novel approach for quantitative high-throughput GSIS, employing the use of Matrix Assisted Laser Desorption/Ionization-Time of

Flight (MALDI-TOF) mass spectroscopy.[39] This innovative procedure requires samples to be spiked with an internal standard of bovine insulin to quantitate and normalize insulin content. Following dilution and spiking, small sample quantities are dried onto a 384 steel MALDI target and subsequently analyzed. The advantage of this method lies in its ability to directly detect insulin, thereby circumventing potential complications such as incomplete antigen binding or interference from compounds within the detection assay. Interestingly, experimental results from both ELISA and MALDI-TOF were nearly identical. While several preparatory steps are required prior to mass spectrometry analysis, these stages are brief and overall assay efforts are comparable to those required for luminescence or fluorescence proximity assays. Such innovations underscore the potential for efficient, high-throughput interrogation of GSIS dynamics. However, it's noteworthy that these assays continue to be single endpoint assays instead of multiplexed assays, even though the cells hold potential for imaging or other readouts after the GSIS is complete.

1.4 High Content Screening

Multiplexed imaging based phenotypic cell screening, also known as "high-content screening," is designed to extract a wealth of information from cells through the use of fluorescent probes and automated fluorescence microscopy. With significant advancements in the field, this approach has evolved where screens can be conducted in a completely automated and quantitative manner, providing robust results capable of measuring multiple endpoints including biomarker intensity, spatial distribution of signals and morphologic endpoints.[40] The primary goal of this approach is to extract as much information as possible from cell populations within each experiment. Where earlier HCS efforts include one or two image-based features, the

advent of cell painting and availability of the open source image/data analysis software, such as CellProfiler, CellPose and Knime, have expanded the information content in screening to encompass hundreds-to-thousands of features.[41,42] This technique is particularly advantageous for targeting subpopulations within cell systems to enable image cytometry. Assays focusing on cell cycle, infection, and differentiation have shown robust results, leading to their adoption within the diabetes research field.

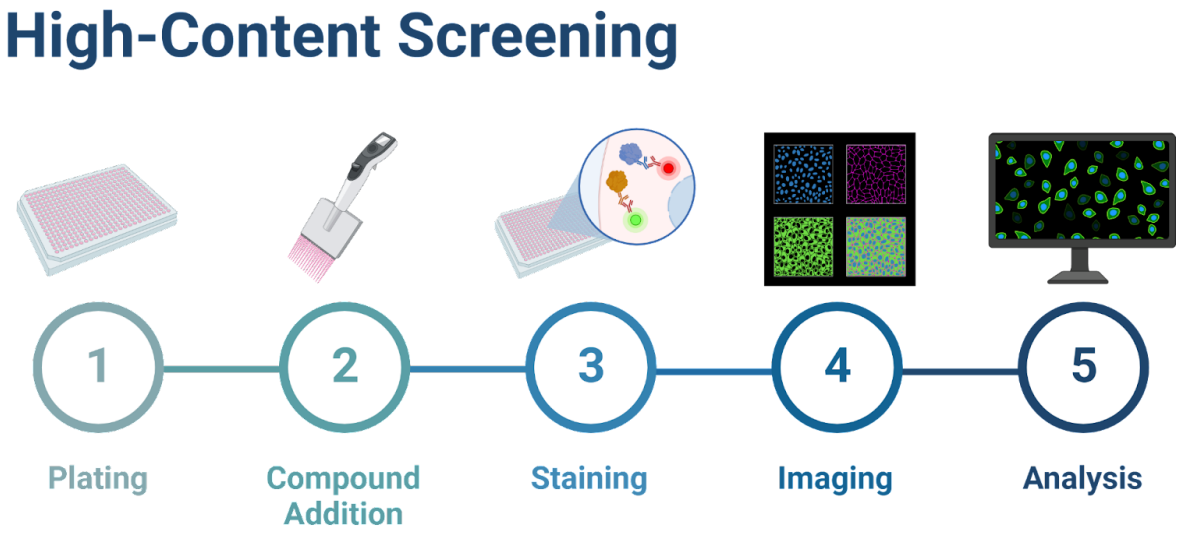

Figure 3. General workflow for HCS. **Step 1:** Cells are plated in 384-well format. **Step 2:** compounds are added to each well with controls on each plate. **Step 3:** Cells are fixed, permeabilized and stained with various dyes and antibodies to illuminate proteins or cellular compartments of interest. **Step 4:** Multiple fluorescent channels are imaged using specialized automated high throughput microscopes. **Step 5:** Image analysis is performed to segment individual cells, quantify intensities, textures, and morphologic characteristics of the objects of interest. Created with BioRender.com.

In conducting a high-content screen, it is critical to ascertain the reliability and robustness of the assay. This is typically assessed through a statistical coefficient called Z-prime (Z').[43] The Z' offers a measure to evaluate the quality of a biological assay factoring in both the assay window and variability of the data. This includes consideration of background and positive controls. The mathematical formulation of Z' equals one minus the absolute value of ratio of the

difference between the standard deviations of the controls and the difference of their means. It is important to note that the accuracy of this metric degrades if hit rates exceed 20% of the samples. Meanwhile, the B-score plays a crucial role as a normalization method in high throughput experiments.[44] This method is designed to handle spatial bias and plate/batch effects. For instance, a common plate effect can be the evaporation of media in the outer wells, leading to a decrease in cell viability in those wells. Normalization is achieved by comparing the measurement of each well to the median of its neighboring wells within the same plate.[45] One benefit of high-content multivariate assay endpoints is the ability to generate machine learning (ML) models that can significantly enhance the robustness of the assay. These methods generally rely on training machine learning random forest models against the positive and negative controls in the plate enabling scoring of compound treated wells for robust quantitation of efficacy with simultaneous detection of cytotoxicity. We have previously described a pragmatic approach to these general methods in the NIH Assay Guidance Manual as a resource to help guide the implementation of ML models in the context of high-content screening.[46] This approach also streamlines the integration of high-dimensional screening data into conventional high-throughput screening data analysis paradigms intended for univariate plate reader-based compound screening.

An early application of imaging in diabetes drug discovery was in the search for Hepatocyte Nuclear Factor (HNF) 4a agonists. This screen took advantage of T6PNE cells, a line originating from human fetal islets and engineered to express PDX1, NeuroD1, and E47.[47,48] The cells were further adapted for high throughput screening through the incorporation of a lentiviral vector. This vector was designed to express Green fluorescent protein (GFP) under the control of

the human insulin promoter. In this screening methodology, tamoxifen was employed to impair insulin expression, and the objective was to identify compounds which rescued insulin production. Following a two-day incubation, the cells were imaged using a high throughput microscope. The primary parameter analyzed from the images was the intensity of the GFP; however, this assay ultimately suffered low Z' scores due to variability in GFP expression.[48]

Through the deployment of a dual reporter system of Ins1/GFP and Pdx1/red fluorescent protein (RFP) in a high-content screen, a link was identified between sodium channel inhibition and increases in insulin transcription where the multiplexed readout delineates the "maturation" of the beta-cells. Cells expressing high Pdx1 but low Ins1 expression were "immature" while cells expressing high Pdx1 and high Ins1 were "mature".[49] This screen was carried out in 96-well plates employing a MIN-6 cell line. Cells underwent imaging via a live-cell imaging on a Zeiss 200M microscope. Variability was observed in the outer rows, which was corrected through B-score normalization.[50] The study took advantage of a library of 1120 compounds that contained many off-patent drugs. The well-documented mechanism of action (MOA) of these known drugs enhances hypothesis generation when used in HCS screening.[51] Regrettably, due to excessive variability, the assay proved incompatible with primary human islets.

A proposed strategy to restore beta-cell mass involves the conversion of other endocrine cells to beta-cells. Such a process has been confirmed through lineage tracing in mouse models following beta-cell loss.[51] Particularly, when examining alpha cells, it was found that simultaneous loss of of Dnmt1 and Arx genes led to the expression of Insulin, Pdx1, and Nkx6.1 genes within those same cells.[52] To identify compounds capable of inducing this transformation,

a Min6 line was manipulated to overexpress Myc-tagged ARX which lead to the repression of their normal beta-cell genes. Cells were plated in 384-well format, and compounds were introduced with the goal of repressing ARX expression and boosting insulin production. Outcomes were determined by fluorescent staining of insulin and Myc-ARX, followed by high-throughput imaging.[53]

The scarcity of human-derived beta-cell lines has necessitated the use of cadaveric human islets as a model for diabetes drug discovery due to their physiological relevance. It has been well established that islets sourced from donors remain viable in culture and are capable of demonstrating islet cell proliferation and normal insulin secretion dynamics.[54] Yet, their three-dimensional structure poses challenges for rapid imaging and analysis. The most common approach begins with dispersal of isolated islets into a single-cell suspension exhibit high viability under specific culture conditions.[55,56] To enable the use of these cells in the 384-well screening environment, plates were initially coated with an extracellular matrix formed by HTB-9 cells, a bladder carcinoma line. After these cells secreted matrix factors, they were removed using ammonium hydroxide, and dissociated human islet cells were plated on top of the matrix.[57] Without this extracellular matrix, dispersed islet cells have very low attachment strength and tend to detach over the course of the protocol.[58] Additionally, the matrix allowed dispersed islet cells to be cultured for up to seven days. The cell populations were examined via imaging, applying a combination of glucagon, c-peptide, and Ki67 staining. A library of 1280 compounds was screened in cells from three different donors.[59] However, one crucial factor to note is variability in the beta-cells between donors; this is a factor that should be considered for optimization in large-scale screening endeavors.

1.5 *In Vivo* Screening

The zebrafish has emerged as an interesting model for in-vivo phenotypic screening, bridging the gap between the simplicity of in-vitro cellular models and the expense of in-vivo mouse models. Due to their optical transparency, ability to absorb compounds added in their environment, and compatibility with 96-well plates, zebrafish embryos are ideally suited for high-throughput screening.[60] Several studies have utilized zebrafish in screens to identify pathways leading to the induction of beta-cell proliferation. In one study, the use of YFP expression, driven by the insulin promoter, and RFP expression, driven by the somatostatin 2 promoter, allowed for the differentiation of beta-cell production. Moreover, the inclusion of RFP could facilitate the identification of compounds that selectively increase beta-cell mass.[61] To further explore beta-cell dynamics, two other studies leveraged variations of fluorescent ubiquitination-based cell cycle indicator (FUCCI) technology. The core of FUCCI features of a plasmid that containing GFP and RFP fused to proteins unique to G1 or S/G2/M phases.[62] In one approach, this system was placed under the control of the insulin promoter, thus allowing the visualization of proliferating beta-cells within the zebrafish pancreas.[63] The alternative approach replaced the fluorescent proteins with nLuc for a luminescence based readout upon addition of the appropriate substrate.[64] Both of these techniques deploy a few larvae per well of a 96-well plate for compound exposure. The zebra fish can be anesthetized with Tricaine, allowing for high throughput imaging and image analysis-based quantitation.[65]

1.6 Microtissues & Primary Islets

While immortalized or primary cell monolayers have significantly contributed to diabetes drug discovery, they fall short in replicating the complexity of the pancreatic islet. Moreover, the

widespread use of rodent-derived cell lines has led to a more comprehensive understanding of the intracellular signaling pathways steering rodent beta-cell proliferation than that of human beta-cells.[66] On the other hand, human islets are small, three-dimensional structures composed of five main endocrine cell types, interspersed through the islet along with other non-endocrine cell types.[67] Their 3D structure makes drug penetration, as well as imaging and analysis, a considerable challenge. Microscopy of intact microtissues often involved mounting them on glass slides and imaging on low throughput confocal microscopes, demanding significant time and effort. Nonetheless, recent advances in confocal microscopy have facilitated high-content imaging and analysis of single-cells in 3D structures such as pseudoislets or intact primary islets.

One strategy to address low drug penetration involves dissociating islets to single cells prior to compound or transgene vectors treatment. These cells are then reaggregated into islet-like structures often referred to as "pseudoislets".[68,69] Pseudoislets reestablish gap junctions and maintain GSIS similar to native their native counterparts. They also bring the added advantage in screening reducing variability in size and enhancing uniformity and cellular composition.[70,71] Originally, pseudoislets were formed in bulk using the "hanging-drop" method, a labor-intensive process which involved suspending 30 uL drops, containing dispersed endocrine cells, upside-down in culture dishes.[72] However, a modern adaptation of this method employs round-bottom ultra-low attachment 384-well plates to accomplish reaggregation.[73] This results in pseudoislets that can be maintained in culture for up to 4 weeks. The utilization of round-bottom plates ensures uniformity in pseudoislets position across all wells, thereby facilitating rapid high-resolution imaging. Staining using DAPI, Nkx6.1, and EDU allows for the assessment of beta-

cell proliferation. Interestingly, this method could be multiplexed with GSIS before fixation, accommodating a multi endpoint assay.[74] While this system provides a more physiologically accurate model than monolayer cultures, the generation of only one islet per well significantly hampers throughput. Additionally, because the pseudoislets are not attached to the microwell plate, fixation and staining that requires multiple additions and wash steps can lead to the loss of pseudoislets further hampering screening efforts.

While the uniformity of pancreatic microtissues removes variability, it also establishes a model that is further removed from physiological relevance. The creation of these microtissues intentionally destroys the original size, ratio, and organization of cells within islets. Although the heterogeneity of islets presents some challenges, the primary hurdle is their small size relative to the surface area at the bottom of the microplate wells. High-resolution imaging of an entire well for detailed images of islets would require a tremendous amount of time and a majority of images would be empty. Conversely, low-resolution imaging to identify areas that contain islets would expedite the process but sacrifice detail within the islets. A solution to this problem was addressed by the advent of a two-pass imaging technique. In this method, each well is imaged at low-resolution, the location of multiple islets is determined via image analysis, and the location data is fed back to the microscope to facilitate high-resolution second pass imaging where a single islet is centered within a field. Furthermore, coupling the multiplexed staining of Nkx6.1, glucagon, and Ki-67 with machine learning analysis enabled detection of islet cell proliferation and analysis of islet spatial morphometrics at the single-cell level.[75]

Recent advances regarding induced pluripotent stem cells (iPSCs) have streamlined their generation but expanded their accessibility to research labs. While differentiating IPSCs into pancreatic beta-cells can be a complex and time-consuming process, packed with various combinations of growth hormones and signaling molecules, it offers advantages over cadaveric harvesting.[76] Specifically, it ensures greater control over genetic diversity, age, and overall health of the islets.[77] Furthermore, iPSC-derived islets generated in either a planar or 3D scaffold are notably similar to native islets; they are glucose responsive and display a mix of insulin and glucagon expressing cells.[78] The ability to development and sustain a source of lab-grown that are physiologically relevant islets is a significant breakthrough for diabetes drug discovery.

1.7 Small Molecules in Clinical Development for Diabetes

Using methods described above, small molecules that modulate beta-cell function have been successfully identified. Luciferase based screening has enabled the evaluation of millions of compounds for their ability to modulate beta-cells. For instance, Harmine was initially discovered in HepG2 cells to promote proliferation through DYRK1A inhibition.[17] The aminopyrazine GNF-4877 similarly promotes beta-cell proliferation through the inhibition of DYRK1A and GSK3B.[12] Additionally, both Alsterpaullone and Ro 31-8220 were found to protect beta-cells against inflammation based apoptosis through GSK3B inhibition.[39] Several compounds were confirmed to reduce fatty-acid induced apoptosis in beta cells (lipotoxicity) through either a MAP4K4 kinase or calcium channel mediated pathway. [48] On the other hand, compounds including Milrinone, Forskolin, and Anagrelide were found to enhance GSIS through a luminescent reporter of insulin secretion.[53] These results were corroborated, with the addition of repaglinide, in a MALDI-TOF GSIS screen.[61,63] High content screening highlighted the

importance of HNF4-alpha in the modulation of insulin promoter expression.[78] Another HCS effort found Artemisinins cause alpha-cells to take on beta-cell characteristics.[79] Zebrafish screening studies revealed retinoic acids, glucocorticoids, and a number of other drugs classes that can increase beta cell mass.[80–82] The employment of cadaveric human islets in recently developed screening assays holds an exciting potential for the additional detection of beta-cell modulating compounds.[74,75]

Despite the discovery of numerous small molecule modulators of beta-cell function, many are barriers to clinical translation for diabetes indications. However, a number of existing therapeutics have undergone or are undergoing clinical trials to investigate their effectiveness in affecting beta-cell modulation to regenerate or preserve beta-cell mass. For instance, Lansoprazole (Prevacid) and Sitagliptin (Januvia) were studied in combination with Dyamid to protect and replenish beta-cell mass in new onset T1D.[84] Another therapy, Verapamil, demonstrated potential in inhibiting beta-cell expression of proapoptotic TXNIP and is currently being studied for its ability to prevent functional beta-cell loss in T1D.[85] Though Venetoclax exhibited promise in treating T1D in mouse models, it has yet to advance to clinical trials.[86] The LIBRA study in 2011-2014 was a Phase 3 trial to study the ability of Liraglutide, a GLP1 agonist, to preserve beta cell function.[87] The current Phase 4 trial hopes to discern if Liraglutide can protect beta-cell mass by diminishing ER stress in T2D patients.[88] On another front, Fingolimod (Fingoland) has displayed positive outcomes against T1D and is presently in a Phase 4 trial to evaluate its efficacy in countering T2D.[89] Although the repurposing of current therapies holds promise, the discovery of various small molecule modulators presents an exciting frontier in the pursuit to find new therapies for T2D.

Chapter 2
A Method for Automated High-Throughput, High-Content 3D Imaging of Intact Pancreatic Islets

2.1 Introduction

Diabetes mellitus represents a spectrum of persistent pathological conditions initiated by disruption in blood glucose homeostasis. Diabetes and sequelae affect 462 million people worldwide and approximately 12% of global health expenditure is dedicated to diabetes and associated sequelae.[89] The prevalence is predicted to increase as countries become more developed and it is estimated that 1 in 10 adults will be affected by diabetes by 2040, globally.[90] Blood glucose homeostasis is regulated by a network of metabolic pathways between the pancreas, liver, and skeletal muscle tissues.

Elevated blood glucose triggers a complex physiological response primarily centered around pancreatic beta-cells, skeletal muscle, and the liver. Specifically, when blood glucose levels rise postprandially, the beta-cells within the pancreatic islets of Langerhans respond by increasing the synthesis and release of insulin. Insulin, a key hormone in glucose homeostasis, binds to insulin receptors throughout the body, promoting glucose uptake by cells, mostly by large skeletal muscles, thereby reducing circulating glucose levels. Concurrently, insulin suppresses the activity of alpha cells in the pancreas, thereby inhibiting the secretion of

glucagon, a hormone that promotes glucose production. Furthermore, insulin acts on the liver to dampen gluconeogenesis, the process by which glucose is synthesized from non-carbohydrate precursors. This multifaceted response to hyperglycemia involving coordinated insulin-mediated glucose uptake, glucagon suppression, and the curtailment of hepatic gluconeogenesis, effectively counterbalances the elevated blood glucose levels, reinstating metabolic equilibrium.

Loss of beta-cell function and mass is the central event in the etiology of both Type 1 (T1D) and Type 2 diabetes (T2D), through distinct mechanisms.[61,91–94] Pancreatic islets are tight clusters of predominantly alpha and beta-cells that undergo functional and compositional changes when under chronic glucolipotoxicity.[19,36,95] Islet cells undergo hypertrophy and hyperplasia in diet-induced obesity to compensate for the increased demand for insulin during insulin resistance in T2D. The ability of beta-cells to compensate can vary widely among individuals, and compensatory mechanisms can ultimately fail, leading to beta-cell loss and the development of insulin dependence in type-2 diabetes mellitus (T2DM).[74,96,97] Furthermore, the exact mechanisms driving beta-cell hyperplasia and hypertrophy in T2DM are not yet fully understood, and improved experimental systems are needed to support basic islet biology and drug discovery efforts toward a curative pharmacologic therapy for T2D.

Current pharmacologic strategies and cell-based therapies for beta-cell replenishment include the stimulation of proliferation of existing beta-cells, differentiation or trans differentiation into new beta-cells from other cell types including ductal or stem cells, and differentiation of beta-cells from iPSCs and engraftment into extracellular matrix scaffolds for transplantation.[98] Mouse (MIN6) and rat (INS-1) insulinoma cell lines have been used to

interrogate beta-cell metabolic pathways and function.[98] However, cancer cell lines cultured in monolayers fail to capture islet complexity and are not capable of detecting pro-proliferative effects because they actively replicate. Existing strategies to assay primary islets in high throughput either rely on dissociating the cells for image cytometry or re-forming dissociated islet cells into pseudoislets.[11,57,96] The dissociation of islet cells results in the loss of important cell-to-cell communication, spatial connectivity and dissociation induces a prominent perturbation that may interfere with detection of bioassay endpoints.[74,97,98] Desirable characteristics for an improved islet screening platform would incorporate intact primary human or rodent islets, have single-cell resolution to detect infrequent proliferation events, and maximize the number of cell observations per condition/treatment for adequate statistical sampling.

Herein, we describe an improved 384-well method for automated high-content fluorescence imaging of multiple intact murine islets per-well with single-cell resolution and an analysis pipeline for image cytometric detection of nascent/proliferating beta-cells. Technological advancements in high-content imaging hardware allow for two-pass imaging involving low-magnification islet identification followed by high-resolution imaging of each individual islet. This two-pass imaging method coupled with serial 2D maximum intensity projection (MIP) imaging reduces the number of images needed per islet, reduces data size, speeds acquisition/analysis, and alleviates the need for true 3D image analysis that remains a technological barrier for most screening centers. By retaining the 3D structure, we are able to extract the cell populations and their spatial organization within each islet. Additionally, this

technology allows for the detection of in vivo beta-cell regeneration through isolation and quantitation of islets from drug treated animals to capture stimulated beta-cell proliferation.

2.2 Materials

2.2.1 Animals

8-12 week, male C57BL/6J mice were purchased from Jackson Labs. The mice were maintained on a normal chow diet and were housed on a 12-hour light/dark cycle. All animal protocols were approved by the University of Michigan Committee on the Use and Care of Animals in accordance with AAALAC and AVMA guidelines.

Table 1. Reagents required for this assay method.

Reagents	**Catalog Number**	**Provider**
RPMI 1640 + L-Glut	11875-093	Gibco
Hank's Buffer	14175-095	Gibco
Fetal Bovine Serum	FB12999102	Fisher Scientific
HEPES (1M)	15630-080	Gibco
PenStrep	15070-063	Gibco
NEAA	11140-050	Gibco
GrowDex-T	200103002	UPM BioMedicals
Bovine Serum Albumin	A2153	Sigma-Aldrich
Tween20	BP337-100	Fisher Scientific
TritonX100	21568-2500	Acros
PBS pH 7.4	10010-023	Gibco

Glycerol	17904	Thermo Scientific
Fructose	F0127	Sigma-Aldrich
Hoechst 33342 Trihydrochloride TriHydrate	H3570	Invitrogen
Ki67 Primary FITC Conjugated Antibody	115-698-82	Invitrogen
Nkx6.1 Rabbit Antibody	ab221549	Abcam
Glucagon Mouse Antibody	ab10988	Abcam
Goat anti-Rabbit IgG Secondary antibody Alexa Fluor Plus 555	A32794	Invitrogen
Goat anti-Mouse IgG Secondary Antibody Alexa Fluor 647	A21235	Invitrogen

2.2.2 Equipment

- Revvity 384-well PhenoPlate (6057300)
- Multichannel Pipette and tips
- Incubator (37^{o}C and 5% CO_2)
- Biosafety Cabinet
- 37^{o}C Water Bath
- Plate Rocker
- Aluminum Foil
- HPD300e Dispenser
- Yokogawa Cell Voyager 8000 Confocal Microscope (CV8000)
    - 4x Dry (NA=0.16) UPLXAPO4X
    - 40x Water Immersion (NA=1.0) UPLSAPO40XW

2.2.3 Software

- Yokogawa Search First
- CellPose 2.0[99]
- CellProfiler 3.8, 4.2 [42,98]
- Knime 4.5.1[100]

2.2.4 Reagent Setup

Table 2. Reagent Setup

Solution	**Components**
Islet Culture Media	86 mL RPMI 10 mL FBS 1 mL HEPES 1 mL L-Glut 1 mL NEAA 1 mL P/S
Collagenase Solution	1 mg Collagenase 1 mL Hanks
Hanks-FBS	180 mL Hanks Buffer 20 mL FBS
0.2% GrowdexT solution	1:5 dilution of GrowDex-T in cell culture media
Fix Solution	4% PFA in PBS
Perm Buffer	10 mL PBS 10 µL Tween 20
Wash Buffer	100 mg BSA 50 mL PBS 50 µL Triton X100
Primary Antibody Mix	Wash Buffer 1:500 dilution of Nkx6.1 Antibody 1:2000 dilution of Glucagon Antibody

Secondary Antibody Mix	Wash Buffer 1:1000 Alexa Fluor 647 1:1000 Alexa Fluor 555 1:500 Ki67 FITC 1:1000 Hoechst
Fructose Glycerol Solution[101]	3.3 mL Glycerol 0.7 mL dH_2O 2.97g Fructose

2.3 Islet Isolation Culturing

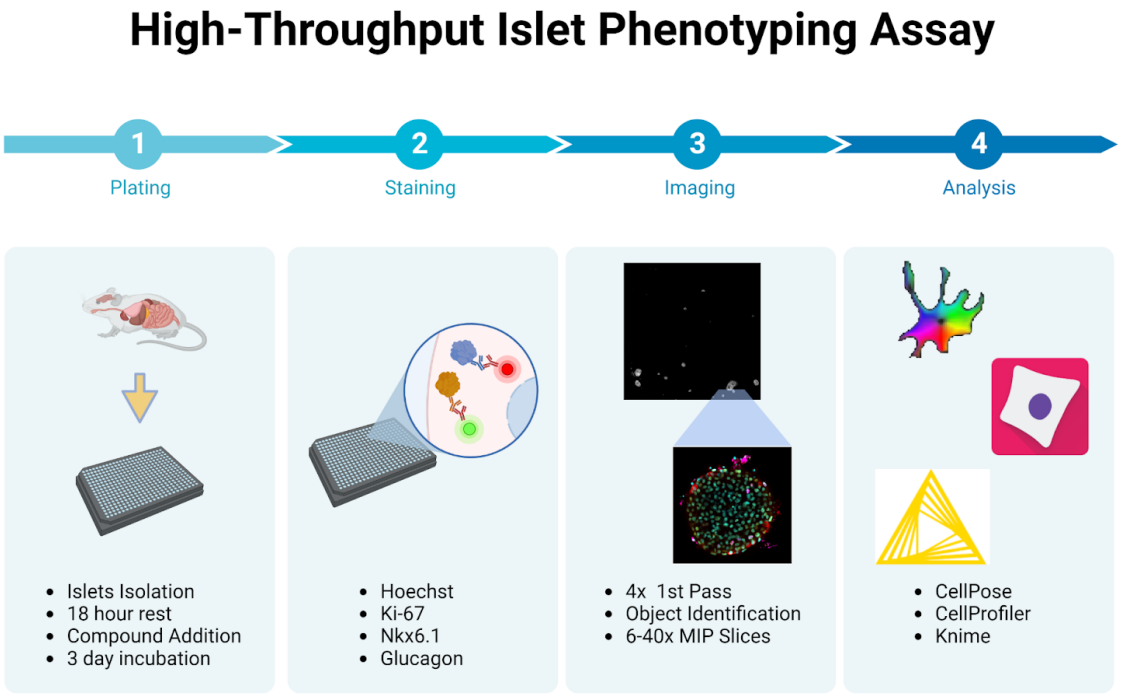

Figure 4. Workflow for high-content imaging of intact islets. (1) Islets are harvested from mice and placed in 384-well plates. (2) After fixation, islets are stained with Hoechst, Ki67, Nkx6.1, and Glucagon antibodies. (3) Imaging on a Yokogawa CV8000 with a 4X overview image of the entire well followed by centered 40X 3D-imaging of each islet. (4) Images are analyzed with Cellpose and Cellprofiler for islet and cell segmentation and feature extraction. Data analysis is performed using Knime.

2.3.1 Islet Isolation

Islets were obtained through the Michigan Diabetes Research Center (MDRC) Islet Isolation Laboratory. Isolation was carried out following established protocols.[102] In brief, mice were euthanized by CO2 asphyxiation. The pancreases were extracted and digested using a solution containing Collagenase P. A histopaque gradient is used to separate the endocrine islets from the exocrine cells. Islets are picked and counted into a 15 mL conical tube. Each cluster of endocrine cells is considered to be one islet equivalent (IE). Isolated islets were resuspended in Islet Culture Medium to a total concentration of 200 islet equivalents (IE) per mL.

2.3.2 Plating of Isolated Islets

1. Add 50 μL of the 200 IE/mL suspension per well of a 384 well plate
    a. If working with less than a full plate, islets are dispensed to the internal wells, omitting the edge wells.
2. Place the plate into the 37ºC 5% CO_2 incubator for 18-24 hours
    a. This allows the islets to recover after the extraction process and attach to the plate bottom.

a.

Table 3. General list of steps for plating and imaging of islets.

Step	Parameter	Value	Description	Equipment
1	Plating	5-20 islets/well	Adjust volume to desired islet concentration and add to wells	Biosafety Cabinet
2	Recovery	18-24 hrs	37°C, 5% CO_2	Incubator
3	ECM Addition	25 µL	Add GrowDex-T to each well	Biosafety Cabinet
3	Compound Plus DMSO Addition	100 nL per well	Use HPD300e or another method to add compounds to islet wells	Reagent Dispenser, Biosafety Cabinet
4	Incubation	72 hrs	37°C, 5% CO_2	Incubator
5	Fixation	1 hrs	Incubate at 4°C	Cold room
6	Permeabilization	15 min	Incubate at 4°C	Cold room
7	Block	15 min	Incubate at 4°C	Cold room
8	Primary Antibody	24 hrs	Incubate overnight at 4°C on a plate rocker	Plate Rocker
9	Secondary Antibody	24 hrs	Incubate overnight at 4°C on a plate rocker	Plate Rocker
10	Imaging	1-24hrs	Use a two-pass imaging protocol to image each islet	Yokogawa CV8000

2.3.3 Extracellular Matrix and Compound Addition

1. Islets are inspected with a brightfield microscope, and high-quality islets will have maintained their spherical shape. Exocrine cells attached to the outer surface of the islet will slough off.
2. Warm media to 37°C using a water bath

3. Sterilize the biosafety cabinet using UV light and wipe down all working surfaces with 70% (vol/vol) ethanol.
4. Aspirate media, leaving 5 µL in the well.
5. Add 25 µL 0.2% GrowDexT Solution.
6. Add 25 µL media on top of growdex.
    a. Media can contain compounds during this addition.
7. Use an HPD300e digital dispenser to dispense a 5 point, two-fold dilution series from 20 uM to 1.25 uM using a 5 mM Harmine stock solution in DMSO. DMSO content was normalized to 50 nL in each well.

Critical: Dry spotting the compounds before plating the islets may result in a high number of islets either having low attachment or dissociating.

8. Place in a 37ºC 5% CO_2 incubator for 72 hours to allow the treatment to take effect.

2.3.4 Fixation and Staining

The fixing and staining protocol was adapted from the Dekkers et al. protocol for 3D imaging of organoids.[42,99] The optimized fluorescent probe set consisted of Hoechst-33342 to label all nuclei, Ki67 to label proliferating cells, Nkx6.1 to identify nuclei of beta-cells, and glucagon to label alpha cells. We also found that EDU is interchangeable with Ki67. We observed that optical clearing with a high refractive index solution of fructose/glycerol prior to imaging significantly enhanced the signal-to-background and overall brightness of the fluorophores.

Prepare the Fix Solution, Perm Buffer, Wash Buffer, and Primary Antibody Solution according to the previous table.

1. Aspirate 45 µL of media from wells.
2. Add 45 µL of Fix Solution to each well.
3. Incubate plate at 4°C for 45 minutes.
4. PAUSE POINT: At this point, fixed islets can be stored at 4°C for up to a week.
5. Aspirate 45 µL of Fix solution.
6. Add 45 µL of Perm Buffer to each well.
7. Incubate for 15 minutes at 4°C.
8. Aspirate 45 µL of the Perm Buffer.
9. Add 45 µL of wash buffer to each well.
10. Incubated for 15 minutes at 4°C.
11. Aspirate 45 µL of wash buffer.
12. Add 45 µL of the primary antibody solution to each well.
13. The plate was rocked for 24 hours at 4°C.
14. Primary Antibody Solution was aspirated.
15. Wells washed three times with Wash Buffer.
16. To each well was added 50 µL of the secondary antibody solution and the plate was rocked on a plate rocker for 24 hours at 4°C.
17. The secondary antibody solution was removed, and the plate was washed 2x with Wash Buffer.
18. 2x wash with PBS and dispense 50µL of PBS per well.

PAUSE POINT: The plates were wrapped with foil and stored at 4°C until imaging.

19. Prior to imaging, aspirate PBS and add 50 µL fructose/glycerol optical clearing solution 15 minutes before imaging. This leads to a higher signal-to-noise ratio and allows for shorter exposure times. (Up to 4x S:N ratio)

2.4 Two-Pass Confocal High-Content Water-Immersion Islet Imaging

The technological advancement of high-content imaging platforms to include both water immersion objective lenses, dual microlens spinning disc confocal imaging, and coupled low-resolution/high-resolution imaging to enable 2D object identification and targeted high-resolution 3D imaging.

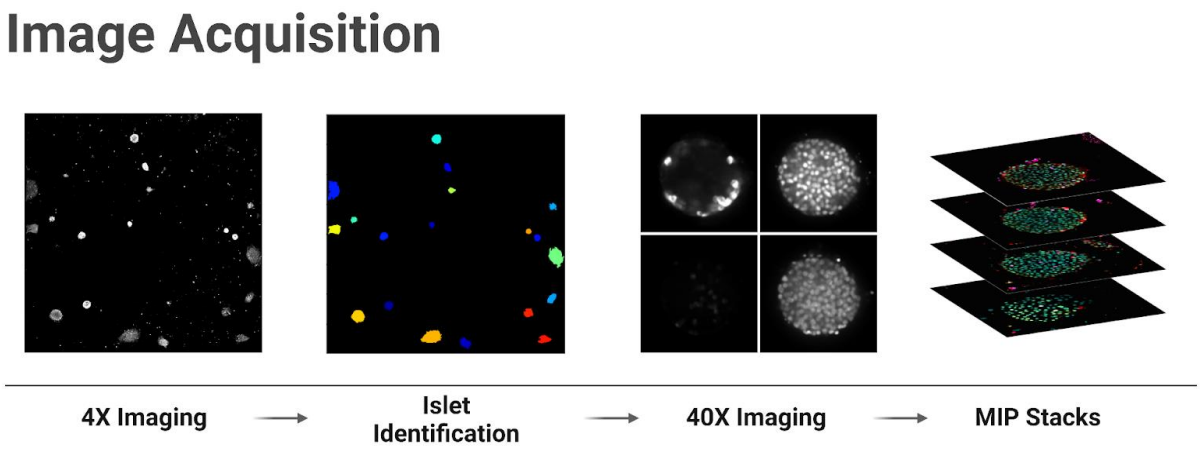

Figure 5. Image acquisition pipeline for the CV8000. A single 4x field captures the entire well for islet identification. 4X well images are then processed using CellProfiler to identify islets and filter out unwanted objects. The location of each identified islet is fed back to the microscope and imaged at 40x in second-pass 3D imaging.

2.4.1 4X Imaging

Using the 4X objective, a single field well-overview is captured for islet identification. The measurement setting was optimized for the Nkx6.1 channel which excludes any groups of non-endocrine cells and prevents photobleaching due to the long wavelength. For typical

protocols, the instrument autofocus (AF) utilizes the difference in refractive indexes of the plate bottom and the water in the well to locate the optimal focal plane. Optical clearing with high index of refraction fructose/glycerol can interfere with laser-based autofocus and requires detection of the plate bottom. The well-overview field was captured as a 3-slice maximum intensity projection (MIP) spanning 6 μm. Exposure time and laser power were adjusted to produce a minimum of 3:1 signal-to-noise ratio between the islets and empty areas of the well.

2.4.2 40X Serial MIP Stacks

Using the 40X water immersion objective allows for high-resolution 3D-imaging with one islet centered in the field of view. With this optical configuration, each islet occupies approximately 80-90% of the image. Each Z-section of the islet is a MIP acquired using an independent acquisition cycle which leads to a higher signal-to-noise ratio within the islet. Each MIP is composed of a five-image Z-stack spanning 2.5 um. Five MIPs are captured per islet with 7.5 um between each MIPs. The method for optimizing the distance between MIPs is described in the supplemental methods. Generally, peak intensities should be below 10,000 and signal-to-noise should be at a minimum of 3:1.

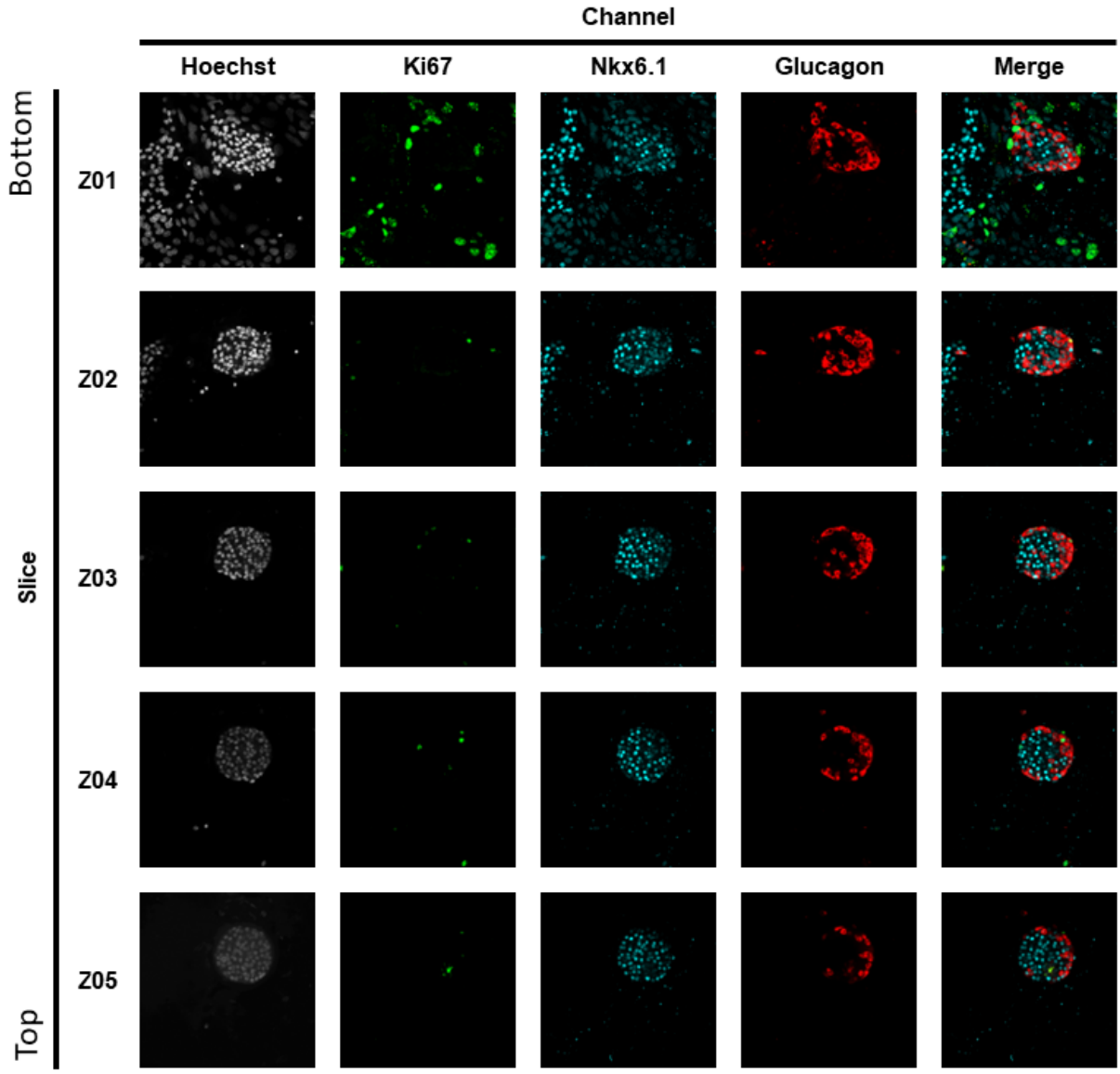

Figure 6. Example montage of an islet image stack. Rows correspond to MIP slices and columns are channels. Z01 represents the bottom of the islet and Z05 is the top. Hoechst staining is in grey, Ki67 antibody staining in green, Nkx6.1 in the middle cyan column, and glucagon is represented in red in the fourth column. Column 5 contains a merge of the Ki67, Nkx6.1, and glucagon channels.

2.4.3 CellProfiler Pipeline forIslet Identification

A CellProfiler pipeline is used to identify the islets in each 4X image. Images are loaded into the pipeline and objects 40-120 pixels in diameter are identified using Minimum Cross Entropy (MCE) thresholding. Object size and shape parameters are measured and objects with an eccentricity measurement above 0.9 are considered artifacts and are filtered out. The center coordinates for the retained objects are exported to a spreadsheet to be used by the Search First software.

2.4.4 Yokogawa Search First Acquisition

The 4X, Cellprofiler, and 40X measurement settings were all compiled separately and image acquisition was orchestrated by the Yokogawa Search First software. The Search First software captures the 4X image, analyzes each with the provided pipeline, then feeds object coordinates back into a 40X acquisition cycle, and finally applies post-processing image corrections before saving the files at the provided location.

2.4.5 Image Analysis

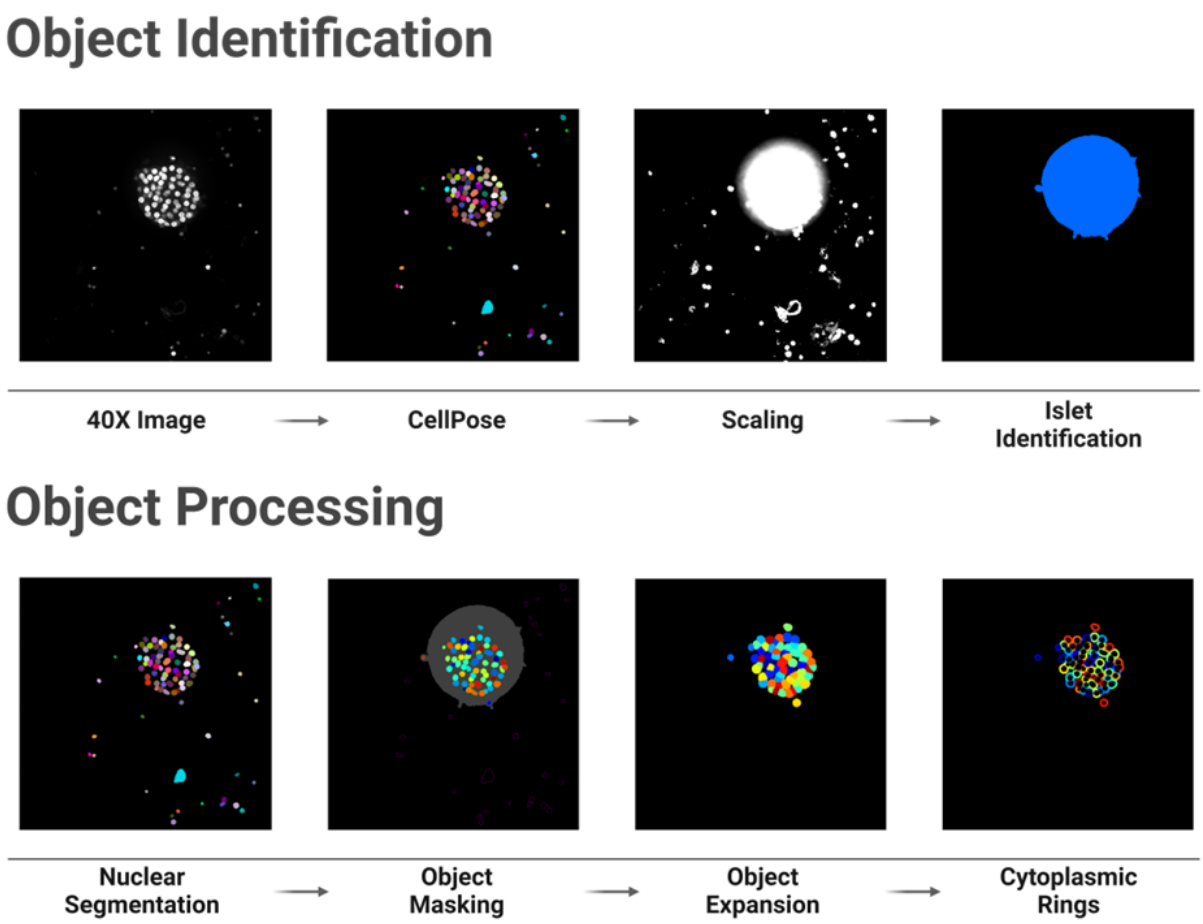

Figure 7. Top: Workflow for object identification in the 40X images. Cellpose segmentation software is used to identify all of the nuclei in the hoechst channel. In CellProfiler, fluorescence intensity is then scaled up and an islet object is identified. Bottom: Workflow for processing identified objects in CellProfiler. Masks from CellPose are imported into Cellprofiler. Nuclei that are outside of the islet rejected so measurements are only taken for islet cells. The remaining nuclei are expanded by 15 pixels to include cytoplasm surrounding the nuclei to create a 'cell' object. Finally, the nuclear objects are subtracted from the 'cell' objects to create a 'cytoplasmic' ring object.

A combination of CellProfiler and CellProfiler Analyst was used to identify out-of-focus images. For images that are in focus, nuclear objects are identified in every slice using Cellpose. These objects, along with the original images are then loaded into CellProfiler for intensity and morphometric feature extraction. This allows for the identification and rejection of exocrine cells, which have a higher replication rate and can skew replication measurements. Size,

intensity, texture, granularity, and radial distribution measurements are taken within the nuclear and cytoplasm for all channels. Relating each nucleus to the islet object allows for the quantification of cell organization patterns within the islets. The CellProfiler modules are described in the table below.

Table 4. Cellprofiler Modules for islet analysis.

Analysis Sequence	Description
RescaleIntensity	Rescales the intensity in the Hoechst channel for islet identification
IdentifyPrimaryObjects	Uses the hoechst channel to identify the whole islet
MaskObjects	Masks the cells outside the islet to omit them from analysis
IdentifySecondaryObjects	Expands nuclear mask, acquired from Cellpose, by 15 pixels to create a ‘cell’ object
IdentifyTertiaryObjects	Subtracts nuclear objects from secondary objects to make a cytoplasmic ring
MeasureObjectIntensity	Measures the intensity of glucagon, ki67, and nkx6.1 in the islet, nuclei, cell, and cytoplasm
MeasureObjectIntensityDistribution	Measures the intensity distribution of glucagon, ki67, and nkx6.1 in the nuclei, cell, and cytoplasm
MeasureObjectSizeShape	Measures the size and shape of the islets and nuclei
MeasureGranularity	Measures the granularity of glucagon, ki67, and nkx6.1 signal in the islet, nuclei, cell, and cytoplasm
MeasureTexture	Measures the texture of glucagon, ki67, and nkx6.1 signal in the islet, nuclei, cell, and cytoplasm
RelateObjects	This provides each cell’s distance from the centroid and outer edge of its parent islet
MeasureObjectIntensityDistribution	Measures the intensity distribution of glucagon and ki67 inside the islet
Export to Database	Exports all of the nuclear, cytoplasmic, and cell features to an SQLite database
Export to Database	Exports all of the islet features to an SQLite database

2.4.6 Data Analysis

After importing the SQLite database file into Knime, image metadata (PlateID, WellID and drug treatment information) was joined to the cell object table. The resulting table was composed of 1367 columns with intensity, size, shape, location, texture, and granularity measurements for 140,000+ cell object rows. Feature pruning identified 27 constant value columns that were removed using a constant value filer node. In the remaining columns, missing values were replaced with zeros for numerical values and NA for string values. A linear correlation filter was performed on a random sample set composed of 25% of the rows and removed any descriptors with a correlation greater than 0.90. The remaining 671 features were scaled using Z-score normalization.

To enable machine learning analysis, two feature subsets were created. The first contained NKX6.1 and Glucagon feature measurements while the second contained only Ki67 features. Principal Component Analysis dimensionality reduction was performed on both feature sets, condensing each set down to 5 principal components. Applying K-means clustering to the principal components produced 2 distinct clusters in each feature set. The cluster labels from both feature sets were joined back to the original cell data to label each cell as NKX+ or Glucagon+ and Ki67+/-. An example image set and processing pipelines are available on Zenodo (DOI: 10.5281/zenodo.7864552).

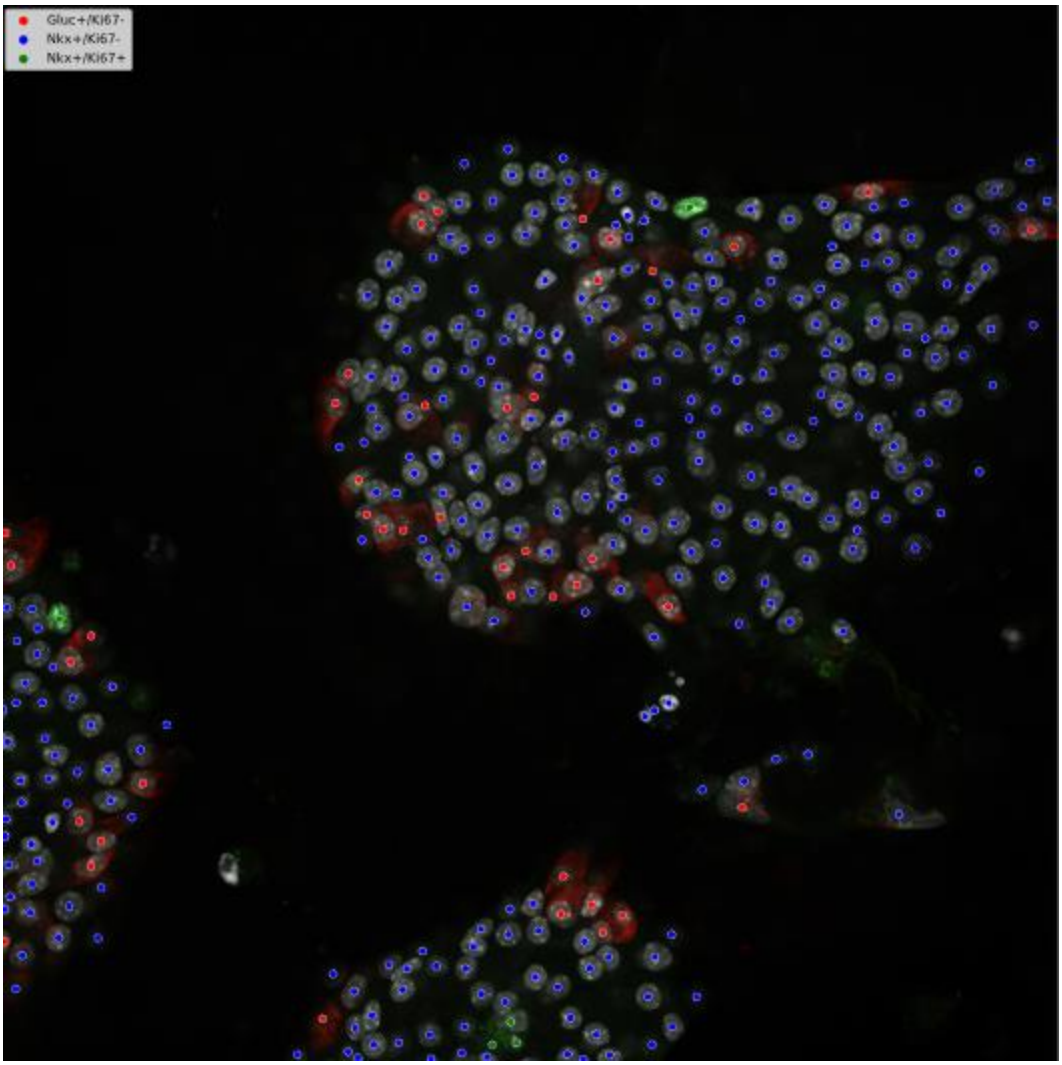

Figure 8. Unsupervised clustering labels are overlaid onto a composite image from an islet slice. Each identified cell has a plotted point at it's XY center. The color of the point represents the clustering label. Blue dots are Nkx6.1 positive, Ki67 negative cells. Red dots are Glucagon positive, Ki67 negative cells, and green dots are Nkx6.1 positive, Ki67 positive cells.

2.5 Results

2.5.1 Islet Culturing and Imaging Development

We developed an assay system that maintains the throughput of 2D dispersed islet assays while capturing the complexity of whole intact islets. Our primary aim was to include multiple islets in each well, allowing for efficient imaging and analysis, while also preserving the ability to extract spatial features. Our pipeline begins with the extraction of fresh pancreatic islets and plating roughly 10 per well in a 384-well plate. The islets are rested for 18-hours to allow for recovery and secure attachment. We found an overlay of GrowDex-T after this stage provided the islets with extracellular matrix support during compound treatment and protection during staining without any significant impact on image quality. Compound exposure lasts 3 days before fixation and staining. Islets were stained with Hoechst for nuclear segmentation, Ki67 to identify proliferating cells, Nkx6.1 as a nuclear beta-cell biomarker, and glucagon for alpha cell identification. Plates were imaged at 4X in the Nkx6.1 channel, islets were identified using CellProfiler, and the extracted coordinates were used to image each islet at 40x. We determined that, while true 3D segmentation was possible with this platform, serial 2D segmentation could expeditiously provide spatial features and is more amenable to high-throughput screening by reducing the complexity of the image analysis. The 40x images were processed with the Cellpose segmentation software and CellProfiler was used to extract features from identified objects.[102] Features were extracted on the islet and cell level. The identification of an islet object in each image allowed for the exclusion of exocrine cells in the analysis that remain after the islet extraction process.

2.5.2 Islet Phenotyping

The major shortcoming of dispersed islet assays is the loss of information related to the composition and organization within islets and the perturbation of islet cells by dispersion into a single cell suspension. After processing in Cellpose and Cellprofiler, cells were classified by either Nkx6.1 or Glucagon positive and Ki67 positive or negative. Of the combined 142,000 endocrine cells, 96% were beta-cells and 4% were alpha-cells. While this proportion of alpha cells was lower than expected, it has been shown that islet composition can vary dramatically even within the same species.[103] Through clustering of the Ki-67 features, we are able to identify the proliferating subpopulations within the alpha and beta-cell subsets. These features clearly separate the proliferating cell subpopulation into a distinct cluster when represented in a t-SNE plot (Figure 9A). By keeping the islets intact, we are able to see the cell type composition within each islet (Figure 9B).

Islets have been shown to have incredible variability in their architecture and our findings were consistent with this observation.[104] The amount of alpha cells and proliferating cells per islet varied dramatically, even within the same condition. This showed that certain islets are primed for beta-cell proliferation while others saw little to no proliferation. While alpha cell composition varied from 0 to >40%, we did not observe any correlation in the amount of proliferating beta-cells. It has been previously observed that differences in alpha cell composition can correlate with the original location of the islet within the pancreas. Glucagon-rich islets can be found in duodenal, gastric and splenic regions whereas glucagon poor islets are in the lower duodenal region of the pancreas.[105] Retention of the islet architecture allows us to quantitate how the various cell types are distributed within the islets. (Figure 9C) The beta-cells

show an even distribution throughout the islet. As has been previously observed for rodent islets, the alpha cells were scattered through the islet but more likely to be located at the islet edge.[106]

2.5.3 Induction of Beta-Cell Proliferation Using Harmine

To compare our assay system to typical islet dispersion assays, we chose to perform a standard beta-cell proliferation assay using Harmine. Harmine, a DYRK1A inhibitor, has been shown to consistently stimulate beta-cell proliferation.[17,107,108] We administered Harmine at five concentrations (20, 10, 5, 2.5, and 1.25 uM) and DMSO as a control. Due to the confounding ability of the DMSO vehicle to stimulate beta-cell proliferation, it was minimized to 0.4% and normalized across the dose range. This experiment consisted of 160 islets spread across 25 wells with each condition represented by 10-20 islets spread across 3 wells. After 72 hours of exposure to harmine, the islets were processed through the described pipeline. The highest doses of 20 uM, 10 uM, and 5 uM showed a significant increase in beta-cell proliferation over the vehicle control (Figure 9D). The extent of proliferation at 10 uM was slightly lower than what has been previously reported.[17] Analysis of the cell distributions showed that Ki67 positive cells were not evenly dispersed throughout the islet but instead mostly located on the outer edges of the islet, a distribution similar to that of the alpha cells. One potential explanation for slight decrease in proliferation and peripheral distribution of replicating cells could be poor drug penetration into these dense cell structures.

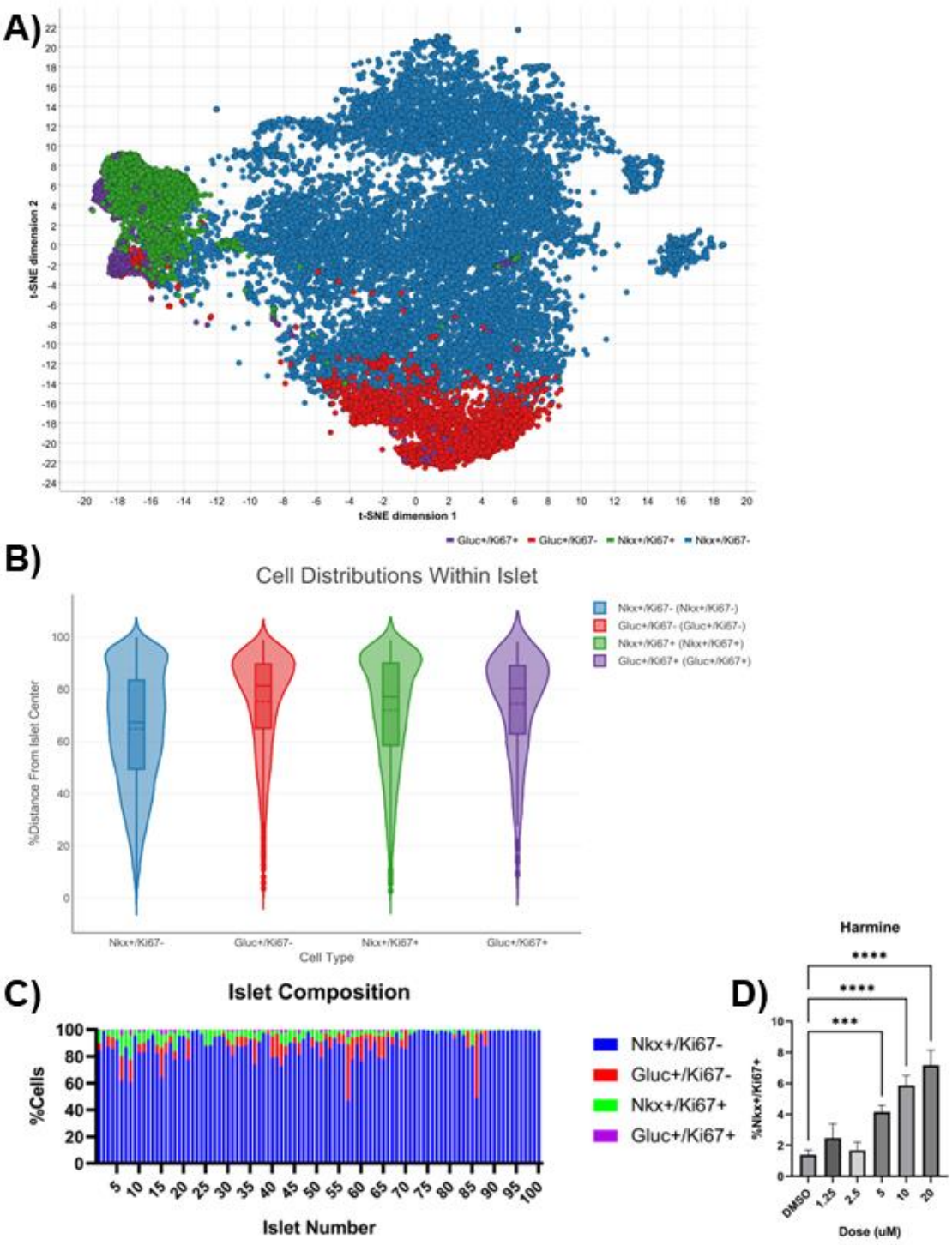

Figure 9. A panel of islet phenotype descriptors and results of Harmine stimulated beta-cell proliferation. (**A)** A t-sne plot of the islet cells showing discrete alpha/beta and proliferative populations with beta-cells shown in blue, alpha cells in red, proliferating beta-cells in green, and proliferating alpha cells in purple. (**B)** Violin plots with cell type on the X axis and the normalized distance from the center of the islet on Y axis. **(C)** A bar chart showing the cell composition in each islet. **(D)** A plot showing the amount of beta-cell proliferation observed in islets at various concentrations of Harmine. (***p< 0.001, ****p <0.0001 comparing conditions to DMSO control).

2.6 Advantages and Limitations

A key approach in diabetes research has been the Walpita et al. human islet method, which involves dispersing islet cells into a 2D layer to simplify imaging.[107] A crucial part of this method is the use of an extracellular matrix derived from HTB-9 cells, which aids in the adherence of dissociated islet cells that typically weakly attach to standard cell culture surfaces. The InSphero group has recently introduced a pseudoislet method that disperses islet cells and then reconstitutes a single human islet microtissue per well.[109] This method facilitates imaging by maintaining the reformed microtissue at the base of a round bottom well. Our approach, however, manages to circumvent many drawbacks of dispersed islet assays by preserving the islet structure. These intact islets attach firmly to standard cell culture plates. Maintaining the islet integrity permits the analysis of cell distribution in three dimensions, while eliminating potential inaccuracies due to false positives from exocrine cells or cell loss during staining. Our technique enables imaging of multiple islets per well, thus significantly enhancing throughput compared to single-islet-per-well or histological methods. By initially using a low magnification scan to locate each islet in the well, we can subsequently perform high-resolution imaging without needing to capture the empty spaces between islets. The primary constraint of this procedure is the availability of high-content imaging instruments with immersion objective lenses and two-pass imaging. The imaging process for a single plate, which may accommodate up to 4000 islets, requires approximately 12 hours to complete. An additional limitation in our method is the inability to accurately segment the cell cytoplasm, rendering measurements of beta-cell size or volume unachievable. Despite these limitations, this assay provides the diabetes research community with a high throughput technique that more closely resembles physiological

conditions than other available methods, potentially leading to more efficient drug screening. Although this study is focused on pancreatic islet phenotyping, it is broadly applicable to other 3D organoid or spheroid cell culture systems.

2.7 Conclusions

With the escalating global diabetes epidemic, novel curative pharmacotherapies that restore beta-cell mass in diabetes are urgently needed. The diabetes drug discovery field has been significantly hindered by the lack of robust preclinical phenotypic islet bioassays. Established bioassays using cancer insulinoma beta-cell lines are inadequate for studying beta-cell proliferative effects. To rectify this, we have developed an ex vivo pancreatic islet bioassay that can detect beta-cell proliferation, chemoprotection, and islet spatial morphometrics. High-content imaging instruments with water immersion and two-pass and 3D imaging are an enabling technology that delivers a robust islet phenotyping platform capable of scaling for high-throughput screening. The advancements in imaging technology described herein, coupled with machine learning analysis yield a robust image cytometric method for detecting drug-induced beta-cell proliferation. We demonstrate the utility of this method by detecting selective beta-cell proliferation induced by harmine, a natural product and DYRK1A inhibitor. The technology also enables the detection of in vivo beta-cell regeneration. This assay offers a high throughput bioassay with higher physiological relevance than other methods, potentially improving diabetes drug discovery and development.

2.8 Supplemental Materials

2.8.1 Z-Slice Optimization

Several islets were imaged using 0.1-micron Z spacing resulting in 300 slices (Figure 10A). The nuclei were identified individually in each slice, then grouped into nuclear objects by similar xy nuclear center coordinates across consecutive z slices (Figure 10). From this, we were able to determine 10 microns as the 75% interquartile range for the distance each nucleus spans (Figure 10C). This distance was then used as a starting point for the distance between each MIP to get roughly one nuclear slice per cell in every cell within each islet during imaging. This spacing, paired with 2.5-micron max intensity projections (MIPs), vastly reduced the number of images per islet from >300 to 7 while retaining important spatial data.

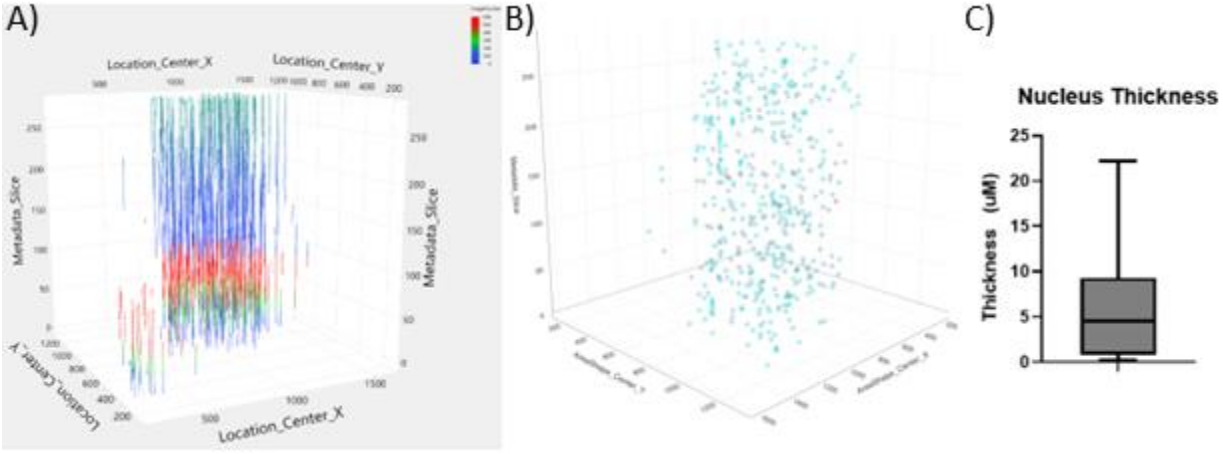

Figure 10. Z-Stack cell analysis. A) Scatterplot the XY coordinates for every nucleus in all 300 slices along the Z axis. B) Scatterplot of the XYZ center of each cell. C) Box plot of thickness of each cell in the islets.

Chapter 3 Creating Exploration of a Chromenone Scaffold as an Anti-Diabetic Therapeutic

3.1 Introduction

Diabetes affects more than 420 million people and, as of 2019, is the ninth leading cause of death globally. This long-term medical condition presents a myriad of potential complications ranging from blindness to limb amputation. Furthermore, it also includes kidney failure, and a threefold increased risk for heart attacks and strokes.[110] The damaging effects of moth major forms of diabetes, Type-1 and Type-2, stem from the dysfunction of beta-cells in the pancreas. For Type-1 diabetes, cell loss occurs through a chronic autoimmune response that attacks the beta-cell population. In Type 2 diabetes (T2D), existing beta-cell populations cannot meet the increased demand for insulin resulting from progressively worsening insulin resistance. The persistent challenge on the beta-cells leads, over time, to a significant reduction in beta-cell mass, up to 25-65%.[111]

Glycemic control and managing comorbidities, both short and long term, are the greatest challenges facing individuals with diabetes. Treatment generally starts with several classes of antidiabetic reagents before transitioning to insulin administration. Metformin, the most prescribed antidiabetic, suppresses hepatic glucose production; however, its ability to further help an individual is limited without weight loss.[112] The addition of a sulfonylurea can increase

insulin production in the short term but might be at the expense of increased β-cell loss.[113] Thiazolidinediones, PPAR-gamma agonists, are a potent class of therapeutics that have pronounced effects throughout the body. Not only do thiazolidinediones promote insulin production by β-cells, but they provide a protective effect for the β-cells against lipotoxicity from free fatty acids. This protective effect is achieved through an increase in the number of adipocytes, which better contain and seal away the fatty acids. Unfortunately, an increased number of adipocytes can result in patient weight gain.[114] Other successful therapies for T2DM include GLP1 modulators, glucose absorption blockers, and insulin administration.

Numerous research groups are working to develop therapeutics aimed at expanding a patient's beta-cell population.[115] This has been a prominent focus of diabetes research since the discovery of 5-IT by Annes et al., a compound that selectively promotes beta-cell proliferation in murine islets.[114] In the ensuing years, investigators used a high throughput screen chemical screen to identify harmine, a compound that mimics 5-IT's effect in human beta cells. An investigation into the mechanism of action (MOA) showed harmine inhibits several enzymes, including dual-specificity tyrosine-regulated kinases (DYRK1A, DYRK1B, DYRK2, DYRK3), monoamine oxidases (MOAs), and cdc-like kinases (CLKs). Importantly, test on INDY, a known inhibitor of DYRK1A previously developed for Down syndrome treatment, demonstrated that it too could cause beta-cell proliferation. This evidence led researchers to attributed harmine's proliferative activity to it's DRYK1A inhibition.[17,116] Shortly following this discovery, further exploration confirmed 5-IT's potent proliferative effect on human beta cells, also pinpointing the inhibition of DYRK1A as the underlying mechanism, echoing the MOA of harmine.[107]

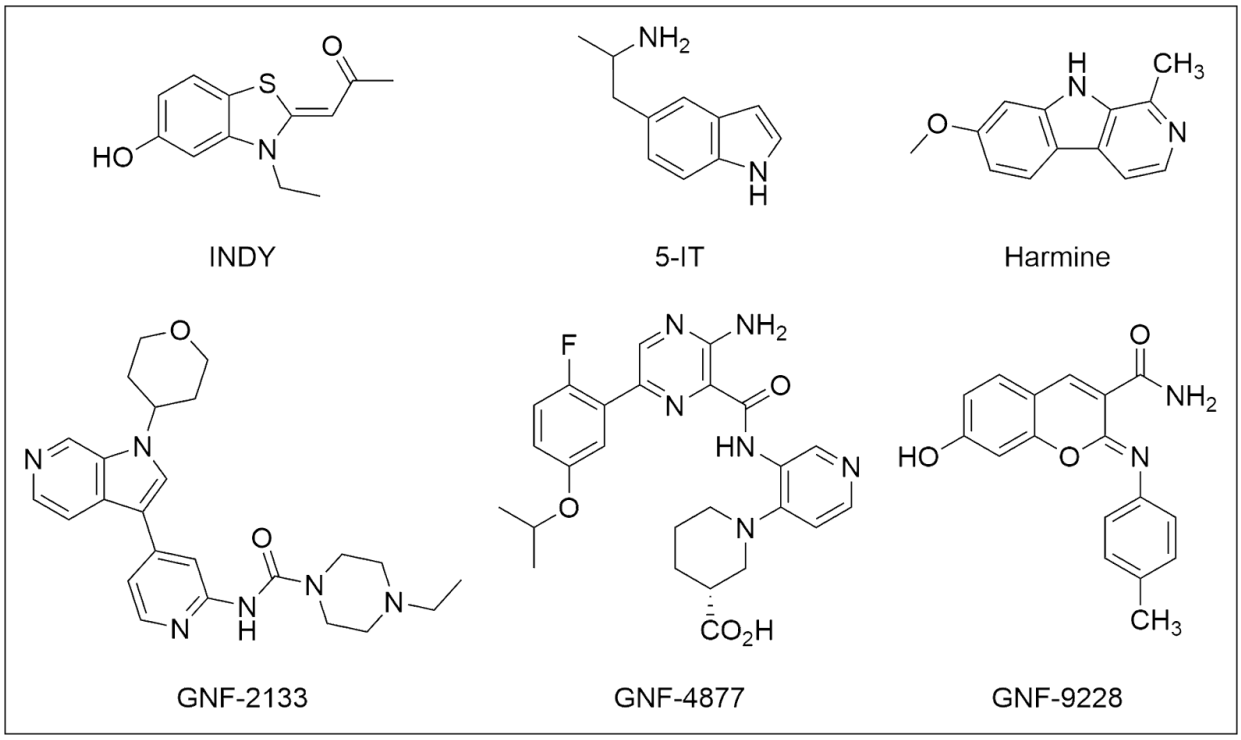

Figure 11. Structures of beta-cell proliferative compounds reported in the literature.

One promising strategy for treating diabetes would be to use a therapeutic to expand a patient's native beta-cell populaiton.[117] This has been a prominent focus of diabetes research since the discovery of 5-IT by Annes et al., a compound that selectively promotes beta-cell proliferation in murine islets.[117] In the ensuing years, investigators used a high throughput chemical screen to identify harmine, a compound that mimics 5-IT's effect in human beta cells. An investigation into the mechanism of action (MOA) showed harmine inhibits several enzymes, including dual-specificity tyrosine-regulated kinases (DYRK1A, DYRK1B, DYRK2, DYRK3), monoamine oxidases (MOAs), and cdc-like kinases (CLKs). Importantly, experiments with INDY, a known inhibitor of DYRK1A previously developed for Down syndrome treatment, demonstrated that it too could cause beta-cell proliferation. This evidence led researchers to attributed harmine's proliferative activity to its DRYK1A inhibition.[17,116] Shortly following this

discovery, further exploration confirmed 5-IT's potent proliferative effect on human beta cells, also pinpointing the inhibition of DYRK1A as the underlying mechanism, echoing the MOA of harmine.[107]

In early 2013, a series of diaryl urea compounds were reported to promote beta-cell proliferation through the NFkB pathway.[11] Two years later, progress was made with the development of the diaryl urea compounds into a series of aminopyrazine compounds, GNF-4877 being one, that not only promote beta cell proliferation but are also more potent than harmine.[12] The mechanism of action was identified to be regulation of the NFAT translocation pathway through inhibition of both DYRK1A and GSK3B. Finally, in 2020, a structure-activity-relationship (SAR) campaign led to the evolution of GNF-4877 into GNF-2133. This new series of 6-azaindole compounds boasted enhanced potency in human beta-cells and favorable pharmacokinetics. However, hypertrophy was observed in several tissue types other than pancreatic when GNF-2133 was tested in vivo.[123]

At the same time, a high throughput screen was carried out using an INS-1-derived cell line, augmented with a VGF luciferase reporter, and the GNF chemical library. This screen identified two major scaffolds, among which GNF-9228 stood out as a more potent proliferator. When compared to GNF-4877, GNF-9228 does not spur proliferation through inhibition of the NFAT translocation pathway. Additionally, when GNF-9228 is co-administered with harmine, the proliferative effect intensifies, suggesting its MOA may diverge from the conventional DYRK1A pathway. Unfortunately, a challenge was noted in that GNF-9228 was susceptible to remarkably rapid clearance.[22] Given the promising potency, selectivity, and unusual MOA of

GNF-9228, our lab elected to initiate a SAR campaign focused on improving the pharmacokinetics of GNF-9228, particularly addressing the problems with clearance.

3.2 In Vivo Efficacy

GNF-9228 induces a considerable enhancement in beta cell proliferation in vitro, with reported increases of up to tenfold. Additionally, it has demonstrated a remarkable capacity to shield beta cells from cytotoxic stress and augment glucose-stimulated insulin secretion (GSIS), elevating insulin secretion by up to threefold.[22] Previous studies examined the in vivo pharmacokinetics, but did not explore its efficacy. Emboldened by these promising findings, we administered GNF-9228 within a diet-induced obesity (DIO) mouse model. The formulation of GNF-9228 was devised to minimize dimethyl sulfoxide (DMSO) content, a strategic approach aimed at precluding any potential assay interference.[123,126]

To evaluate the impact of GNF-9228, we have also incorporated whole islet imaging as an analytical tool in our study. Pancreatic islets were harvested from treated mice and subjected to high-throughput, high-content imaging methodologies designed to preserve their structural integrity.[124] Unlike histological sectioning, which only provides limited, two-dimensional, monolayer depictions of tissue structures, whole islet imaging provides a more holistic and accurate insight into the drug's effects on the islets.[124] This assay protocol facilitated enhanced visualization and quantification of beta cell proliferation, surpassing the capabilities of conventional histological sections (Figure 12A). Analysis quantified up to a 5.5% EDU incorporation among the treated animal cohort (Figure 12B). In vivo, GSIS assessments were conducted before and after compound administration as a complementary investigative approach. Albeit a discernible variance between the pre- and post-treatment conditions was observed, the

introduction of GNF-9228 did not yield an improved insulin release response to a glucose bolus (Figure 12C).

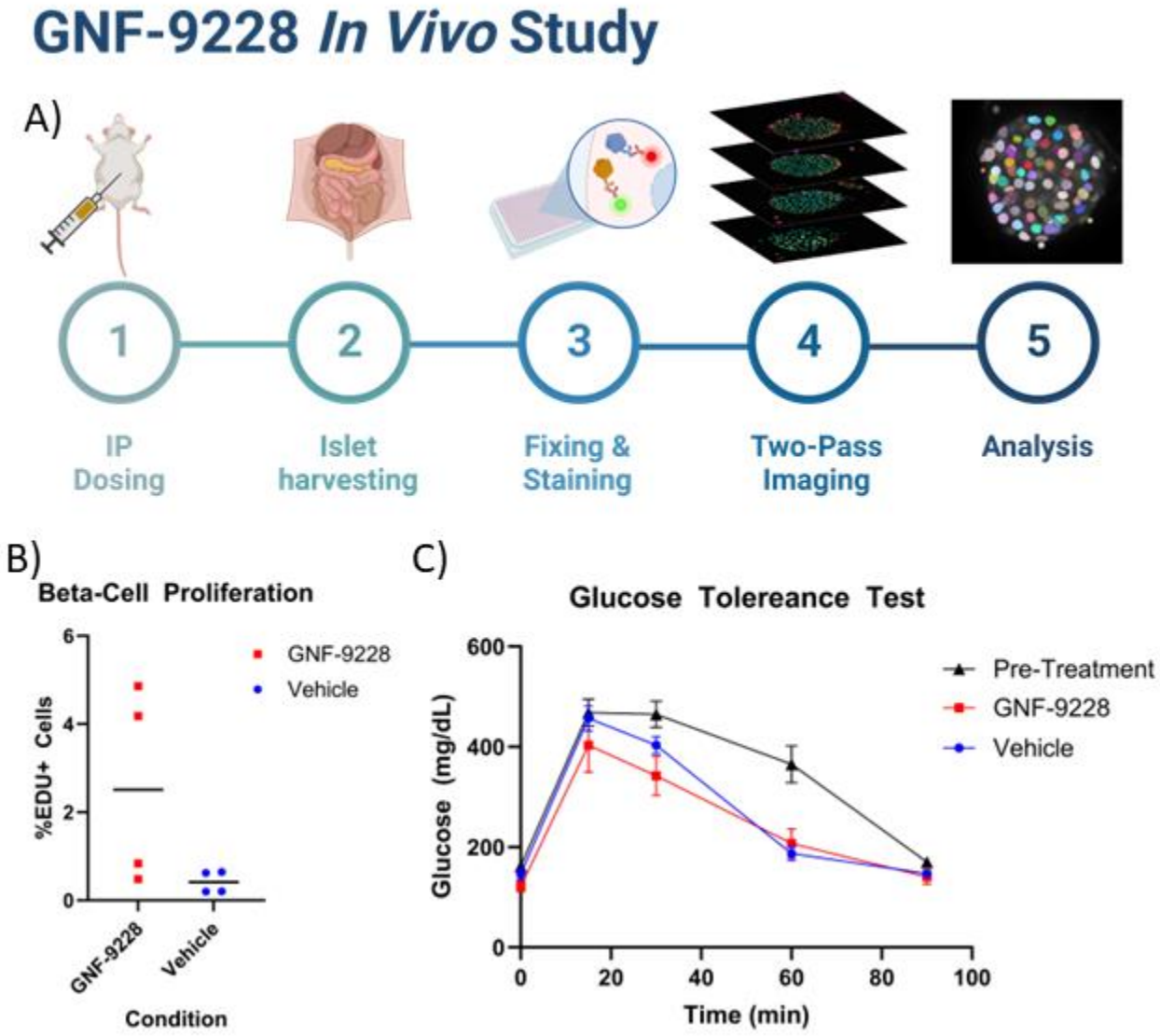

Figure 12. GNF-9228 In Vivo Study results. A) Workflow for in vivo dosing and high-content islet analysis. B) Graph showing %EDU positive cells per animal in either the treated or control group. C) Glucose Tolerance Test results shown as blood glucose levels over time.

Comparative assessment between our in vivo data and published data derived from isolated islets underscored the partial efficacy of the treatment, potentially attributed to inter-

individual pharmacokinetic variations. Notably, discernible compound deposits were identified within the abdominal region of certain animals. The deposits could have enabled the compound's more sustained and steady-state presence than would have otherwise been achieved. These outcomes collectively illuminate the promising potential of GNF-9228 as an in vivo probe, contingent upon the refinement of its physicochemical attributes to optimize systemic exposure.

3.3 Metabolite ID & Microsomal Stability Studies

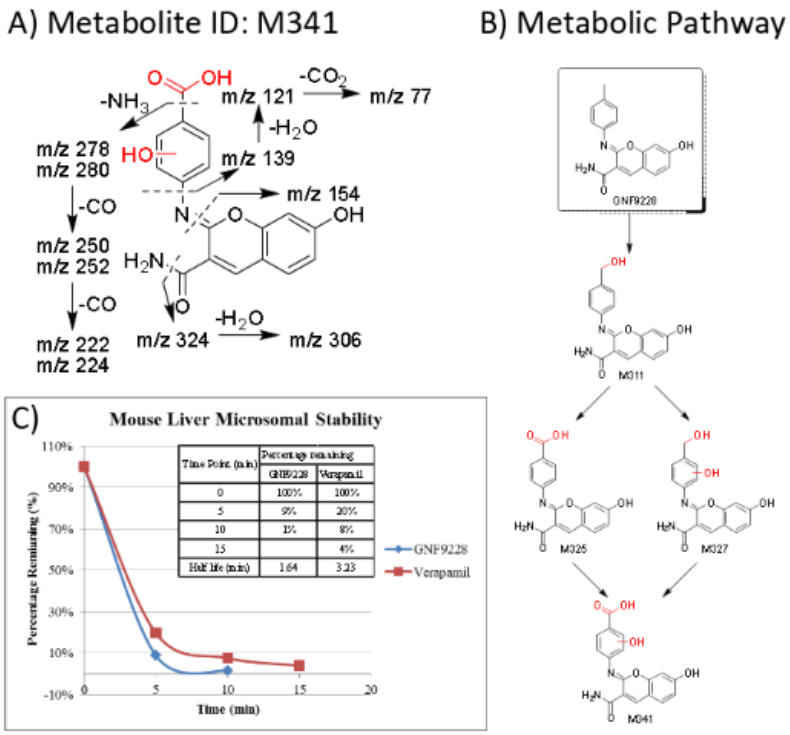

Figure 13. Metabolic analysis of GNF-9228. A) Metabolite ID study results. B) Proposed oxidation sites and metabolic pathway of GNF-9228. C) Mouse liver microsomal stability of GNF-9228.

Given the results of the in-vivo experiment, we hypothesized unfavorable pharmacokinetic characteristics and low potency likely impede the application of GNF-9228. In light of this setback, our research strategy commenced with an investigation into the metabolic

profile of the molecular scaffold. The results of a microsomal stability study showed a highly rapid breakdown of GNF-9228. Due to this, a metabolite ID study was conducted to elucidate clearance pathways. The outcomes of this investigation revealed that the aniline moiety, bearing the R2 substituent, served as the principal site of oxidation within the scaffold. Specifically, the 4-methyl group was found to undergo oxidation, forming a primary alcohol moiety. Subsequent observations unveiled the occurrence of further oxidations, leading to the formation of either a carboxylic acid or a phenol. Based on these insightful findings, the aniline moiety emerged as the primary target for subsequent synthetic endeavors in our synthetic campaign.

3.4 Synthesis

We found the chromenone scaffold to be well suited for a structure-activity-relationship (SAR) campaign. To access salicylaldehydes **2** that were not commercially available, a Vilsmeier-Haack reaction could be used. This reaction uses phosphorus oxychloride and DMF to generate an electrophilic chloroiminium ion whose reaction is directed by the R and hydroxyl group of **1**.[127] Substituted cyanoacetemides were made through the condensation of the ethoxyacetamide with a primary or secondary aniline.[128] Subsequently, the core moiety (**5**) was synthesized via a one-pot Knoevenagel Condensation between the salicylaldehyde (**2**) and cyanoacetamide (**4**), followed by an intramolecular ring closing.[129] From here, the addition of anilines and other aromatic amines is facile through nucleophilic attack of the pyran in acetic acid.[130] This synthetic route demonstrated notable efficiency, delivering acceptable yields while minimizing the need for extensive purification processes.

The metabolite ID study's findings emphasized the aniline moiety's pivotal role as our scaffold's primary site of metabolism. Significantly, incorporating the aniline as the final step in the synthetic sequence enabled the generation of diverse compounds through high-throughput late-stage functionalization. To expedite this process, seventy-eight reactions were concurrently conducted using HPLC vials. Each vial was outfitted with six glass beads and tared before setting up the reactions. A concentrated stock solution of aniline in methanol was added to a dilute stock of the core **5a** in acetic acid. The vials were placed on an Orbitrap shaker overnight. After shaking, the vials were centrifuged to accumulate the finished product at the bottom of the vials. The reaction mixture was decanted off, and a similar process was employed for ether and water washes. The final remnants of water were removed from the samples using a lyophilizer. The vials were reweighed, and the final product was taken up in DMSO to generate 100 mM stock solutions. Reaction products were confirmed via UPLC/MS analysis, and it was

determined that forty-six were successful.

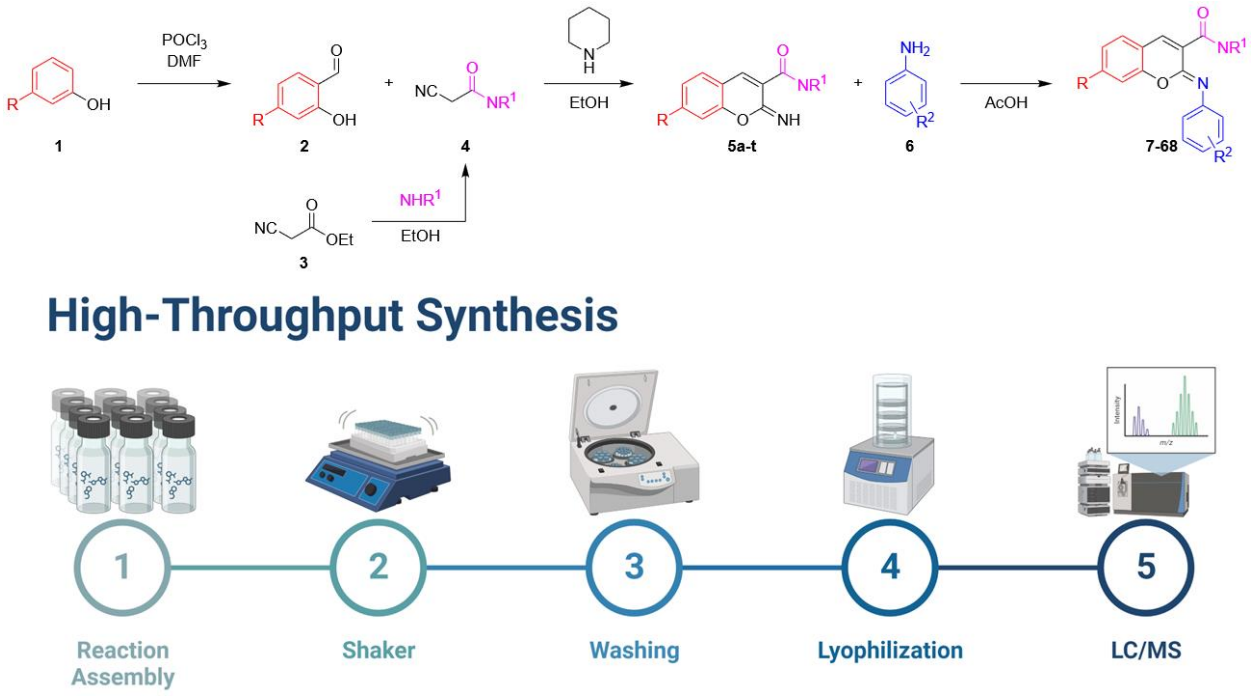

Figure 14. Synthesis of GNF-9228 analogs. Top: Synthetic route for the synthesis of GNF-9228 scaffold. Bottom: Workflow for the high-throughput synthesis of chromenones.

In addition to the aniline site implicated in the mouse liver microsome study, a range of substitutions were implemented at two other positions on the core. Several attempts were undertaken to introduce various groups at the R1 position. Initial endeavors to synthesize the morpholine amide core yielded fruitful outcomes; however, introducing additional steric bulk at R1 impeded the aniline addition reaction. Consequently, a cyclohexyl amide derivative was synthesized to mitigate some steric hindrance surrounding the reactive amine. Regrettably, the final reaction did not progress as anticipated, but the synthesized compounds were carried forward into the bioassays. In total, seventy-five analogs were generated and subsequently subjected to bioassays for further evaluation. (Table S1)

3.5 Biological Evaluation

3.5.1 VGF Expression and Cytotoxicity Protection

The initial screening of GNF-9228 was conducted utilizing an INS-1 rat insulinoma cell line transfected with a plasmid capable of expressing luciferase under the control of a VGF promoter.[22] The induction of VGF expression is known to occur through the action of Nkx6.1 in pancreatic islets, producing peptides that confer protection to islet beta cells against apoptotic cell death. Moreover, increased expression of Nkx6.1 has been associated with a selective promotion of beta-cell proliferation.[20] All synthesized analogs were tested at 10 uM the luciferase based assay to access upregulation of VGF, and subsequently upregulation of Nkx6.1 (Table 9).

Among the initial set of aniline analogs generated in the high throughput synthesis, a subset displayed at least 30 % efficacy relative to GNF-9228 at 10 uM in the INS-1 luciferase assay (Table 1). The nitrile and fluorinated analogs were particularly interesting, as their electron-withdrawing properties were expected to impede benzene ring oxidation and mitigate the methyl carbon as a susceptible site of oxidation. When an attempt was made to merge **7** and **17** into a single analog, a complete loss of activity was observed. This outcome prompted a hypothesis that attributed the loss in activity to the alterations in ring electronics stemming from the steric similarities between the proton and its fluorine substituent. For this reason, the electron-rich ring of **14** was promising despite its predicted poor metabolic stability. A trifluoromethoxy analog (**15**) was synthesized to circumvent this apparent weakness and proved similarly efficacious in the luciferase assay, showing that an electron-rich ring was desirable at

R2. Compound **5b** was of particular interest due to its noticeable efficacy and comparably different metabolic profile than GNF-9228.

Table 5. Top GNF-9228 analogs with their normalized response in the luciferase assay (%Luc) and cytotoxicity assay (%Viability), along with calculated physical properties.

Cmpd	R	R1	R2	%Luc	%Via	MW	cLogP	HBA	HBD	Rot
9228	3-OH	H	4-CH3	100.58	104.42	294.31	2.94	3	2	2
7	3-OH	H	2-F	52.19	49.24	298.27	2.56	3	2	2
8	3-OH	H	3-F	18.06	9.31	298.27	2.56	3	2	2
9	3-OH	H	2,4-F	28.98	123.55	316.26	2.71	3	2	2
10	3-OH	H	2,6-F	14.49	100.87	316.26	2.71	3	2	2
11	3-OH	H	2,5-F	39.87	45.87	316.26	2.71	3	2	2
12	3-OH	H	2,6-F, 4-OMe	25.52	79.05	346.29	2.55	4	2	3
13	3-OH	H	2-F, 4-CN	8.86	98.54	323.28	2.42	4	2	2
14	3-OH	H	4-OEt	58.06	111.26	324.34	2.62	4	2	4
15	3-OH	H	4-OCF3	60.05	-15.24	364.28	3.85	4	2	4
16	3-OH	H	4-tbutyl	46.42	135.60	336.39	3.97	3	2	3
5b	3-OH	Cyclohexyl	---	39.88	95.39	286.33	2.30	3	3	2
17	3-OH	H	4-CN	51.25	-1.51	305.29	2.28	4	2	2
18	3-OH	H	3-CN	6.22	3.47	305.29	2.28	4	2	2
19	3-OCH3	H	4-CN	25.87	115.85	319.32	2.42	4	1	3

The expression of the pheromone VGF ultimately leads to the production of TLQP-21, a peptide recognized for its ability to safeguard beta cells and facilitate the trafficking of insulin vesicles.[21] Therefore, we employed an orthogonal assay, an endoplasmic reticulum (ER)-induced cytotoxicity assay. This confirmed the activity of some compounds while showing others were ineffective. Esters in the 4-position generally saw moderate to superb activity in this assay

system. While compound **14** underperformed in the luciferase assay relative to GNF-9228, it provided better protection against Thapsigargin than GNF-9228. However, we were surprised that **15** was no better at protecting the cells from ER-mediated cytotoxicity than the DMSO control. Additionally, the cyclohexyl amide **5b** showed similar efficacy to the lead compound. Most modifications to R were not well tolerated; however, the methoxy analog **19** performed much better in the cytotoxicity assay than its parent **17**.

3.5.2 Structure-Activity Relationships

The core phenol (R), the amide (R1), and the aniline (R2) were three positions on this molecule that were accessible for facile derivatization. Results in the luciferase and cytotoxicity assays were poorly correlated for aniline analogs, showing an R-squared of only 0.3. Changes in basic molecular properties such as cLogP, molecular weight, hydrogen bond acceptors (HBA), or hydrogen bond donor count (HBD) had no overarching activity trends. When comparing similar substitutions at the 3 and 4 positions of the aniline moiety, the substitution at the latter position generally outperformed the former. This can be seen in the fluoro and nitrile analogs. Likewise, a discernible trend emerged wherein bulky substitutions at the 3-position of the aniline moiety resulted in diminished potency or even loss of activity in the luciferase assay; however, the cytotoxicity assay was much more tolerant of these groups. Bulky lipophilic groups at the 4-position tended to fare well in both assays. Compounds **16** and **14** are examples of this trend.

Table 6. Results in the cell-based assays for modifications to the chromenone core.

Cmpd	R	R1	R2	%Luc	%Via	MW	cLogP	HBA	HBD	Rot
19	3-OCH3	H	4-CN	25.87	115.85	319.32	2.42	4	1	3
20	3-H	H	4-CN	3.85	-10.78	289.29	2.58	3	1	2
21	3-Me	H	4-CN	29.41	-22.12	303.32	3.09	3	1	2
22	3-t-butyl	H	4-CN	15.86	-22.19	345.40	4.13	3	1	3
23	2-OH	H	4-CN	8.38	-29.16	305.29	2.93	4	2	2
24	4-OH	H	4-CN	4.84	-29.16	305.29	2.28	4	2	2
25	3-F	H	4-CN	15.72	-20.87	307.28	2.72	3	1	2
26	3-Cl	H	4-CN	11.45	-10.18	323.74	3.19	3	1	2
27	3-Br	H	4-CN	26.65	-3.25	368.19	3.35	3	1	2

Modifications to the phenol core consistently yielded diminished efficacy, as observed across various analogs in the series. Compound **20** eliminated the hydroxyl group (R) from the core, which led to a complete activity loss in both assay systems and suggesting its essential role. Furthermore, the substitution of the hydroxyl group with lipophilic moieties failed to elicit any therapeutic effects (**21-22**), underscoring the necessity of a hydrogen bond acceptor or donor group at R. Notably, a hydroxyl walk around the benzene ring revealed that the 3-position exhibited the highest efficacy, while moving the hydroxy to the 2 or 4 position demonstrated a complete loss of activity. Likewise, replacing the hydroxyl group with a halogen atom resulted in nearly complete inactivity (**25-27**). Conversely, **19** exhibited a notable reduction in efficacy in the luciferase yet excelled in the cytotoxicity assay, implying the need for an H-bond donor at R.

Table 7. Amide analogs of the GNF-9228 scaffold.

Cmpd	R	R1	R2	%Luc	%Via	MW	cLogP	HBA	HBD	Rot
5c	3-OH	Cyclopropyl	---	7.60	96.28	244.25	0.96	3	3	2
5d	3-OH	Cyclobutyl	---	30.20	79.69	258.28	1.41	3	3	2
5e	3-OH	Cyclopentyl	---	30.24	83.99	272.30	1.85	3	3	2
5b	3-OH	Cyclohexyl	---	39.88	95.39	286.33	2.30	3	3	2
5f	3-OH	Cycloheptyl	---	21.71	18.86	300.36	2.74	3	3	2

3.6 *In vivo* Pharmacokinetics

A PK study was performed to deduce if changes to the aniline moiety would improve in vivo metabolic stability, as the metabolite ID study suggested. With primary metabolism predicted to occur on the aniline methyl, we surmised that compounds containing electron-withdrawing groups would protect the ring from oxidation while removing the methyl site. Much to our dismay, modifications to the aniline ring were largely ineffective. Deuteration of the methyl group (**58**) showed no increase in stability. Compounds with a nitrile in the 4-position, **13** and **17**, showed a slight increase in AUC; however, no compound showed a significant increase in half-life or AUC. This led us to conclude that while oxidation of the aniline might be the primary site of first-pass metabolism, renal clearance via the core hydroxyl could play a more prominent role in the rapidly decreasing compound within the animals.

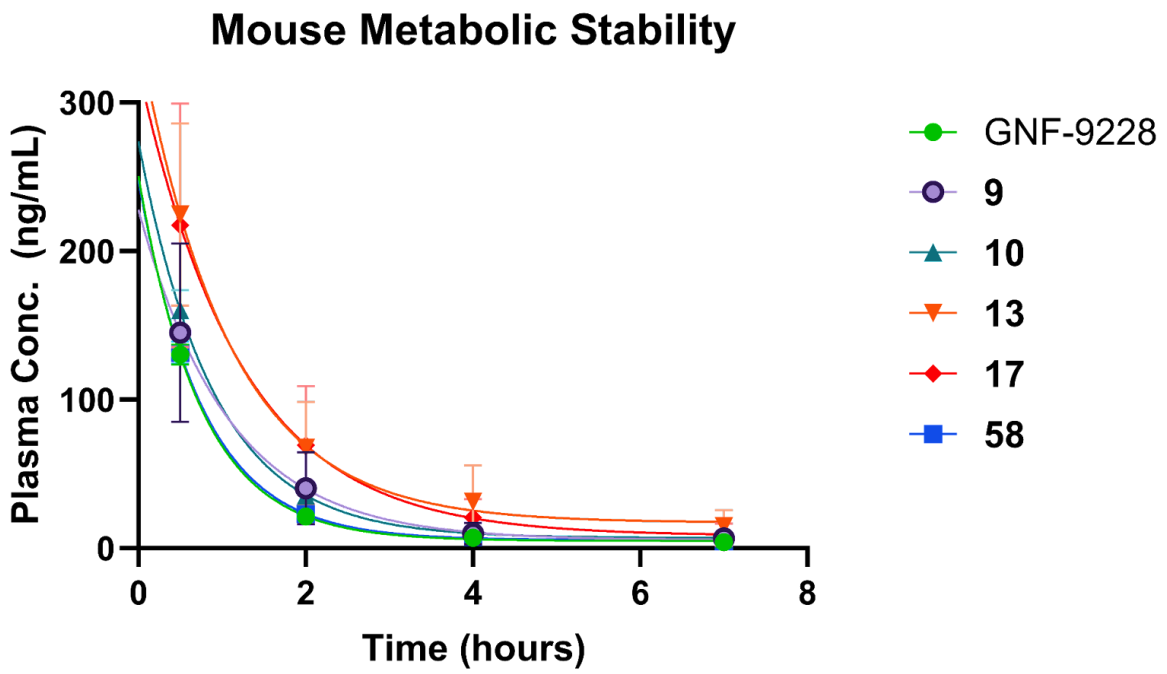

Figure 15. *In vivo* metabolic stability of GNF-9228 analogs shown as plasma concentration over hours.

3.7 Ex Vivo Efficacy

We also evaluated a subset of the compounds in a cadaveric islet-based cell proliferation assay. In contrast to the *in vivo* experiment, here islets were gathered from either rat or human donors and plated before exposure to compounds for 72 hours. As is consistent with the literature, the effect in human islets was much less pronounced that in the rodent islets. One striking characteristic of this study was the poor correlation between results obtained in either species. This was especially visible for compounds **7** and **19** where the difference was nearly 3-fold, underscoring the intricate dichotomy between roden and human islet biology. With very positive results in the luciferase and cytoxicity assay, we were eager to test **5b** in this assay system; however, much to our dismay, **5b** showed no significant effect on beta-cell proliferation in either species.

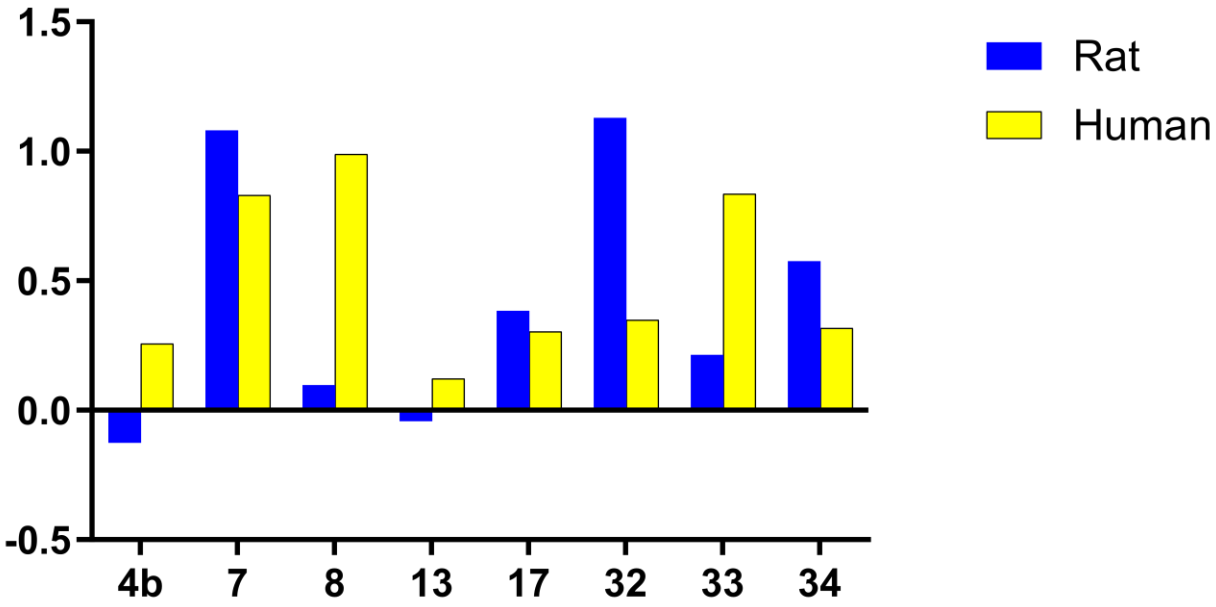

Figure 16. Percent of cells displaying EDU incorporation in *ex vivo* islet assays.

3.8 KinomeScan Data

Many studies focusing on beta cell proliferation tend to inhibit one or more kinases, with DYRK1A being a prominent target. Interestingly, recent research has demonstrated that Harmine, 5-IT, and GNF-4877 are not selective inhibitors of DYRK1A; rather, they function as pan-kinase inhibitors.[126] To further understand how our compound compares to these kinase inhibitors, we carried out a KinomeScan study (Table 8). The kinomic profiling revealed that GNF-9228 is somewhat selective; it displays a marked tendency to inhibit the CMGC (CDK/MAPK/GSK/CLK) and CK1 (Casein Kinase 1) kinase families (Figure 17A). Both of these families play pronounced roles in cell regulation. The CMGC kinase family, for instance, is critically involved in cell cycle control and signal transduction processes, while CK1s contribute

to signal transduction and cell differentiation.[127,128] In comparing the KinomeScan profile of GNF-9228, its profile was found to bear the most resemblance to that of Harmine.

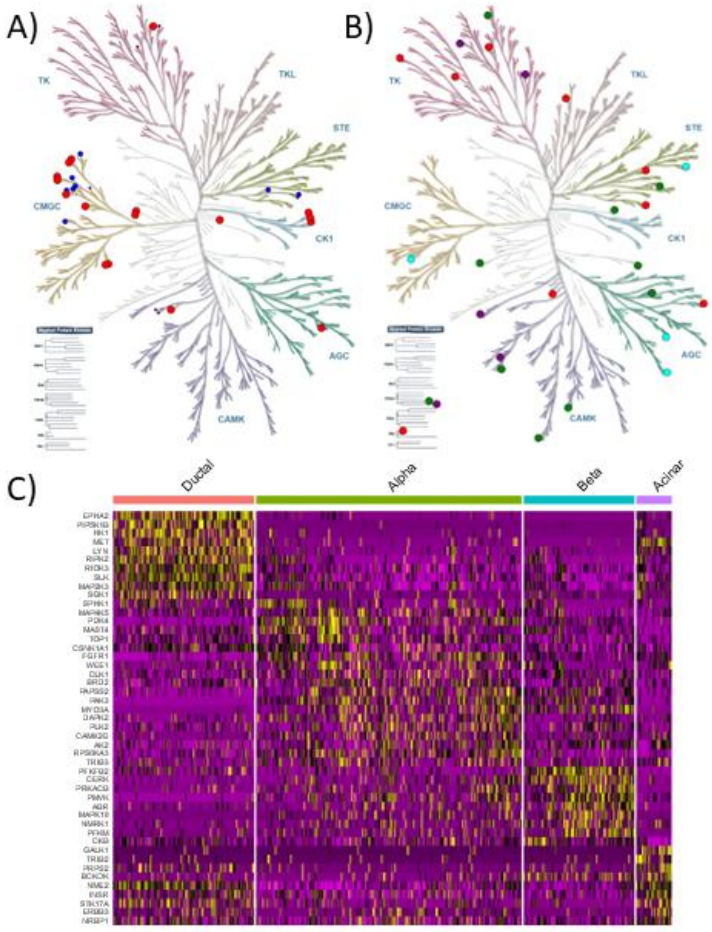

Figure 17. Kinome analysis of endocrine cells.[29] **A)** Kinmap of kinases inhibited by GNF-9228. Red dots are ≥ 90% inhibition, blue dots are 80-90% inhibition. **B)** Kinmap of kinases uniquely expression in various endocrine cell types. Red are ductal, green are alpha, cyan are beta, and purple are acinar cells. **C)** ScRNA seq profile of relative kinase expression in endocrine cells of T2D persons.

To understand how these pan-kinase inhibitors might selectively stimulate beta cells, we evaluated the differential expression of the human kinome within various Type II Diabetic human pancreatic cell types using published scRNA data (Figure 17C).[129] This analysis showed that only a small subset of the human kinome is uniquely upregulated in each cell type. Surprisingly, the CMGC and CK1 branches primarily inhibited by GNF-9228 were not

preferentially expressed in any of the endocrine cell lines. Furthermore, the subset of kinases that are upregulated in beta-cells is underrepresented in the KinomeScan data; however, these compounds generally do not inhibit the kinases unique to the other pancreatic tissue cell lines (Figure 17B)

3.9 Conclusions

Diabetes continues to be a global health issue, posing a challenge to millions of people worldwide. In spite of numerous advances in interventions aiming to enchance quality of life, a cure remains elusive. This underscores the critical need for ongoing research into curative therapeutic strategies for T2D. Our investigation has highlighted the utility of high-content islet imaging of *in vivo* dosed islets, which offers significant improvements over traditional histological analysis. The use of this method led to a more robust islet analysis, allowing us to quantify a larger number of cells, the size and shape of the islets, as well as the three-dimensional cell organization within them. Regrettably, even with these methodological advancements, our SAR efforts failed to produce an increase in the potency or metabolic stability of the GNF-9228 scaffold. Nevertheless, recognizing a potential correlation of the core hydroxyl with renal clearance provides an avenue for further studies. Moreover, the assessment of GNF-9228's influence on the human kinome allowed us to better understand its interactions within human cells. Even though our work with GNF-9228 did not yield the desired outcomes in terms of therapeutic improvement, our advanced use of islet imaging and kinome analysis represent important steps forward in the field of curative therapeutics for diabetes.

3.10 Experimental

3.10.1 Chemistry

3.10.1.1 General Synthesis of cyanoacetamides (Procedure A)[123,130]

To a vail containing a stir bar was added amine (1.20 eq), in ethanol (0.5 M) if a solid at room temperature, and ethyl 2-cyanoacetate (1 eq). The reaction was stirred for 18 hours. Thereafter, the crude material was purified by triteration through the addition of 2 mL of hexanes to the reaction mixture. Following 5 minutes of sonication, the precipitate was separated using vacuum filtration. The resulting solid was washed with hexanes (3x 2 mL). The residue was dried under vacuum and purified by flash chromatography when needed.

3.10.1.2 General synthesis of chromenone cores (Procedure B)[128]

To a flask equipped with a stir bar was added benzaldehyde (1 eq), cyanoacetamide (1.1 eq), and ethanol (0.5 M) in that order. Piperidine (1 mol%) was added, and the reaction was let stir for 18 hours at room temperature. The resulting precipitate was filtered and washed 3 times with ice-cold absolute EtOH. The residue was dried under vacuum and used without further purification.

3.10.1.3 General Synthesis of chromenones (Procedure C)[130]

To a flask equipped with a stir bar was added the desired aniline (1 eq), chromenone core (1 eq), and acetic acid (0.125 M) in that order. The reaction was let stir for 18 hours at RT. The precipitate was separated by filtration and then washed three times with ice-cold water, followed by three times with ether. The residue was dried under vacuum. When necessary, crude

residues were purified by normal phase column chromatography using a gradient of up to 10% methanol in DCM.

3.10.1.4 High Throughput Synthesis of Chromenones (Procedure D)

Six glass beads were added to each HPLC vial, and the vials were tared. Then, chromenone core in acetic acid (980 uL, 0.125M) was added to each vial, followed by aniline in methanol (99 uL, 1.25 M). Vials were capped and shaken on a LabeLine 3520 Orbit Shaker at 225 RPM for 18 hours. At this time, 500 uL of ice-cold water was added to each reaction, and the vials were centrifuged. The water was decanted, and the wash step repeated once more with water and once with ether. The precipitates were dried under vacuum and then lyophilized to remove the remaining water. The final residues were weighed before being solubilized in DMSO to a final concentration of 10 mM. The molecular weight and purity of the products were confirmed using UPLC/MS.

3.10.2 Biological Assays

3.10.2.1 Luciferase Assay [22]

Preliminary screening of synthesized compounds was conducted using 832/13-VGF-Luc cells, generously provided by Dr. Hans Hohmeier. To start the process, a Beckman-Coulter ECHO 655 system was used to dry spot a 2 mM stock solution of the compounds, dissolved in dimethyl sulfoxide (DMSO), onto white, clear-bottom, 384-well plates. Columns 1, 2, 23, and 24 of each plate were allocated for DMSO and GNF-9228 controls. Subsequently, the cells were seeded at 8000 cells per well in a volume of 20 μL of culture medium in the compound plates. Following an 18-hour incubation period, 10 μL of OneGlo (Promega) reagent was added to each well to

facilitate luminescence detection. The luminescent signal was quantified using an Envision plate reader (PerkinElmer). To ensure comparability and accuracy, the obtained data were normalized to the average values of the controls on each plate.

3.10.2.2 Live Cell ER-Cytotoxicity Assay

The experimental setup involved a 384-well format, with two columns of each plate dedicated to a positive control of GNF-9228 at a concentration of 10 μM. The last two columns were treated with 0.1% dimethyl sulfoxide (DMSO) and served as the negative control. To conduct this assay, 832/13 cells were seeded at 8000 cells in 40 uL per well. These cells were preincubated with 10 μM of the compound for a duration of 24 hours. Each compound was dosed in triplicate. Following the primary incubation, Thapsigargin was dispensed into each well at a concentration of 250 nM, utilizing an HPD300e system. Subsequently, the cells were incubated for an additional 24 hours. After a 24-hour incubation with Thapsigargin, 10 uL of a 5x solution containing Hoechst and Propidium iodide in media was added to each well, resulting in a final 5 ug/mL concentration for both dyes. Live cell imaging was carried out using an Arrayscan VTI system, and image analysis was performed using CellProfiler 4.2.1 software. Briefly, nuclei were identified as primary objects in the Hoechst channel, and intensity measurements within the nuclei were recorded in the Propidium Iodide channel. Cells were then categorized as either propidium iodide (PI) positive or negative based on predetermined staining thresholds. Non-viable cells were identified as those above the propidium iodide staining threshold, and readouts were expressed as the percentage of viable cells in each well. Plate-based normalization was implemented using the control columns present on each plate.

3.10.2.3 Ex-Vivo Islet Assays

Ex vivo were conducted as previously described.[22] In brief, islets were harvested and plated in microwell plates. Compounds were then added to produce a final concentration of 10 uM. EDU was added in the last 72h of cell culture after treatment with compounds of interest. After which, they were dispersed and imaged with the Cellomics CX5 High-Content (HC) cell-based imaging system.

3.10.2.4 In-Vivo Islet Assay

All animal protocols were approved by the Unvieristy of Michigan Committee on the Use and Care of Animals in accordance with AAALAC and AVMA guidelines. The *in vivo* islet assay was carried out in 30 week old, diet induced obesity (DIO) mice. The mice were maintained on high fat chow diet and were hosued on a 12-hour light/dark cycle. Mice were injected twice daily with an 80% PEG, 20% DMSO vehicle containing 50 mg/kg EDU. For animals treatment animals, the injected solution also contained 20mg/kg GNF-9228. After seven days of injections, islets were obtained through the Michigan Diabetes Research Center (MDRC) Islet Isolation Laboratory using established protocols.[102] Islets were then plated in 384-well Revvity PhenoPlates with media containing 10 uM EDU. After an overnight incubation, cells were stained, imaged, and analyzed as previously described.[75]

3.10.2.5 KinomeScan

The scanMAX kinome screen for GNF-9228 at 10 uM against 468 kinases, as detailed in Table S1, was performed by DiscoverX Corp. (Freemont, CA). In brief, this system uses a competition binding assay method to quantitatively measure the affinity of compounds for specific kinase

targets. Specially designed probes, tagged with a known binding ligand, are mixed with text compounds. Following immobilization and washing, the amount of kinase that remains bound to immobilized ligand is quantified.[137]

3.10.3 Pharmacokinetics

3.10.3.1 Metabolite ID Study

The metabolite ID study was performed by the UM PK core.

3.10.3.2 Microsomal Stability

The following procedure was applied to test compounds submitted for metabolic stability assessment in human liver microsomes. Eight reference compounds (atenolol, buspirone, imipramine, lidocaine, methoxyverapamil, propranolol, sulpiride, and verapamil) were incubated along with 88 test compounds in 96-well format. Liquid transfer steps were performed with a PP-550 MS 96-channel Personal Pipettor (Apricot Designs, Inc., Monrovia, CA, USA) under computer control. The substrate plate was prepared by addition of NADPH solution (500l, 4 mM) to each well of a 1.2 ml deep-well microtiter plate. Test compounds were diluted to 1 mM in acetonitrile from a 10 mM DMSO stock then dispensed (4 nmol each), by aid of an eight-channel Finnipipette® multipipettor (Thermo Labsystems, Helsinki, Finland) into 88 wells of the 1.2 ml deep-well substrate plate. Compounds were arrayed in the substrate microtiter plate in such a way as to leave the first column (eight wells) empty for reference compounds. Solutions of eight reference compounds (4 l, 1 mM) were added into the first column of the microtiter plate. The entire plate was mixed five times using the 96-channel pipettor and then agitated on a

plate shaker for 10 min. The solutions in the plate were then transferred into twelve 200l low-volume incubation plates (30 l each well) and pre-incubated at 37 ◦C for 5 min in a VWR incubator (VWR Scientific products, Cornelius, OR, USA). Pre-warmed (37 ◦C, 5 min) microsomal solution (2 mg/ml) was then added into all wells of the incubation plates (30l/well). The final incubation solutions contained 4M test compound or reference compound, 2 mM NADPH, 1 mg/ml (total protein) microsomes, and 50 mM phosphate (pH 7.4). The incubation plates were then incubated at 37 ◦C for 0, 5, 15, and 30 min, respectively. At each time point, three incubation plates were removed from the incubator and quenched immediately with an equal volume of ice-cold 0.3 M TCA. Quenched plates were centrifuged for 15 min at 420 rad/s in an Eppendorf 5804R centrifuge (Brinkman Instruments, Westbury, NY, USA) and the supernatants transferred to new 200l low-volume analytical plates for high throughput parallel LC/MS analysis.

3.10.3.3 In Vivo Mouse PK

Mouse PK was performed by the UM PK core. Compounds were dosed to mice in cassettes of four. Plasma concentration was monitored by LC-MS.

3.10.4 Single-cell RNA-Seq Quality Control and Analysis

Normalized cell count and metadata matrices were obtained for series GSE124742 through the Gene Expression Omnibus. Cells were filtered by <20% mitochondrial genes and Type II Diabetic cell labels (n=579 cells). Data were normalized and features were selected using the Seurat V4 package.[132] Dimensionality reduction was done by PCA (20 PCs), clusters were

selected by KNN, and clusters were labeled with assigned cell types based on key marker expression (GCG, INS, SST, PPY, GHRL, COL1A1, PRSS1, KRT19).

3.11 Supplemental Material

3.11.1 KinomeScan Results[133]

Table 8. Results from the KinomeScan assay.

Entrez Gene Symbol	Harmine	5-IT	GNF 4788	GNF-9228
AAK1	74	85	0.5	96
ABL1(E255K)-phosphorylated	93	19	6.7	79
ABL1(F317I)-nonphosphorylated	97	63	52	88
ABL1(F317I)-phosphorylated	91	43	31	100
ABL1(F317L)-nonphosphorylated	96	38	23	82
ABL1(F317L)-phosphorylated	100	21	13	89
ABL1(H396P)-nonphosphorylated	63	4.5	1.1	76
ABL1(H396P)-phosphorylated	87	14	7.3	100
ABL1(M351T)-phosphorylated	83	17	6.9	91
ABL1(Q252H)-nonphosphorylated	69	27	5.8	78
ABL1(Q252H)-phosphorylated	97	14	5.5	91
ABL1(T315I)-nonphosphorylated	76	12	4.3	100
ABL1(T315I)-phosphorylated	91	0.7	0	84
ABL1(Y253F)-phosphorylated	86	17	11	95
ABL1-nonphosphorylated	90	34	19	69
ABL1-phosphorylated	100	14	7.2	67
ABL2	89	100	83	94
ACVR1	95	47	0	84
ACVR1B	91	80	5.5	85
ACVR2A	82	95	4.5	73
ACVR2B	86	82	4	86
ACVRL1	100	75	1.6	100
ADCK3	88	100	43	75

ADCK4	93	31	56	100
AKT1	96	99	100	89
AKT2	80	97	100	100
AKT3	84	100	46	64
ALK	92	4.5	0.45	100
ALK(C1156Y)	87	5	3.6	68
ALK(L1196M)	100	17	12	99
AMPK-alpha1	77	63	44	78
AMPK-alpha2	94	40	53	93
ANKK1	78	19	0.2	99
ARK5	88	73	13	96
ASK1	99	100	100	97
ASK2	100	44	34	100
AURKA	85	38	0	43
AURKB	80	38	25	92
AURKC	59	62	7.2	85
AXL	82	25	0.65	54
BIKE	67	98	0	68
BLK	100	63	20	46
BMPR1A	79	84	6	100
BMPR1B	71	0.55	0.55	88
BMPR2	96	1.8	0.9	99
BMX	84	81	45	91
BRAF	100	60	5.5	88
BRAF(V600E)	90	58	4.6	81
BRK	95	100	94	77
BRSK1	92	18	100	34
BRSK2	93	19	90	49

BTK	100	59	42	100
BUB1	53	6.1	3.9	100
CAMK1	73	56	9.8	100
CAMK1B	100	7.8	1.2	87
CAMK1D	74	37	19	100
CAMK1G	84	75	6.1	100
CAMK2A	60	15	3.8	100
CAMK2B	42	11	1.6	100
CAMK2D	79	22	6.7	97
CAMK2G	91	34	14	98
CAMK4	100	29	70	100
CAMKK1	99	54	0.3	100
CAMKK2	100	57	0.25	100
CASK	76	56	9.5	71
CDC2L1	100	95	100	96
CDC2L2	93	100	97	96
CDC2L5	53	0	47	64
CDK11	83	16	0.95	12
CDK2	98	35	2.3	100
CDK3	100	16	0.75	95
CDK4	91	70	92	100
CDK4-cyclinD1	100	9.6	1.6	76
CDK4-cyclinD3	100	18	7.5	87
CDK5	95	39	32	99
CDK7	21	0.25	6	57
CDK8	55	22	0	12
CDK9	67	8.1	11	85
CDKL1	91	47	28	78

CDKL2	82	36	3.4	67
CDKL3	99	87	46	98
CDKL5	100	15	37	100
CHEK1	96	90	23	98
CHEK2	80	35	31	100
CIT	29	87	1.6	39
CLK1	0.35	4.2	0.25	2.1
CLK2	2.4	8.9	2.1	0.3
CLK3	24	34	1.6	16
CLK4	13	0.7	0	0.4
CSF1R	88	39	24	23
CSF1R-autoinhibited	100	33	9.1	23
CSK	79	73	5.9	100
CSNK1A1	5	0.85	0.15	9.1
CSNK1A1L	53	42	3	78
CSNK1D	13	9.6	0.8	7.8
CSNK1E	1.7	9.1	0	0.6
CSNK1G1	51	11	2	93
CSNK1G2	19	43	1.1	38
CSNK1G3	27	70	0.05	74
CSNK2A1	11	0	0	8.5
CSNK2A2	23	9.8	0	2.9
CTK	93	31	12	88
DAPK1	78	4.9	3.2	92
DAPK2	72	4.8	1.6	100
DAPK3	69	5.9	5.2	100
DCAMKL1	79	19	43	80
DCAMKL2	93	41	89	100

DCAMKL3	82	65	2.5	100
DDR1	88	99	8.3	100
DDR2	71	76	21	92
DLK	95	31	20	100
DMPK	90	100	1.1	100
DMPK2	98	85	60	85
DRAK1	35	63	1.8	46
DRAK2	73	51	0.9	91
DYRK1A	0	0.15	0.35	0
DYRK1B	6.1	3.9	0.35	3.5
DYRK2	3.2	0.2	0	15
EGFR	96	79	34	93
EGFR(E746-A750del)	96	56	18	80
EGFR(G719C)	95	99	45	54
EGFR(G719S)	93	100	42	74
EGFR(L747-E749del, A750P)	89	95	0	68
EGFR(L747-S752del, P753S)	100	97	0.8	59
EGFR(L747-T751del,Sins)	78	100	16	55
EGFR(L858R)	81	82	21	79
EGFR(L858R,T790M)	100	57	0	100
EGFR(L861Q)	82	91	18	65
EGFR(S752-I759del)	70	100	24	77
EGFR(T790M)	85	60	4.9	100
EIF2AK1	81	83	81	100
EPHA1	92	67	14	100
EPHA2	93	94	18	95
EPHA3	93	28	0.85	100
EPHA4	87	96	23	100

EPHA5	95	97	4.7	85
EPHA6	88	86	3.6	100
EPHA7	85	96	0.75	94
EPHA8	87	100	72	88
EPHB1	98	100	11	91
EPHB2	89	92	16	88
EPHB3	88	98	58	42
EPHB4	83	98	6.1	99
EPHB6	71	7	0	46
ERBB2	85	81	53	93
ERBB3	100	55	4.3	84
ERBB4	99	74	23	95
ERK1	99	88	100	90
ERK2	94	94	100	97
ERK3	99	78	100	85
ERK4	96	39	92	95
ERK5	100	66	10	89
ERK8	59	42	0.4	48
ERN1	85	0	0	100
FAK	100	98	16	100
FER	97	72	6.5	73
FES	84	98	31	97
FGFR1	91	12	17	78
FGFR2	91	56	49	97
FGFR3	94	55	65	100
FGFR3(G697C)	93	56	67	90
FGFR4	100	63	53	100
FGR	80	87	30	64

FLT1	94	57	4.2	83
FLT3	85	25	1.6	48
FLT3(D835H)	71	14	0	62
FLT3(D835V)	25	0.85	0	16
FLT3(D835Y)	67	3.3	0.2	21
FLT3(ITD)	79	6.7	0.15	37
FLT3(ITD,D835V)	72	0	0	43
FLT3(ITD,F691L)	78	0	0	30
FLT3(K663Q)	83	8	0.55	63
FLT3(N841I)	100	0	0	67
FLT3(R834Q)	97	5.1	5	100
FLT3-autoinhibited	100	0.75	24	100
FLT4	95	70	0	93
FRK	100	100	34	77
FYN	97	100	27	81
GAK	75	45	1.4	56
GCN2(Kin.Dom.2,S808G)	97	76	4.7	58
GRK1	67	22	1.4	77
GRK2	100	9.9	46	100
GRK3	100	0	23	100
GRK4	67	96	7.2	71
GRK7	100	11	0.35	95
GSK3A	88	35	0	16
GSK3B	71	66	0.15	96
HASPIN	2	0	22	0
HCK	88	83	15	64
HIPK1	21	0.45	0.2	3.1
HIPK2	8.6	0.1	0.05	2.3

HIPK3	9.4	1.8	0.8	12
HIPK4	80	28	6.1	26
HPK1	74	49	2.5	84
HUNK	76	100	100	100
ICK	77	16	0	100
IGF1R	100	100	100	88
IKK-alpha	81	0.4	55	100
IKK-beta	95	6.5	59	100
IKK-epsilon	100	99	6	54
INSR	100	13	26	97
INSRR	91	53	32	83
IRAK1	17	0	0	67
IRAK3	35	29	2.7	93
IRAK4	85	0.05	0.5	80
ITK	91	74	44	100
JAK1(JH1domain-catalytic)	100	71	12	96
JAK1(JH2domain-pseudokinase)	63	36	0.6	50
JAK2(JH1domain-catalytic)	92	4.8	0	100
JAK3(JH1domain-catalytic)	61	20	0.25	100
JNK1	41	2.1	0.45	83
JNK2	58	1.8	5.5	100
JNK3	80	0.55	1.6	88
KIT	86	32	21	56
KIT(A829P)	100	9.2	1.6	100
KIT(D816H)	92	32	0	100
KIT(D816V)	91	52	0.2	54
KIT(L576P)	92	22	10	61
KIT(V559D)	95	20	9.3	45

KIT(V559D,T670I)	92	26	13	100
KIT(V559D,V654A)	91	99	56	66
KIT-autoinhibited	88	54	88	100
LATS1	94	46	40	73
LATS2	83	19	16	61
LCK	96	81	35	44
LIMK1	97	89	100	90
LIMK2	100	88	72	83
LKB1	91	59	2.8	93
LOK	86	38	12	58
LRRK2	100	0	0	36
LRRK2(G2019S)	100	0.5	0.7	100
LTK	80	43	5.3	67
LYN	89	83	80	73
LZK	86	72	64	100
MAK	92	92	0.3	93
MAP3K1	98	35	14	97
MAP3K15	68	76	14	100
MAP3K2	77	0.7	0.3	93
MAP3K3	93	0.25	0	90
MAP3K4	93	98	43	99
MAP4K2	100	1.7	0.1	68
MAP4K3	80	67	8.9	81
MAP4K4	80	78	2.6	73
MAP4K5	80	68	1.9	77
MAPKAPK2	72	100	46	100
MAPKAPK5	100	70	12	100
MARK1	82	41	40	77

MARK2	88	31	2.8	100
MARK3	91	97	3.1	100
MARK4	76	33	20	80
MAST1	85	34	5.1	96
MEK1	79	0.1	49	12
MEK2	96	0.1	34	21
MEK3	58	0	0	64
MEK4	90	1.3	1.1	100
MEK5	79	0.1	2.1	13
MEK6	100	5.1	14	95
MELK	100	68	10	87
MERTK	83	44	0	61
MET	100	100	8.9	25
MET(M1250T)	99	89	1.4	12
MET(Y1235D)	66	60	0.1	52
MINK	67	0	0	84
MKK7	100	15	56	100
MKNK1	79	49	69	72
MKNK2	22	0	63	57
MLCK	93	68	100	99
MLK1	100	92	5.9	87
MLK2	90	32	0.15	78
MLK3	100	69	0	79
MRCKA	93	95	82	92
MRCKB	92	100	50	100
MST1	83	48	0.85	67
MST1R	92	37	3.9	86
MST2	96	14	3.5	97

MST3	97	0.5	7.8	100
MST4	93	12	2	100
MTOR	84	100	28	83
MUSK	85	94	100	85
MYLK	59	9	0	74
MYLK2	95	88	100	63
MYLK4	59	100	100	51
MYO3A	91	50	4.7	100
MYO3B	87	94	0.3	75
NDR1	92	0	51	89
NDR2	99	0.5	69	98
NEK1	100	78	97	77
NEK10	53	1.5	0	100
NEK11	82	57	95	100
NEK2	89	82	80	100
NEK3	80	12	28	55
NEK4	97	48	82	100
NEK5	94	87	59	79
NEK6	100	80	100	75
NEK7	100	46	60	100
NEK9	95	69	52	100
NIK	73	37	0.05	88
NIM1	94	59	67	86
NLK	93	84	46	86
OSR1	100	0.45	53	100
p38-alpha	95	100	100	100
p38-beta	85	98	100	66
p38-delta	96	38	87	91

p38-gamma	43	39	53	76
PAK1	73	90	27	100
PAK2	47	58	15	100
PAK3	78	44	12	52
PAK4	76	33	0.2	100
PAK6	75	39	2.2	100
PAK7	93	32	0	100
PCTK1	100	25	74	100
PCTK2	100	29	78	94
PCTK3	90	37	100	80
PDGFRA	90	24	32	100
PDGFRB	84	29	5.3	45
PDPK1	100	95	44	90
PFCDPK1(P.falciparum)	59	4.3	3.1	50
PFPK5(P.falciparum)	53	38	51	61
PFTAIRE2	93	100	77	99
PFTK1	96	34	91	82
PHKG1	100	27	29	100
PHKG2	66	4.9	40	100
PIK3C2B	97	97	0	100
PIK3C2G	52	65	19	73
PIK3CA	91	90	6	100
PIK3CA(C420R)	88	100	20	10
PIK3CA(E542K)	62	45	6.4	97
PIK3CA(E545A)	89	90	16	100
PIK3CA(E545K)	74	79	9.1	48
PIK3CA(H1047L)	68	57	0	78
PIK3CA(H1047Y)	87	96	5.3	94

PIK3CA(I800L)	71	51	0	49
PIK3CA(M1043I)	86	65	1.2	100
PIK3CA(Q546K)	63	33	3.6	100
PIK3CB	50	58	78	100
PIK3CD	72	85	36	100
PIK3CG	49	33	0.35	68
PIK4CB	12	34	0	33
PIKFYVE	99	97	1.9	71
PIM1	45	48	0.95	28
PIM2	39	96	8.8	7.5
PIM3	43	55	9.9	22
PIP5K1A	86	100	7.5	57
PIP5K1C	38	67	0.3	8.6
PIP5K2B	85	96	7.1	100
PIP5K2C	36	44	3.1	65
PKAC-alpha	88	75	15	89
PKAC-beta	95	70	4.3	100
PKMYT1	81	100	95	60
PKN1	98	38	5.7	80
PKN2	91	70	1.8	100
PKNB(M.tuberculosis)	85	6.8	3.7	94
PLK1	93	51	39	100
PLK2	96	52	50	10
PLK3	75	68	36	92
PLK4	77	22	0	92
PRKCD	90	42	0.05	80
PRKCE	91	15	0	100
PRKCH	87	57	0.3	86

PRKCI	100	11	3.9	10
PRKCQ	76	72	4.4	97
PRKD1	92	57	100	100
PRKD2	87	1.1	93	100
PRKD3	93	15	47	100
PRKG1	67	77	8.1	100
PRKG2	84	73	0	100
PRKR	100	31	23	91
PRKX	100	97	69	100
PRP4	91	100	4.6	78
PYK2	100	100	38	100
QSK	73	59	8.4	100
RAF1	89	100	79	98
RET	91	61	0.3	82
RET(M918T)	91	51	0.05	78
RET(V804L)	94	59	0.05	85
RET(V804M)	92	40	1.3	100
RIOK1	74	66	0.9	68
RIOK2	62	16	0	56
RIOK3	71	61	0.35	88
RIPK1	97	100	100	75
RIPK2	98	100	8.9	70
RIPK4	57	0	0	51
RIPK5	77	4.8	0	89
ROCK1	26	7.3	20	100
ROCK2	43	3.1	18	10
ROS1	94	49	0.55	68
RPS6KA4(Kin.Dom.1-N-terminal)	94	41	1.3	99

RPS6KA4(Kin.Dom.2-C-terminal)	40	1.4	47	10
RPS6KA5(Kin.Dom.1-N-terminal)	90	78	0.1	93
RPS6KA5(Kin.Dom.2-C-terminal)	97	100	61	99
RSK1(Kin.Dom.1-N-terminal)	91	40	0.4	90
RSK1(Kin.Dom.2-C-terminal)	67	23	8.8	100
RSK2(Kin.Dom.1-N-terminal)	72	11	0.55	50
RSK2(Kin.Dom.2-C-terminal)	80	100	10	38
RSK3(Kin.Dom.1-N-terminal)	81	43	0.15	100
RSK3(Kin.Dom.2-C-terminal)	89	21	2.1	100
RSK4(Kin.Dom.1-N-terminal)	100	13	1.5	100
RSK4(Kin.Dom.2-C-terminal)	84	36	32	10
S6K1	57	7.5	2.1	100
SBK1	100	7.6	84	93
SGK	84	2.6	0.85	80
SgK110	100	64	100	74
SGK2	100	3.2	0	100
SGK3	56	2	1.6	90
SIK	99	100	95	91
SIK2	75	100	65	96
SLK	93	48	0	71
SNARK	95	6	3.2	100
SNRK	71	34	53	99
SRC	90	92	7	45
SRMS	100	28	34	92
SRPK1	79	71	0	82
SRPK2	100	100	0	10
SRPK3	84	93	5.7	77
STK16	72	2.9	0.65	99

STK33	96	70	7.4	67
STK35	75	62	2	100
STK36	84	92	32	72
STK39	81	0	59	95
SYK	98	100	0.05	76
TAK1	100	1.9	0.1	64
TAOK1	100	2.1	2.9	45
TAOK2	100	18	3.2	88
TAOK3	100	5.3	0.8	96
TBK1	98	93	0	95
TEC	95	100	100	94
TESK1	86	87	52	93
TGFBR1	91	52	0.2	96
TGFBR2	78	70	0.05	58
TIE1	97	63	17	87
TIE2	94	62	11	85
TLK1	89	5	59	100
TLK2	100	1.9	90	100
TNIK	92	9.1	0.1	98
TNK1	80	100	24	76
TNK2	98	94	94	98
TNNI3K	98	93	53	75
TRKA	100	0.45	0	63
TRKB	100	0.1	5.2	100
TRKC	99	4.3	1.3	92
TRPM6	75	39	25	100
TSSK1B	100	92	34	100
TSSK3	87	54	28	96

TTK	73	3.4	2.9	100
TXK	93	69	27	73
TYK2(JH1domain-catalytic)	96	0	0	10
TYK2(JH2domain-pseudokinase)	24	67	26	96
TYRO3	93	74	69	94
ULK1	89	0.3	46	100
ULK2	89	1.1	26	94
ULK3	98	0.45	3.7	98
VEGFR2	78	6.3	0.45	10
VPS34	13	26	0.05	50
VRK2	100	28	0	100
WEE1	90	93	100	80
WEE2	100	100	68	100
WNK1	100	100	93	85
WNK2	79	71	72	100
WNK3	100	100	97	76
WNK4	100	88	96	100
YANK1	100	31	1.4	100
YANK2	89	98	2.5	64
YANK3	77	84	8.9	64
YES	97	85	17	91
YSK1	100	9.8	52	99
YSK4	25	0	0	34
ZAK	93	95	11	90
ZAP70	92	84	0	92

3.11.2 Cell Assay Results

Table 9. Complete list of GNF-9228 analogs and their results in the cell-based assays.

Cmpd	R	R1	R1	%Luc	%Via	MW	cLogP	HBA	HBD	Rot
9228	3-OH	H	4-CH3	100.58	104.42	294.31	2.94	3	2	2
7	3-OH	H	2-F	52.19	49.24	298.27	2.56	3	2	2
8	3-OH	H	3-F	18.06	9.31	298.27	2.56	3	2	2
9	3-OH	H	2,4-F	28.98	123.55	316.26	2.71	3	2	2
10	3-OH	H	2,5-F	39.87	45.87	316.26	2.71	3	2	2
11	3-OH	H	2,6-F	14.49	100.87	316.26	2.71	3	2	2
12	3-OH	H	2,6-F, 4-OMe	25.52	79.05	346.29	2.55	4	2	3
13	3-OH	H	2-F, 4-CN	8.86	98.54	323.28	2.42	4	2	2
14	3-OH	H	4-OEt	58.06	111.26	324.34	2.62	4	2	4
15	3-OH	H	4-OCF3	60.05	-15.24	364.28	3.85	4	2	4
16	3-OH	H	4-tbutyl	46.42	135.60	336.39	3.97	3	2	3
4b	3-OH	Cyclohexyl	---	39.88	95.39	286.33	2.30	3	3	2
17	3-OH	H	4-CN	51.25	-1.51	305.29	2.28	4	2	2
18	3-OH	H	3-CN	6.22	3.47	305.29	2.28	4	2	2
19	3-OCH3	H	4-CN	25.87	115.85	319.32	2.42	4	1	3
20	3-H	H	4-CN	3.85	-10.78	289.29	2.58	3	1	2
21	3-Me	H	4-CN	29.41	-22.12	303.32	3.09	3	1	2
22	3-t-butyl	H	4-CN	15.86	-22.19	345.40	4.13	3	1	3
23	2-OH	H	4-CN	8.38	-29.16	305.29	2.93	4	2	2
24	4-OH	H	4-CN	4.84	-29.16	305.29	2.28	4	2	2
25	3-F	H	4-CN	15.72	-20.87	307.28	2.72	3	1	2
26	3-Cl	H	4-CN	11.45	-10.18	323.74	3.19	3	1	2

27	3-Br	H	4-CN	26.65	-3.25	368.19	3.35	3	1	2
5c	3-OH	Cyclopropyl	---	7.60	96.28	244.25	0.96	3	3	2
5d	3-OH	Cyclobutyl	---	30.20	79.69	258.28	1.41	3	3	2
5e	3-OH	Cyclopentyl	---	30.24	83.99	272.30	1.85	3	3	2
5f	3-OH	Cycloheptyl	---	21.71	18.86	300.36	2.74	3	3	2
5g	2-OH	Cyclohexyl	---	8.53	-7.59	286.33	2.95	3	3	2
5h	4-OH	Cyclohexyl	---	9.78	-16.45	286.33	2.30	3	3	2
28	3-OH	H	2,3-F	30.56	32.65	316.26	2.71	3	2	2
29	3-OH	H	2,4,6-F	20.57	71.90	334.25	2.85	3	2	2
30	3-OH	H	3,4,5-F	16.24	79.85	334.25	2.85	3	2	2
31	3-OH	H	3,5-F	8.04	58.89	316.26	2.71	3	2	2
32	3-OH	H	2-Cl	19.07	54.00	314.73	3.03	3	2	2
33	3-OH	H	3-Cl	20.03	29.72	314.73	3.03	3	2	2
34	3-OH	H	4-Cl	14.48	107.46	314.73	3.03	3	2	2
35	3-OH	H	2,3-Cl	15.78	53.12	349.17	3.63	3	2	2
36	3-OH	H	2,5-Cl	2.55	12.97	349.17	3.63	3	2	2
37	3-OH	H	3,4-Cl	0.59	48.11	349.17	3.63	3	2	2
38	3-OH	H	2-Me, 4-Cl	14.75	45.55	328.75	3.54	3	2	2
39	3-OH	H	2-OMe, 4-Cl	-0.78	107.77	344.75	2.87	4	2	3
40	3-OH	H	3-OH, 4-Cl	0.18	43.51	330.72	2.72	4	3	2
41	3-OH	H	3-OMe, 4-Cl	-3.90	50.27					
42	3-OH	H	3-Cl, 5-F	6.29	49.28	332.72	3.17	3	2	2
43	3-OH	H	3-Cl, 5-CF3	-2.33	77.60	382.72	3.90	3	2	3
44	3-OH	H	3-Cl, 5-OCH3	11.38	29.62	344.75	2.87	4	2	3

			3-Cl, 5-							
45	3-OH	H	CH3	3.28	60.77	328.75	3.54	3	2	2
46	3-OH	H	3-CN, 5-Cl	5.01	85.71	339.74	2.88	4	2	2
			2-Cl, 5-							
47	3-OH	H	OCH3	4.38	18.83	344.75	2.87	4	2	3
			2-Cl, 4-							
48	3-OH	H	CH3	27.83	7.53	328.75	3.54	3	2	2
49	3-OH	H	2-Cl, 4-Br	20.34	19.47	393.62	3.79	3	2	2
50	3-OH	H	4-Br	1.73	50.90	359.18	3.19	3	2	2
51	3-OH	H	3,5-CF3	-12.90	110.12	416.28	4.18	3	2	4
52	3-OH	H	2,5-CH3	2.48	29.75	308.34	3.45	3	2	2
53	3-OH	H	3,4-OCH3	8.21	55.86	340.34	2.11	5	2	4
54	3-OH	H	3-Alkyl	16.52	71.75	304.31	2.57	3	2	2
			2-COOH,							
55	3-OH	H	6-CH3	3.65	39.38	338.32	2.59	5	3	3
56	3-OH	H	3-CONH2	10.98	114.63	323.31	1.27	4	3	3
			4-							
57	3-OH	H	NCOCH3	21.78	81.54	337.34	1.66	4	3	3
58	3-OH	H	4-CD3	90.29	39.11	297.33	2.94	3	2	2
			3-CN,4-							
59	3-OH	H	CH3	10.07	82.50	319.32	2.79	4	2	2
			2-Pyr, 4-							
60	3-OH	H	CN	9.34	4.36	306.28	1.65	5	2	2
61	3-OH	H	4-O-n-hex	33.83	60.51	366.42	4.03	4	2	7
62	3-OH	Cyclohexyl	Cyclohexyl	0.65	16.98	368.48	4.32	3	2	3
63	3-Pyr	H	4-CN	7.00	23.64	290.28	1.36	4	1	2
64	3-Pyr	H	2-F, 4-CN		3.14	308.27	1.51	4	1	2
65	3-CN	H	4-CN	23.14	-38.61	314.30	2.44	4	1	2

66	3-CN	H	4-CH3	7.45	85.75	303.32	3.09	3	1	2
67	3-CN	H	4-OCF3	3.50	33.57	373.29	4.01	4	1	4
68	3-O-n-butyl	H	CH3	12.54	54.32	350.42	4.41	3	1	6

3.11.3 Chemical Synthesis

All reagents were used as received from commercial sources unless otherwise noted. ^{1}H spectra were obtained in DMSO-d_6 or $CDCl_3$ at room temperature, unless noted otherwise, on a Varian Inova 500 MHz instrument. Chemical shifts were recorded in parts per million (ppm) on the δ scale from the solvent peaks. Mass spectra data and retention times, recorded in minutes, were obtained on an Agilent 1290 Infinity UPLC and 6520 Q-TOF system with an Agilent Zorbax Eclipse Plus-C18 column (2.1x50 mm, 1.8 micron)with the gradient 10% MeOH/water(1 min) 10-90% MeOH/Water (4 min), and 90% MeOH/Water (2 min).

3.11.3.1 Cyanoacetamides (4a-d)

2-cyano-N-cyclobutylacetamide (4a)

Following Procedure A: To a vial was added cyclobutamine (417 mg, 5.86 mmol, 1.25 eq) and ethyl 2-cyanoacetate (530 mg, 4.69 mmol, 1 eq). Reaction was let stir for 18 hrs. Hexanes (2 mL) were added and the vial was sonicated for 5 minutes. Vacuum filtration was used to isolate and dry **4a** as a white solid (536.2 mg, 3.88 mmol, 82.8%). This material was used without further purification. ^{1}H NMR (499 MHz, DMSO-d_6) δ 8.46 (d, J = 7.0 Hz, 1H), 4.14 (tdd, J = 8.8, 7.6,

1.1 Hz, 1H), 3.55 (s, 2H), 2.15 (dtt, *J* = 8.6, 7.5, 2.9 Hz, 2H), 1.92 – 1.80 (m, 2H), 1.68 – 1.55 (m, 2H).

2-cyano-N-cyclopentylacetamide (4b)

Following Procedure A: To a vial was added cyclobutamine (479 mg, 5.62 mmol, 1.20 eq) and ethyl 2-cyanoacetate (530 mg, 4.69 mmol, 1 eq). Reaction was let stir for 18 hrs. Hexanes (2 mL) were added and the vial was sonicated for 5 minutes. Vacuum filtration was used to isolate and dry **4b** as a tan solid (630.4 mg, 4.14 mmol, 88.4%). This material was used without further purification. ^{1}H NMR (499 MHz, DMSO-d_6) δ 8.18 (d, *J* = 7.1 Hz, 1H), 3.96 (h, *J* = 6.8 Hz, 1H), 3.55 (s, 2H), 3.29 (s, 0H), 1.85 – 1.73 (m, 2H), 1.67 – 1.54 (m, 2H), 1.57 – 1.44 (m, 2H), 1.42 – 1.30 (m, 2H).

2-cyano-N-cyclohexylacetamide (4c)

Following Procedure A: To a vial was added cyclobutamine (1.58 g, 15.9 mmol, 1.20 eq) and ethyl 2-cyanoacetate (1.50 g, 13.3 mmol, 1 eq). Reaction was let stir for 18 hrs. Hexanes (6 mL) was added and the vial was sonicated for 5 minutes. Vacuum filtration was used to isolate and dry **4c** as a tan solid (2.07 g, 12.44 mmol, 93.8%). This material was used without further purification. ^{1}H NMR (499 MHz, DMSO-d_6) δ 8.10 (d, *J* = 7.7 Hz, 1H), 3.58 – 3.45 (m, 2H), 1.73 (dd, *J* = 12.7, 3.9 Hz, 2H), 1.72 – 1.61 (m, 2H), 1.53 (dt, *J* = 12.8, 3.7 Hz, 1H), 1.32 – 1.20 (m, 2H), 1.19 – 1.06 (m, 3H).

2-cyano-N-cycloheptylacetamide (4d)

Following Procedure A: To a vial was added cycloheptanamine (626 mg, 5.53 mmol, 1.18 eq) and ethyl 2-cyanoacetate (530 mg, 4.69 mmol, 1 eq). Reaction was let stir for 18 hrs. Hexanes (2 mL) were added and the vial was sonicated for 5 minutes. Vacuum filtration was used to isolate and dry **4d** as a white solid (595.1 mg, 3.30 mmol, 70.5%). This material was used without further purification. ^{1}H NMR (499 MHz, DMSO-d_6) δ 8.14 (d, J = 7.7 Hz, 1H), 3.70 (qd, J = 8.5, 4.2 Hz, 1H), 3.55 (s, 2H), 1.76 (ddt, J = 10.7, 7.2, 3.2 Hz, 3H), 1.63 – 1.52 (m, 3H), 1.51 (ddd, J = 15.2, 8.0, 3.2 Hz, 1H), 1.43 – 1.33 (m, 5H).

3.11.3.2 Chromenone Cores (5a-u)

7-hydroxy-2-imino-2H-chromene-3-carboxamide (5a)

Following procedure B: To a vial was added 2,4-dihydoxybenzaldehyde (7.5 g, 54.3 mmol, 1 eq), 2-cyanoacetamide (5.02 g, 59.7 mmol, 1.1 eq), ethanol (110 mL, 0.50 M), and a catalytic amount of piperidine (1 mol%) was added in that order. After 18 hours, the precipitate was filtered, washed, then dried under vacuum to yield **5a** (5.56 g, 27.25 mmol, 50.2%) as a tan solid. The crude product was used without purification or characterization, following literature precedent.

N-cyclohexyl-7-hydroxy-2-imino-2H-chromene-3-carboxamide (5b)

To a vail containing a stir bar was added cyclohexanamine (88.5 mg, 892.7 µmol, 0.95 eq) and ethyl 2-cyanoacetate (106.5 mg, 939.7 µmol, 1 eq). The reaction was stirred for 24 hours. After that time, 2,4-dihydoxybenzaldehyde (129.8 mg, 939.7 µmol, 1 eq), ethanol (1.88 mL, 0.50 M), and a catalytic amount of piperidine (1 mol%) were added, to the same vial, in that order. After 18 hours, the reaction was condensed via rotovap and purified via column chromatography (0% to 30% Methanol:DCM gradient) to yield **5b** (94.0 mg, 330 µmol, 35%) as a yellow solid. ^{1}H NMR (499 MHz, DMSO-d_6) δ 8.75 (s, 1H), 8.55 (d, *J* = 7.9 Hz, 1H), 7.79 (d, *J* = 8.6 Hz, 1H), 6.85 (dd, *J* = 8.7, 2.3 Hz, 1H), 6.77 (d, *J* = 2.4 Hz, 1H), 3.78 (d, *J* = 7.7 Hz, 1H), 3.27 (s, 4H), 1.86 – 1.78 (m, 2H), 1.68 – 1.61 (m, 2H), 1.53 (d, *J* = 11.1 Hz, 1H), 1.40 – 1.24 (m, 3H), 1.27 – 1.17 (m, 1H).

N-cyclopropyl-7-hydroxy-2-imino-2H-chromene-3-carboxamide (5c)

To a vail containing a stir bar was added cyclopropanamine (56.4 mg, 988.6 µmol, 1.05 eq) and ethyl 2-cyanoacetate (106.5 mg, 941.5 µmol, 1 eq). The reaction was stirred for 22 hours. Thereafter, the crude material was purified by triteration through the addition and decanting of 1 mL of hexanes to the reaction mixture, 3 times. To that same vial was added 2,4-dihydoxybenzaldehyde (117.0 mg, 847.3 µmol, 0.9 eq), ethanol (1.883 mL, 0.50 M), and a catalytic amount of piperidine (1 mol%) was added in that order. After 18 hours, the precipitate was filtered, washed, then dried under vacuum to yield **5c** (170.0 mg, 696 µmol, 73.9%) as a yellow solid.The crude product was used without purification or characterization.

N-cyclobutyl-7-hydroxy-2-imino-2H-chromene-3-carboxamide (5d)

Following procedure B: To a vial was added 2,4-dihydoxybenzaldehyde (100 mg, 724 µmol, 1 eq), **3a** (110 mg, 796 µmol, 1.1 eq), ethanol (1.45 mL, 0.50 M), and a catalytic amount of piperidine (1 mol%) was added in that order. After 18 hours, the precipitate was filtered, washed, then dried under vacuum to yield **5d** (78.6 mg, 304 µmol, 42.0%) as a yellow solid. The crude product was used without purification or characterization.

N-cyclopentyl-7-hydroxy-2-imino-2H-chromene-3-carboxamide (5e)

Following procedure B: To a vial was added 2,4-dihydoxybenzaldehyde (100 mg, 724 µmol, 1 eq), **3b** (121 mg, 796 µmol, 1.1 eq), ethanol (1.45 mL, 0.50 M), and a catalytic amount of piperidine (1 mol%) was added in that order. After 18 hours, the precipitate was filtered, washed, then dried under vacuum to yield **5e** (28.8 mg, 106 µmol, 14.6%) as a yellow solid. The crude product was used without further purification. ^{1}H NMR (499 MHz, DMSO-d_6) δ 10.57 (s, 1H), 10.32 (d, J = 7.2 Hz, 1H), 8.69 (s, 1H), 8.29 (d, J = 5.7 Hz, 1H), 7.99 (t, J = 7.5 Hz, 0H), 7.56 (d, J = 8.4 Hz, 1H), 6.67 (d, J = 8.3 Hz, 0H), 6.54 (s, 1H), 6.43 – 6.36 (m, 0H), 3.43 (qd, J = 7.0, 4.8 Hz, 1H), 3.29 (s, 1H), 1.94 – 1.81 (m, 1H), 1.84 (s, 1H), 1.68 – 1.55 (m, 3H), 1.50 (s, 1H), 1.42 (dt, J = 12.6, 6.1 Hz, 1H).

N-cycloheptyl-7-hydroxy-2-imino-2H-chromene-3-carboxamide (5f)

Following procedure B: To a vial was added 2,4-dihydoxybenzaldehyde (100 mg, 724 µmol, 1 eq), **4d** (144 mg, 796 µmol, 1.1 eq), ethanol (1.45 mL, 0.50 M), and a catalytic amount of piperidine (1 mol%) was added in that order. After 18 hours, the precipitate was filtered, washed, then dried under vacuum to yield **5f** (32.4 mg, 108 µmol, 14.9%) as a yellow solid. The crude product was used without further purification. ^{1}H NMR (499 MHz, DMSO-d_6) δ 10.58 (s, 1H), 10.47 (d, J = 7.7 Hz, 1H), 8.73 (s, 1H), 8.31 (t, J = 12.9 Hz, 2H), 8.00 (d, J = 8.8 Hz, 0H), 7.56 (d, J = 8.5 Hz, 1H), 6.67 (dd, J = 8.6, 2.2 Hz, 1H), 6.55 (d, J = 2.3 Hz, 1H), 6.43 – 6.36 (m, 1H), 4.33 (tq, J = 16.1, 8.1 Hz, 2H), 3.46 – 3.40 (m, 1H), 3.29 (s, 1H), 2.26 (q, J = 9.2, 8.1 Hz, 2H), 2.19 – 2.02 (m, 2H), 1.95 – 1.83 (m, 2H), 1.73 – 1.56 (m, 2H), 1.05 (t, J = 7.0 Hz, 2H).

N-cyclohexyl-8-hydroxy-2-imino-2H-chromene-3-carboxamide (5g)

Following procedure B: To a vial was added 2,3-dihydoxybenzaldehyde (100 mg, 724 µmol, 1 eq), **3c** (132 mg, 796 µmol, 1.1 eq), ethanol (1.45 mL, 0.50 M), and a catalytic amount of piperidine (1 mol%) was added in that order. After 18 hours, the precipitate was filtered, washed, then dried under vacuum to yield **5g** (25.9 mg, 90.5 µmol, 12.5%) as a yellow solid. The crude product was used without purification or characterization.

N-cyclohexyl-6-hydroxy-2-imino-2H-chromene-3-carboxamide (5h)

Following procedure B: To a vial was added 2,5-dihydoxybenzaldehyde (100 mg, 724 µmol, 1 eq), **4c** (132 mg, 796 µmol, 1.1 eq), ethanol (1.45 mL, 0.50 M), and a catalytic amount of piperidine (1 mol%) was added in that order. After 18 hours, the precipitate was filtered, washed, then dried under vacuum to yield **5h** (158.0 mg, 551.8 µmol, 76.2%) as a yellow solid. The crude product was used without purification or characterization.

8-hydroxy-2-imino-2H-chromene-3-carboxamide (5i)

Following procedure B: To a vial was added 2,3-dihydoxybenzaldehyde (500 mg, 3.62 mmol, 1 eq), 2-cyanoacetamide (335 mg, 3.92 mmol, 1.1 eq), ethanol (7.24 mL, 0.50 M), and a catalytic amount of piperidine (1 mol%) was added in that order. After 18 hours, the precipitate was filtered, washed, then dried under vacuum to yield **5i** (606.6 mg, 2.97 mmol, 82.1%) as a tan solid. The crude product was used without further purification. ^{1}H NMR (499 MHz, DMSO-d_6) δ 9.87 (s, 2H), 9.58 (s, 1H), 8.69 (s, 1H), 8.33 (s, 1H), 7.76 (s, 1H), 7.15 (dd, J = 6.6, 2.5 Hz, 1H), 7.03 (h, J = 6.5, 5.9 Hz, 2H).

6-hydroxy-2-imino-2H-chromene-3-carboxamide (5j)

Following procedure B: To a vial was added 2,5-dihydoxybenzaldehyde (500 mg, 3.62 mmol, 1 eq), 2-cyanoacetamide (335 mg, 3.92 mmol, 1.1 eq), ethanol (7.24 mL, 0.50 M), and a catalytic amount of piperidine (1 mol%) was added in that order. After 18 hours, the precipitate was

filtered, washed, then dried under vacuum to yield **5j** (482.5 mg, 2.36 mmol, 65.3%) as a tan solid. The crude product was used without further purification. ^{1}H NMR (499 MHz, DMSO-d_6) δ 9.63 (d, *J* = 3.9 Hz, 2H), 8.68 (d, *J* = 1.7 Hz, 1H), 8.31 (d, *J* = 1.6 Hz, 1H), 7.74 (d, *J* = 4.4 Hz, 1H), 7.07 – 7.01 (m, 2H), 6.95 (dd, *J* = 8.9, 2.8 Hz, 1H), 6.88 – 6.78 (m, 0H).

2-imino-2H-chromene-3-carboxamide (5k)

Following procedure B: To a vial was added 2-hydroxybenzaldehyde (200 mg, 1.64 mmol, 1 eq), 2-cyanoacetamide (151 mg, 1.80 mmol, 1.1 eq), ethanol (3.28 mL, 0.50 M), and a catalytic amount of piperidine (1 mol%) was added in that order. After 18 hours, the precipitate was filtered, washed, then dried under vacuum to yield **5k** (124.3 mg, 660.5 µmol, 40.3%) as a white solid. The crude product was used without purification or characterization.

2-imino-7-methoxy-2H-chromene-3-carboxamide (5l)

Following procedure B: To a vial was added 2-hydroxy-4-methoxybenzaldehyde (200 mg, 1.31 mmol, 1 eq), 2-cyanoacetamide (122 mg, 1.45 mmol, 1.1 eq), ethanol (2.63 mL, 0.50 M), and a catalytic amount of piperidine (1 mol%) was added in that order. After 18 hours, the precipitate was filtered, washed, then dried under vacuum to yield **5l** (131.5 mg, 602.6 µmol, 45.8%) as a light tan solid.The crude product was used without purification or characterization.

7-fluoro-2-imino-2H-chromene-3-carboxamide (5m)

Following procedure B: To a vial was added 4-fluoro-2-hydroxybenzaldehyde (200 mg, 1.43 mmol, 1 eq), 2-cyanoacetamide (132 mg, 1.57 mmol, 1.1 eq), ethanol (2.85 mL, 0.50 M), and a catalytic amount of piperidine (1 mol%) was added in that order. After 18 hours, the precipitate was filtered, washed, then dried under vacuum to yield **5m** (234.4 mg, 1.137 mmol, 79.6%) as a yellow solid. The crude product was used without purification or characterization.

7-chloro-2-imino-2H-chromene-3-carboxamide (5n)

Following procedure B: To a vial was added 4-chloro-2-hydroxybenzaldehyde (200 mg, 1.28 mmol, 1 eq), 2-cyanoacetamide (118 mg, 1.41 mmol, 1.1 eq), ethanol (2.55 mL, 0.50 M), and a catalytic amount of piperidine (1 mol%) was added in that order. After 18 hours, the precipitate was filtered, washed, then dried under vacuum to yield **5n** (166.0 mg, 746 mmol, 58.4%) as a light tan solid. The crude product was used without purification or characterization.

7-bromo-2-imino-2H-chromene-3-carboxamide (5o)

Following procedure B: To a vial was added 4-bromo-2-hydroxybenzaldehyde (200 mg, 0.995 mmol, 1 eq), 2-cyanoacetamide (92.0 mg, 1.09 mmol, 1.1 eq), ethanol (1.99 mL, 0.50 M), and a catalytic amount of piperidine (1 mol%) was added in that order. After 18 hours, the precipitate was filtered, washed, then dried under vacuum to yield **5o** (190.6 mg, 713.6 µmol, 71.7%) as a white solid. The crude product was used without purification or characterization.

2-imino-7-methyl-2H-chromene-3-carboxamide (5p)

Following procedure B: To a vial was added 2-hydroxy-4-methylbenzaldehyde (200 mg, 1.47 mmol, 1 eq), 2-cyanoacetamide (136 mg, 1.62 mmol, 1.1 eq), ethanol (2.94 mL, 0.50 M), and a catalytic amount of piperidine (1 mol%) was added in that order. After 18 hours, the precipitate was filtered, washed, then dried under vacuum to yield **5p** (201.5 mg, 996.5 µmol, 67.8%) as an orange solid. The crude product was used without purification or characterization.

7-(tert-butyl)-2-imino-2H-chromene-3-carboxamide (5q)

Following procedure B: To a vial was added 4-(tert-butyl)-2-hydroxybenzaldehyde (200 mg, 1.12 mmol, 1 eq), 2-cyanoacetamide (104 mg, 1.23 mmol, 1.1 eq), ethanol (2.24 mL, 0.50 M), and a catalytic amount of piperidine (1 mol%) was added in that order. After 18 hours, the precipitate was filtered, washed, then dried under vacuum to yield **5q** (68.9 mg, 282 µmol, 25.1%) as a white solid. The crude product was used without purification or characterization.

7-cyano-2-imino-2H-chromene-3-carboxamide (5r)

Following procedure B: To a vial was added 4-formyl-3-hydroxybenzonitrile (50 mg, 0.34 mmol, 1 eq), 2-cyanoacetamide (31 mg, 0.37 mmol, 1.1 eq), ethanol (0.68 mL, 0.50 M), and a catalytic amount of piperidine (1 mol%) was added in that order. After 18 hours, the precipitate was filtered, washed, then dried under vacuum to yield **5r** (35 mg, 0.16 mmol, 48%) as a light tan solid. The crude product was used without purification or characterization.

2-imino-2H-pyrano[2,3-c]pyridine-3-carboxamide (5s)

Following procedure B: To a vial was added 3-hydroxyisonicotinaldehyde (100 mg, 812 µmol, 1 eq), 2-cyanoacetamide (75.1 mg, 894 µmol, 1.1 eq), ethanol (1.62 mL, 0.50 M), and a catalytic amount of piperidine (1 mol%) was added in that order. After 18 hours, the precipitate was filtered, washed, then dried under vacuum to yield **5s** (84 mg, 44 µmol, 55%) as a tan solid. The crude product was used without further purification. ^{1}H NMR (499 MHz, DMSO-d_6) δ 10.98 (s, 1H), 8.36 (d, J = 6.8 Hz, 1H), 8.29 (s, 1H), 8.17 (d, J = 5.1 Hz, 1H), 8.00 (s, 1H), 7.83 (s, 1H), 7.72 (dd, J = 22.1, 5.0 Hz, 1H).

7-butoxy-2-imino-2H-chromene-3-carboxamide (5t)

Following procedure B: To a vial was added 4-butoxy-2-hydroxybenzaldehyde (72 mg, 0.37 mmol, 1 eq), 2-cyanoacetamide (34 mg, 0.41 mmol, 1.1 eq), ethanol (0.74 mL, 0.50 M), and a catalytic amount of piperidine (1 mol%) was added in that order. After 18 hours, the precipitate was filtered, washed, then dried under vacuum to yield **5t** (41 mg, 0.16 mmol, 42%) as a tan solid. The crude product was used without purification or characterization.

(7-hydroxy-2-imino-2H-chromen-3-yl)(morpholino)methanone (5u)

To a vail containing a stir bar was added morpholine (116 mg, 1.33 mmol, 3 eq) and ethyl 2-cyanoacetate (50.0 mg, 442 µmol, 1 eq). The reaction was stirred for 24 hours. After that time, 2,4-dihydoxybenzaldehyde (54.9 mg, 398 µmol, 1 eq) in ethanol (884 µL, 0.50 M) was added to

the same vial. After an additional 18 hours, the precipitate was filtered, washed, then dried under vacuum to yield **5u** (71.0 mg, 259 mmol, 58.6%) as a tan solid.

3.11.3.3 Chromenones Analogs for Biological Evaluation (7-68)

(Z)-7-hydroxy-2-(p-tolylimino)-2H-chromene-3-carboxamide (GNF-9228)

Following Procedure C: To a flask was added p-toluidine (1.15 g, 10.8 mmol, 1.1 eq), **5a** (2.00 g, 9.79 mmol, 1 eq), and acetic acid (78.4 mL, 0.125 M). Reaction was let stir for 18 hrs at RT. Following the wash steps, 2.106 g (7.156 mmol, 73.1% yield) of **GNF-9228** was isolated as a yellow solid. Crude material was used without further purification. ^{1}H NMR (499 MHz, DMSO-d_6) δ 10.65 (s, 1H), 9.34 (d, J = 4.3 Hz, 1H), 8.42 (s, 1H), 7.75 (s, 1H), 7.60 (d, J = 8.1 Hz, 1H), 7.16 (q, J = 8.2 Hz, 4H), 6.71 (d, J = 8.5 Hz, 1H), 6.45 (s, 1H), 2.31 (s, 3H).

(Z)-2-((2-fluorophenyl)imino)-7-hydroxy-2H-chromene-3-carboxamide (7)

Following Procedure D: The corresponding aniline (31.2 mg) was solublized in methanol (265 µL) to form a 1.25 M solution. 100 µL of aniline stock solution was added to 900 µL of a 0.125 M solution of core **5a** and shaken for 18 hrs. General workup yielded 9.4 mg (25.6%) of **7** as a yellow solid. **UPLC/MS** (ESI) 299.08 $[M+H]^+$;RT: 2.777 min, Purity 73.16%.

(Z)-2-((3-fluorophenyl)imino)-7-hydroxy-2H-chromene-3-carboxamide (8)

Following Procedure D: The corresponding aniline (31.2 mg) was solublized in methanol (265 µL) to form a 1.25 M solution. 100 µL of aniline stock solution was added to 900 µL of a 0.125 M solution of core **5a** and shaken for 18 hrs. General workup yielded 31.4 mg (84.6%) of **8** as a yellow solid. **UPLC/MS** (ESI) 299.08 $[M+H]^+$;RT: 2.818 min, Purity 54.40%..

(Z)-2-((2,4-difluorophenyl)imino)-7-hydroxy-2H-chromene-3-carboxamide (9)

Following Procedure D: The corresponding aniline (25.0 mg) was solublized in methanol (202 µL) to form a 1.25 M solution. 100 µL of aniline stock solution was added to 900 µL of a 0.125 M solution of core **5a** and shaken for 18 hrs. General workup yielded 14.1 mg (37.1%) of **9** as a yellow solid. **UPLC/MS** (ESI) 317.07 $[M+H]^+$;RT: 2.829 min, Purity 70.4%

(Z)-2-((2,5-difluorophenyl)imino)-7-hydroxy-2H-chromene-3-carboxamide (10)

Following Procedure D: The corresponding aniline (40.6 mg) was solublized in methanol (332 µL) to form a 1.25 M solution. 100 µL of aniline stock solution was added to 900 µL of a 0.125 M solution of core **5a** and shaken for 18 hrs. General workup yielded 17.7 mg (45.6%) of **10** as a yellow solid. **UPLC/MS** (ESI) 317.07 $[M+H]^+$;RT: 2.827 min, Purity 85.0%.

(Z)-2-((2,6-difluorophenyl)imino)-7-hydroxy-2H-chromene-3-carboxamide (11)

Following Procedure D: The corresponding aniline (26.0 mg) was solublized in methanol (198 µL) to form a 1.25 M solution. 100 µL of aniline stock solution was added to 900 µL of a 0.125 M solution of core **5a** and shaken for 18 hrs. General workup yielded 7.2 mg (18.5%) of **11** as a yellow solid. **UPLC/MS** (ESI) 317.07 $[M+H]^+$;RT: 2.666 min, Purity 55.2%

(Z)-2-((2,6-difluoro-4-methoxyphenyl)imino)-7-hydroxy-2H-chromene-3-carboxamide (12)

Following Procedure D: The corresponding aniline (33.0 mg) was solublized in methanol (170 µL) to form a 1.25 M solution. 100 µL of aniline stock solution was added to 900 µL of a 0.125 M solution of core **5a** and shaken for 18 hrs. General workup yielded 11.9 mg (28.0%) of **12** as a yellow solid. **UPLC/MS** (ESI) 347.08 $[M+H]^+$;RT: 2.654 min, Purity 39.9%

(Z)-2-((4-cyano-2-fluorophenyl)imino)-2H-chromene-3-carboxamide (13)

Following Procedure C: To a flask was added 4-amino-3-flurobenzonitrile (133 mg, 979 µmol, 1 eq), **5a** (200 mg, 979 µmol, 1.05 eq), and acetic acid (7.84 mL, 0.125 M). Reaction was let stir for 18 hrs at RT. Following the wash steps, the crude product was purified via column chromatography (0-10% Methanol:DCM) to yield **13** (149.2 mg, 461.5 µmol, 47.1%) as a yellow solid. ^{1}H NMR (499 MHz, DMSO-d_6) δ 10.69 (s, 2H), 9.50 (s, 0H), 8.60 (s, 1H), 8.36 (s, 1H), 8.29 – 8.25 (m, 1H), 8.00 (d, J = 8.8 Hz, 1H), 7.58 (s, 1H), 7.50 (s, 2H), 6.64 (dd, J = 8.4, 2.3 Hz, 1H), 6.51 (d, J = 2.4 Hz, 1H), 6.41 – 6.32 (m, 2H).

(Z)-2-((4-ethoxyphenyl)imino)-7-hydroxy-2H-chromene-3-carboxamide (14)

Following Procedure D: The corresponding aniline (32.0 mg) was solublized in methanol (204 µL) to form a 1.25 M solution. 100 µL of aniline stock solution was added to 900 µL of a 0.125 M solution of core **5a** and shaken for 18 hrs. General workup yielded 2.3 mg (5.8%) of **14** as a yellow solid. **UPLC/MS** (ESI) 325.12 $[M+H]^+$;RT: 2.658 min, Purity 80.6%

(Z)-7-hydroxy-2-((4-(trifluoromethoxy)phenyl)imino)-2H-chromene-3-carboxamide (15)

Following Procedure C: To a flask was added 4-(trifluoromethoxy)aniline (9.54 mg, 539 µmol, 1.1 eq), **5a** (100 mg, 490 mmol, 1 eq), and acetic acid (3.92 mL, 0.125 M). Reaction was let stir for 18 hrs at RT. Following the wash steps, **15** (107 mg, 294 µmol, 60.0% yield) was isolated as a yellow solid. Crude material was used without further purification. ^{1}H NMR (499 MHz, DMSO-d_6) δ 10.67 (s, 1H), 9.14 (d, J = 4.0 Hz, 1H), 8.46 (d, J = 0.8 Hz, 1H), 7.77 (d, J = 4.0 Hz, 1H), 7.62 (d, J = 8.5 Hz, 1H), 7.34 (s, 4H), 6.72 (dd, J = 8.5, 2.2 Hz, 1H), 6.46 (dd, J = 2.3, 0.8 Hz, 1H).

(Z)-2-((4-(tert-butyl)phenyl)imino)-7-hydroxy-2H-chromene-3-carboxamide (16)

Following Procedure C: To a flask was added 4-(tert-butyl)aniline (37 mg, 0.24 mmol, 1 eq), **5a** (50 mg, 0.24 mmol, 1 eq), and acetic acid (2.0 mL, 0.125 M). Reaction was let stir for 18 hrs at RT. Following the wash steps, **16** (84.5 mg, 0.251 mmol, 100% yield) was isolated as a yellow solid. Crude material was used without further purification. 1H NMR (499 MHz, dmso) δ 9.37

(d, J = 4.4 Hz, 1H), 8.39 (s, 1H), 7.69 (d, J = 4.4 Hz, 1H), 7.53 (d, J = 8.5 Hz, 1H), 7.35 (d, J = 8.2 Hz, 2H), 7.16 (d, J = 8.2 Hz, 2H), 6.64 (dd, J = 8.5, 2.2 Hz, 1H), 6.39 (d, J = 2.2 Hz, 1H), 1.28 (s, 9H).

(Z)-2-((4-cyanophenyl)imino)-7-hydroxy-2H-chromene-3-carboxamide (17)

Following Procedure C: To a flask was added 4-aminobenzonitrile (629 mg, 5.414 mmol, 1.1 eq), **5a** (1.00 g, 4.92 mmol, 1 eq), and acetic acid (24.6 mL, 0.200 M). Reaction was let stir for 1 week at RT. Following the wash steps, 1.148 g (3.760 mmol, 76.39% yield) of **17** was isolated as a yellow solid. Crude material was used without further purification. ^{1}H NMR (499 MHz, DMSO-d_6) δ 10.75 (s, 1H), 8.98 (d, *J* = 3.9 Hz, 1H), 8.52 (s, 1H), 7.80 (q, *J* = 2.3 Hz, 2H), 7.65 (d, *J* = 8.5 Hz, 1H), 7.40 – 7.35 (m, 2H), 6.75 (dd, *J* = 8.5, 2.3 Hz, 1H), 6.45 (d, *J* = 2.2 Hz, 1H)

(Z)-2-((3-cyanophenyl)imino)-7-hydroxy-2H-chromene-3-carboxamide (18)

Following Procedure D: The corresponding aniline (33.6 mg) was solublized in methanol (233 µL) to form a 1.25 M solution. 100 µL of aniline stock solution was added to 900 µL of a 0.125 M solution of core **5a** and shaken for 18 hrs. General workup yielded 18.7 mg (49.9%) of **18** as a yellow solid. **UPLC/MS** (ESI) 306.08 $[M+H]^+$;RT: 2.680 min, Purity 52.7%

(Z)-2-((4-cyanophenyl)imino)-7-methoxy-2H-chromene-3-carboxamide (19)

Following Procedure C: To a flask was added 4-aminobenzonitrile (54.1 mg, 458 µmol, 1 eq), **5l** (100 mg, 458 µmol, 1 eq), and acetic acid (3.67 mL, 0.125 M). Reaction was let stir for 18 hrs at RT. Following the wash steps, **19** (52 mg, 0.16 mmol, 36% yield) was isolated as a yellow solid. Crude material was used without further purification. 1H NMR (499 MHz, dmso) δ 8.55 (s, 1H), 7.84 (s, 2H), 7.75 (d, J = 8.6 Hz, 1H), 7.41 – 7.36 (m, 2H), 6.91 (dd, J = 8.6, 2.4 Hz, 1H), 6.72 (d, J = 2.3 Hz, 1H), 3.82 (s, 3H).

(Z)-2-((4-cyanophenyl)imino)-2H-chromene-3-carboxamide (20)

Following Procedure C: To a flask was added 4-aminobenzonitrile (62.8 mg, 531 µmol, 1 eq), **5k** (100 mg, 531 µmol, 1 eq), and acetic acid (4.25 mL, 0.125 M). Reaction was let stir for 18 hrs at RT. Following the wash steps, **20** (66 mg, 0.23 mmol, 43% yield) was isolated as a light yellow solid**.** Crude material was used without further purification. NMR (499 MHz, cdcl3) δ 8.67 (s, 1H), 7.71 – 7.67 (m, 2H), 7.57 (dd, J = 7.7, 1.6 Hz, 1H), 7.52 (ddd, J = 8.6, 7.5, 1.6 Hz, 1H), 7.29 (dd, J = 7.6, 1.1 Hz, 1H), 7.25 (s, 1H), 7.08 (d, J = 8.3 Hz, 1H), 5.94 (s, 1H).

(Z)-2-((4-cyanophenyl)imino)-7-methyl-2H-chromene-3-carboxamide (21)

Following Procedure C: To a flask was added 4-aminobenzonitrile (58.4 mg, 495 µmol, 1 eq), **5p** (100 mg, 495 µmol, 1 eq), and acetic acid (3.96 mL, 0.125 M). Reaction was let stir for 18 hrs at RT. Following the wash steps, **21** (37 mg, 0.12 mmol, 25% yield) was isolated as a yellow solid. Crude material was used without further purification. 1H NMR (499 MHz, dmso) δ 8.95 (d, J =

3.8 Hz, 1H), 8.53 (s, 1H), 7.89 (d, J = 3.6 Hz, 1H), 7.82 (d, J = 8.1 Hz, 2H), 7.69 (d, J = 7.8 Hz, 1H), 7.37 (d, J = 8.1 Hz, 2H), 7.14 (d, J = 7.9 Hz, 1H), 6.99 (s, 1H), 2.34 (s, 3H).

(Z)-7-(tert-butyl)-2-((4-cyanophenyl)imino)-2H-chromene-3-carboxamide (22)

Following Procedure C: To a flask was added 4-aminobenzonitrile (29 mg, 0.25 mmol, 1 eq), **5q** (60 mg, 0.25 mmol, 1 eq), and acetic acid (2.0 mL, 0.125 M). Reaction was let stir for 18 hrs at RT. Following the wash steps, **22** (29 mg, 84 µmol, 34% yield) was isolated as a bright yellow solid. Crude material was used without further purification.1H NMR (499 MHz, cdcl3) δ 9.66 (s, 1H), 8.64 (s, 1H), 7.75 – 7.64 (m, 2H), 7.49 (d, J = 8.2 Hz, 1H), 7.31 (dd, J = 8.2, 1H), 7.06 – 6.95 (m, 1H), 5.84 (s, 1H), 1.32 (s, 9H).

(Z)-2-((4-cyanophenyl)imino)-8-hydroxy-2H-chromene-3-carboxamide (23)

Following Procedure C: To a flask was added 4-aminobenzonitrile (63.6 mg, 539 µmol, 1.1 eq), **5i** (100.0 mg, 490 µmol, 1 eq), and acetic acid (3.92 mL, 0.125 M). Reaction was let stir for 18 hrs at RT. Following the wash steps, **23 (**107 mg, 350 µmol, 71.6% yield) was isolated as a yellow solid. Crude material was used without further purification. ^{1}H NMR (499 MHz, DMSO-d_6) δ 10.11 (s, 1H), 9.10 (d, *J* = 3.9 Hz, 1H), 8.52 (s, 1H), 7.92 (d, *J* = 3.9 Hz, 1H), 7.85 – 7.79 (m, 2H), 7.56 – 7.50 (m, 2H), 7.23 (dd, *J* = 7.3, 1.9 Hz, 1H), 7.12 (t, *J* = 7.7 Hz, 1H), 7.09 (dd, *J* = 8.0, 1.9 Hz, 1H).

(Z)-2-((4-cyanophenyl)imino)-6-hydroxy-2H-chromene-3-carboxamide (24)

Following Procedure C: To a flask was added 4-aminobenzonitrile (63.6 mg, 539 µmol, 1.1 eq), **5j** (100.0 mg, 490 µmol, 1 eq), and acetic acid (3.92 mL, 0.125 M). Reaction was let stir for 18 hrs at RT. Following the wash steps, **24 (**75.0 mg, 246 µmol, 50.2% yield) was isolated as a yellow solid. Crude material was used without further purification. ^{1}H NMR (499 MHz, DMSO-d_6) δ 9.79 (s, 1H), 9.02 (d, *J* = 3.8 Hz, 1H), 8.49 (s, 1H), 7.91 (d, *J* = 3.7 Hz, 1H), 7.85 – 7.78 (m, 2H), 7.40 – 7.34 (m, 2H), 7.14 (d, *J* = 2.7 Hz, 1H), 7.05 – 6.94 (m, 2H), 3.29 (s, 1H).

(Z)-2-((4-cyanophenyl)imino)-7-fluoro-2H-chromene-3-carboxamide (25)

Following Procedure C: To a flask was added 4-aminobenzonitrile (57.3 mg, 485 µmol, 1 eq), **5m** (100 mg, 485 µmol, 1 eq), and acetic acid (3.88 mL, 0.125 M). Reaction was let stir for 18 hrs at RT. Following the wash steps, **25** (34.2 mg, 0.111 mmol, 22.9% yield) was isolated as a yellow solid. Crude material was used without further purification. 1H NMR (499 MHz, dmso) δ 8.90 (d, 1H), 8.58 (d, 1H), 7.91 – 7.88 (m, 1H), 7.85 – 7.79 (m, 2H), 7.48 – 7.37 (m, 2H), 7.22 (td, J = 8.7, 2.5 Hz, 1H), 7.15 (dd, J = 9.6, 2.4 Hz, 1H).

(Z)-7-chloro-2-((4-cyanophenyl)imino)-2H-chromene-3-carboxamide (26)

Following Procedure C: To a flask was added 4-aminobenzonitrile (53.1 mg, 449 µmol, 1 eq), **5n** (100 mg, 449 µmol, 1 eq), and acetic acid (3.59 mL, 0.125 M). Reaction was let stir for 18 hrs at RT. Following the wash steps, **26** (87.6 mg, 0.271 mmol, 60.2% yield) was isolated as a yellow

solid. Crude material was used without further purification.1H NMR (499 MHz, dmso) δ 8.92 – 8.88 (m, 1H), 8.56 (d, J = 0.7 Hz, 1H), 7.95 (d, J = 3.6 Hz, 1H), 7.86 (s, 1H), 7.84 – 7.80 (m, 2H), 7.43 – 7.40 (m, 2H), 7.39 (d, J = 2.0 Hz, 1H), 7.34 (dd, J = 1.9, 0.8 Hz, 1H).

(Z)-7-bromo-2-((4-cyanophenyl)imino)-2H-chromene-3-carboxamide (27)

Following Procedure C: To a flask was added 4-aminobenzonitrile (66.4 mg, 562 µmol, 1 eq), **5o** (150 mg, 562 µmol, 1 eq), and acetic acid (4.49 mL, 0.125 M). Reaction was let stir for 18 hrs at RT. Following the wash steps, **27** (30 mg, 81 µmol, 15% yield) was isolated as a yellow solid. Crude material was used without further purification. 1H NMR (499 MHz, dmso) δ 8.94 – 8.86 (m, 1H), 8.54 (s, 1H), 7.98 – 7.90 (m, 1H), 7.82 (d, J = 8.3 Hz, 2H), 7.76 (d, J = 8.2 Hz, 1H), 7.51 (dd, J = 8.3, 1.8 Hz, 1H), 7.45 (d, J = 1.8 Hz, 1H), 7.41 (d, J = 8.3 Hz, 2H).

(Z)-2-((2,3-difluorophenyl)imino)-7-hydroxy-2H-chromene-3-carboxamide (28)

Following Procedure D: The corresponding aniline (25.0 mg) was solublized in methanol (202 µL) to form a 1.25 M solution. 100 µL of aniline stock solution was added to 900 µL of a 0.125 M solution of core **5a** and shaken for 18 hrs. General workup yielded 12.7 mg (32.7%) of **28** as a yellow solid. **UPLC/MS** (ESI) 341.11 $[M+H]^+$;RT: 2.613 min, Purity 86.83%

(Z)-7-hydroxy-2-((2,4,6-trifluorophenyl)imino)-2H-chromene-3-carboxamide (29)

Following Procedure D: The corresponding aniline (55.4 mg) was solublized in methanol (309 µL) to form a 1.25 M solution. 100 µL of aniline stock solution was added to 900 µL of a 0.125 M solution of core **5a** and shaken for 18 hrs. General workup yielded 8.5 mg (20.7%) of **29** as a yellow solid. **UPLC/MS** (ESI) 335.06 $[M+H]^+$;RT: 2.850 min, Purity 65.2%

(Z)-7-hydroxy-2-((3,4,5-trifluorophenyl)imino)-2H-chromene-3-carboxamide (30)

Following Procedure D: The corresponding aniline (51.9 mg) was solublized in methanol (290 µL) to form a 1.25 M solution. 100 µL of aniline stock solution was added to 900 µL of a 0.125 M solution of core **5a** and shaken for 18 hrs. General workup yielded 12.1 mg (29.5%) of **30** as a yellow solid. **UPLC/MS** (ESI) 335.06 $[M+H]^+$;RT: 2.920 min, Purity 50.8%

(Z)-2-((3,5-difluorophenyl)imino)-7-hydroxy-2H-chromene-3-carboxamide (31)

Following Procedure D: The corresponding aniline (37.4 mg) was solublized in methanol (238 µL) to form a 1.25 M solution. 100 µL of aniline stock solution was added to 900 µL of a 0.125 M solution of core **5a** and shaken for 18 hrs. General workup yielded 20.9 mg (53.8%) of **31** as a yellow solid. **UPLC/MS** (ESI) 317.07 $[M+H]^+$;RT: 2.832 min, Purity 51.3%

(Z)-2-((2-chlorophenyl)imino)-7-hydroxy-2H-chromene-3-carboxamide (32)

Following Procedure D: The corresponding aniline (37.8 mg) was solublized in methanol (294 µL) to form a 1.25 M solution. 100 µL of aniline stock solution was added to 900 µL of a 0.125 M solution of core **5a** and shaken for 18 hrs. General workup yielded 10.7 mg (27.7%) of **32** as a yellow solid. **UPLC/MS** (ESI) 315.05 $[M+H]^+$;RT: 2.857 min, Purity 60.63%.

(Z)-2-((3-chlorophenyl)imino)-7-hydroxy-2H-chromene-3-carboxamide (33)

Following Procedure D: The corresponding aniline (26.0 mg) was solublized in methanol (204 µL) to form a 1.25 M solution. 100 µL of aniline stock solution was added to 900 µL of a 0.125 M solution of core **5a** and shaken for 18 hrs. General workup yielded 19.6 mg (50.7%) of **33** as a yellow solid. **UPLC/MS** (ESI) 315.05 $[M+H]^+$;RT: 2.933 min, Purity 55.0%

(Z)-2-((4-chlorophenyl)imino)-7-hydroxy-2H-chromene-3-carboxamide (34)

Following Procedure D: The corresponding aniline (28.02 mg) was solublized in methanol (180 µL) to form a 1.25 M solution. 100 µL of aniline stock solution was added to 900 µL of a 0.125 M solution of core **5a** and shaken for 18 hrs. General workup yielded 7.5 mg (19.4%) of **34** as a yellow solid. **UPLC/MS** (ESI) 315.05 $[M+H]^+$;RT: 2.925 min, Purity 80.5%

(Z)-2-((2,3-dichlorophenyl)imino)-7-hydroxy-2H-chromene-3-carboxamide (35)

Following Procedure D: The corresponding aniline (70 mg) was solublized in methanol (354 µL) to form a 1.25 M solution. 100 µL of aniline stock solution was added to 900 µL of a 0.125 M solution of core **5a** and shaken for 18 hrs. General workup yielded 18.2 mg (42.5%) of **35** as a yellow solid. **UPLC/MS** (ESI) 349.02 $[M+H]^+$;RT: 2.834 min, Purity 49.6%

(Z)-2-((2,5-dichlorophenyl)imino)-7-hydroxy-2H-chromene-3-carboxamide (36)

Following Procedure D: The corresponding aniline (62.9 mg) was solublized in methanol (318 µL) to form a 1.25 M solution. 100 µL of aniline stock solution was added to 900 µL of a 0.125 M solution of core **5a** and shaken for 18 hrs. General workup yielded 15.3 mg (35.7%) of **36** as a yellow solid. **UPLC/MS** (ESI) 349.01 $[M+H]^+$;RT: 2.985 min, Purity 68.26%

(Z)-2-((3,4-dichlorophenyl)imino)-7-hydroxy-2H-chromene-3-carboxamide (37)
Following Procedure D: The corresponding aniline (65.0 mg) was solublized in methanol (328 µL) to form a 1.25 M solution. 100 µL of aniline stock solution was added to 900 µL of a 0.125 M solution of core **5a** and shaken for 18 hrs. General workup yielded 29 mg (67.7%) of **37** as a yellow solid. **UPLC/MS** (ESI) 349.01 $[M+H]^+$;RT: 3.002 min, Purity 61.5%

(Z)-2-((4-chloro-2-methylphenyl)imino)-7-hydroxy-2H-chromene-3-carboxamide (38)

Following Procedure D: The corresponding aniline (80.0 mg) was solublized in methanol (464 µL) to form a 1.25 M solution. 100 µL of aniline stock solution was added to 900 µL of a 0.125 M solution of core **5a** and shaken for 18 hrs. General workup yielded 19.8 mg (49.1%) of **38** as a yellow solid. **UPLC/MS** (ESI) 329.07 $[M+H]^+$;RT: 2.854 min, Purity 41.2%

(Z)-2-((4-chloro-2-methoxyphenyl)imino)-7-hydroxy-2H-chromene-3-carboxamide (39)

Following Procedure D: The corresponding aniline (44.6 mg) was solublized in methanol (232 µL) to form a 1.25 M solution. 100 µL of aniline stock solution was added to 900 µL of a 0.125 M solution of core **5a** and shaken for 18 hrs. General workup yielded 2.1 mg (5.0%) of **39** as a yellow solid. **UPLC/MS** (ESI) 345.06 $[M+H]^+$;RT: 2.779 min, Purity 39.6%

(Z)-2-((4-chloro-3-hydroxyphenyl)imino)-7-hydroxy-2H-chromene-3-carboxamide (40)

Following Procedure D: The corresponding aniline (38.0 mg) was solublized in methanol (198 µL) to form a 1.25 M solution. 100 µL of aniline stock solution was added to 900 µL of a 0.125 M solution of core **5a** and shaken for 18 hrs. General workup yielded 14 mg (33.1%) of **40** as a yellow solid. **UPLC/MS** (ESI) 345.06 $[M+H]^+$;RT: 2.891 min, Purity 66.2%

(Z)-2-((4-chloro-3-methoxyphenyl)imino)-7-hydroxy-2H-chromene-3-carboxamide (41)

Following Procedure D: The corresponding aniline (46.9 mg) was solublized in methanol (244 µL) to form a 1.25 M solution. 100 µL of aniline stock solution was added to 900 µL of a 0.125 M solution of core **5a** and shaken for 18 hrs. General workup yielded 23.0 mg (54.4%) of **41** as a yellow solid. **UPLC/MS** (ESI) 345.06 $[M+H]^+$;RT: 2.866 min, Purity 77.4%

(Z)-2-((3-chloro-5-fluorophenyl)imino)-7-hydroxy-2H-chromene-3-carboxamide (42)

Following Procedure D: The corresponding aniline (42.9 mg) was solublized in methanol (242 µL) to form a 1.25 M solution. 100 µL of aniline stock solution was added to 900 µL of a 0.125 M solution of core **5a** and shaken for 18 hrs. General workup yielded 21.5 mg (52.6%) of **42** as a yellow solid. **UPLC/MS** (ESI) 333.04 $[M+H]^+$;RT: 2.970 min, Purity 74.8%

(Z)-2-((3-chloro-5-(trifluoromethyl)phenyl)imino)-7-hydroxy-2H-chromene-3-carboxamide (43)

Following Procedure D: The corresponding aniline (105.9 mg) was solublized in methanol (444 µL) to form a 1.25 M solution. 100 µL of aniline stock solution was added to 900 µL of a 0.125 M solution of core **5a** and shaken for 18 hrs. General workup yielded 14.2 mg (30.3%) of **43** as a yellow solid. **UPLC/MS** (ESI) 383.04 $[M+H]^+$;RT: 3.074 min, Purity 62.4%

(Z)-2-((3-chloro-5-methoxyphenyl)imino)-7-hydroxy-2H-chromene-3-carboxamide (44)

Following Procedure D: The corresponding aniline (41.3 mg) was solublized in methanol (214 µL) to form a 1.25 M solution. 100 µL of aniline stock solution was added to 900 µL of a 0.125 M solution of core **5a** and shaken for 18 hrs. General workup yielded 23.9 mg (56.5%) of **44** as a yellow solid. **UPLC/MS** (ESI) 345.07 $[M+H]^+$;RT: 2.906 min, Purity 69.4%

(Z)-2-((3-chloro-5-methylphenyl)imino)-7-hydroxy-2H-chromene-3-carboxamide (45)

Following Procedure D: The corresponding aniline (37.4 mg) was solublized in methanol (216 µL) to form a 1.25 M solution. 100 µL of aniline stock solution was added to 900 µL of a 0.125 M solution of core **5a** and shaken for 18 hrs. General workup yielded 20.0 mg (49.6%) of **45** as a yellow solid. **UPLC/MS** (ESI) 329.07 $[M+H]^+$;RT: 2.925 min, Purity 69.2%

(Z)-2-((3-chloro-5-cyanophenyl)imino)-7-hydroxy-2H-chromene-3-carboxamide (46)

Following Procedure D: The corresponding aniline (39.3 mg) was solublized in methanol (212 µL) to form a 1.25 M solution. 100 µL of aniline stock solution was added to 900 µL of a 0.125 M solution of core **5a** and shaken for 18 hrs. General workup yielded 10 mg (24%) of **46** as a yellow solid. **UPLC/MS** (ESI) 340.05 $[M+H]^+$;RT: 2.746 min, Purity 32.4%

(Z)-2-((2-chloro-5-methoxyphenyl)imino)-7-hydroxy-2H-chromene-3-carboxamide (47)

Following Procedure D: The corresponding aniline (31.0 mg) was solublized in methanol (204 µL) to form a 1.25 M solution. 100 µL of aniline stock solution was added to 900 µL of a 0.125 M solution of core **5a** and shaken for 18 hrs. General workup yielded 16.6 mg (39.2%) of **47** as a yellow solid. **UPLC/MS** (ESI) 345.06 $[M+H]^+$;RT: 2.771 min, Purity 36.8%

(Z)-2-((2-chloro-4-methylphenyl)imino)-7-hydroxy-2H-chromene-3-carboxamide (48)

Following Procedure D: The corresponding aniline (31 mg) was solublized in methanol (206 µL) to form a 1.25 M solution. 100 µL of aniline stock solution was added to 900 µL of a 0.125 M solution of core **5a** and shaken for 18 hrs. General workup yielded 11.2 mg (27.8%) of **48** as a yellow solid. **UPLC/MS** (ESI) 329.07 $[M+H]^+$;RT: 2.957 min, Purity 73.4%

(Z)-2-((4-bromo-2-chlorophenyl)imino)-7-hydroxy-2H-chromene-3-carboxamide (49)

Following Procedure D: The corresponding aniline (68.6 mg) was solublized in methanol (272 µL) to form a 1.25 M solution. 100 µL of aniline stock solution was added to 900 µL of a 0.125 M solution of core **5a** and shaken for 18 hrs. General workup yielded 26.6 mg (55.1%) of **49** as a yellow solid. **UPLC/MS** (ESI) 392.96 $[M+H]^+$;RT: 3.039 min, Purity 67.0%

(Z)-2-((4-bromophenyl)imino)-7-hydroxy-2H-chromene-3-carboxamide (50)

Following Procedure D: The corresponding aniline (117.23 mg) was solublized in methanol (559 µL) to form a 1.25 M solution. 100 µL of aniline stock solution was added to 900 µL of a 0.125 M solution of core **5a** and shaken for 18 hrs. General workup yielded 33.4 mg (75.8%) of **50** as a yellow solid. **UPLC/MS** (ESI) 359.00 $[M+H]^+$;RT: 2.925 min, Purity 51.9%

(Z)-2-((3,5-bis(trifluoromethyl)phenyl)imino)-7-hydroxy-2H-chromene-3-carboxamide (51)

Following Procedure D: The corresponding aniline (40.0 mg) was solublized in methanol (210 µL) to form a 1.25 M solution. 100 µL of aniline stock solution was added to 900 µL of a 0.125 M solution of core **5a** and shaken for 18 hrs. General workup yielded 8.8 mg (17.2%) of **51** as a yellow solid. **UPLC/MS** (ESI) 417.07 $[M+H]^+$;RT: 3.079 min, Purity 49.7%.

(Z)-2-((2,5-dimethylphenyl)imino)-7-hydroxy-2H-chromene-3-carboxamide (52)

Following Procedure D: The corresponding aniline (31.0 mg) was solublized in methanol (204 µL) to form a 1.25 M solution. 100 µL of aniline stock solution was added to 900 µL of a 0.125 M solution of core **5a** and shaken for 18 hrs. General workup yielded 4.6 mg (12.1%) of **52** as a yellow solid. **UPLC/MS** (ESI) 309.12 $[M+H]^+$;RT: 2.901 min, Purity 80.4%

(Z)-2-((3,4-dimethoxyphenyl)imino)-7-hydroxy-2H-chromene-3-carboxamide (53)

Following Procedure D: The corresponding aniline (43.2 mg) was solublized in methanol (231 µL) to form a 1.25 M solution. 100 µL of aniline stock solution was added to 900 µL of a 0.125 M solution of core **5a** and shaken for 18 hrs. General workup yielded 8.2 mg (19.6%) of **53** as a yellow solid. **UPLC/MS** (ESI) 341.11 $[M+H]^+$;RT: 2.613 min, Purity 31.8%

(Z)-2-((3-ethynylphenyl)imino)-7-hydroxy-2H-chromene-3-carboxamide (54)

Following Procedure D: The corresponding aniline (34.3 mg) was solublized in methanol (240 µL) to form a 1.25 M solution. 100 µL of aniline stock solution was added to 900 µL of a 0.125 M solution of core **5a** and shaken for 18 hrs. General workup yielded 19.3 mg (51.4%) of **54** as a yellow solid. **UPLC/MS** (ESI) 305.09 $[M+H]^+$;RT: 2.743 min, Purity 65.2%

(Z)-3-((3-carbamoyl-7-hydroxy-2H-chromen-2-ylidene)amino)-4-methylbenzoic acid (55)

Following Procedure D: The corresponding aniline (59.4 mg) was solublized in methanol (322 µL) to form a 1.25 M solution. 100 µL of aniline stock solution was added to 900 µL of a 0.125 M solution of core **5a** and shaken for 18 hrs. General workup yielded 18.4 mg (44.3%) of **55** as a yellow solid. **UPLC/MS** (ESI) 339.10 $[M+H]^+$;RT: 2.707 min, Purity 37.5%

(Z)-2-((3-carbamoylphenyl)imino)-7-hydroxy-2H-chromene-3-carboxamide (56)

Following Procedure D: The corresponding aniline (42.6 mg) was solublized in methanol (256 µL) to form a 1.25 M solution. 100 µL of aniline stock solution was added to 900 µL of a 0.125 M solution of core **5a** and shaken for 18 hrs. General workup yielded 12.6 mg (31.7%) of **56** as a yellow solid. **UPLC/MS** (ESI) 324.10 $[M+H]^+$;RT: 2.241 min, Purity 45.6%

(Z)-2-((4-acetamidophenyl)imino)-7-hydroxy-2H-chromene-3-carboxamide (57)

Following Procedure D: The corresponding aniline (51.7 mg) was solublized in methanol (282 µL) to form a 1.25 M solution. 100 µL of aniline stock solution was added to 900 µL of a 0.125 M solution of core **5a** and shaken for 18 hrs. General workup yielded 15.7 mg (37.9%) of **57** as a yellow solid. **UPLC/MS** (ESI) 338.11 $[M+H]^+$;RT: 2.206 min, Purity 43.3%

(Z)-7-hydroxy-2-((4-(methyl-d3)phenyl)imino)-2H-chromene-3-carboxamide (58)

Following Procedure C: To a flask was added 4-(methyl-d3)aniline (12.9 mg, 118 µmol, 1 eq), **5a** (25.2 mg, 123 µmol, 1.05 eq), and acetic acid (0.94 mL, 0.125 M). Reaction was let stir for 18 hrs at RT. Following the wash steps, 11.9 mg (40.0 mmol, 34.1% yield) of **58** was isolated as a yellow solid. Crude material was used without further purification.

(Z)-2-((3-cyano-4-methylphenyl)imino)-7-hydroxy-2H-chromene-3-carboxamide (59)

Following Procedure D: The corresponding aniline (44.0 mg) was solublized in methanol (272 µL) to form a 1.25 M solution. 100 µL of aniline stock solution was added to 900 µL of a 0.125 M solution of core **5a** and shaken for 18 hrs. General workup yielded 27.4 mg (56.5%) of **59** as a yellow solid. **UPLC/MS** (ESI) 320.10 $[M+H]^+$;RT: 2.756 min, Purity 58.0%

(Z)-2-((5-cyanopyridin-2-yl)imino)-7-hydroxy-2H-chromene-3-carboxamide (60)

Following Procedure C: To a flask was added 6-aminonicotinonitrile (64.2 mg, 539 µmol, 1.1 eq), **5a** (100.0 mg, 490 µmol, 1 eq), and acetic acid (3.92 mL, 0.125 M). Reaction was let stir for 18 hrs at RT. Following the wash steps, **60 (**128.8 mg, 420.5 µmol, 85.9% yield) was isolated as a yellow solid. Crude material was used without further purification. ^{1}H NMR (499 MHz, DMSO-d_6) δ 10.60 (s, 1H), 9.53 – 9.49 (m, 1H), 8.67 – 8.63 (m, 1H), 8.31 (s, 1H), 8.02 (d, *J* = 8.7 Hz, 0H), 7.62 (s, 1H), 7.55 (d, *J* = 8.5 Hz, 1H), 6.67 (dd, *J* = 8.5, 2.2 Hz, 1H), 6.54 (d, *J* = 2.2 Hz, 1H), 6.44 – 6.36 (m, 1H).

(Z)-2-((4-(hexyloxy)phenyl)imino)-7-hydroxy-2H-chromene-3-carboxamide (61)

Following Procedure C: To a flask was added 4-(hexyloxy)aniline (47 mg, 0.24 mmol, 1 eq), **5a** (50 mg, 0.24 mmol, 1 eq), and acetic acid (2.0 mL, 0.125 M). Reaction was let stir for 18 hrs at RT. Following the wash steps, **61** (64 mg, 0.17mmol, 69% yield) was isolated as an orange solid. Crude material was used without further purification. 1H NMR (499 MHz, dmso) δ 9.38 (d, J =

4.2 Hz, 1H), 8.37 (s, 1H), 7.73 (d, J = 4.3 Hz, 1H), 7.57 (d, J = 8.5 Hz, 1H), 7.29 – 7.18 (m, 2H), 6.96 – 6.86 (m, 2H), 6.70 (dd, J = 8.5, 2.2 Hz, 1H), 6.49 (d, J = 2.2 Hz, 1H), 3.95 (t, J = 6.5 Hz, 2H), 1.70 (p, J = 6.6 Hz, 2H), 1.41 (t, J = 7.6 Hz, 2H), 1.30 (p, J = 3.8 Hz, 4H), 0.91 – 0.81 (m, 3H).

(Z)-N-cyclohexyl-2-(cyclohexylimino)-2H-chromene-3-carboxamide (62)

Following procedure B: To a vial was added 2,4-dihydoxybenzaldehyde (100 mg, 724 µmol, 1 eq), cyclohexanamine (263.0 mg, 2.65 mmol, 3 eq), and ethanol (1.77 mL, 0.50 M) were added in that order. After 48 hours, the precipitate was filtered purified via column chromatography (10-100% EtOAc:Hex) to yield **62** (94.9 mg, 258.0 µmol, 29.1%) as a yellow solid. ^{1}H NMR (499 MHz, DMSO-d_6) δ 10.59 (d, *J* = 7.8 Hz, 1H), 8.22 (s, 1H), 7.53 (d, *J* = 8.4 Hz, 1H), 6.67 (dd, *J* = 8.4, 2.3 Hz, 2H), 6.58 (d, *J* = 2.2 Hz, 1H), 3.91 (tt, *J* = 8.0, 3.6 Hz, 2H), 3.79 (dt, *J* = 12.0, 6.0 Hz, 1H), 1.85 – 1.77 (m, 4H), 1.81 – 1.71 (m, 3H), 1.75 – 1.69 (m, 1H), 1.69 – 1.60 (m, 1H), 1.54 (d, *J* = 31.2 Hz, 1H), 1.48 – 1.21 (m, 8H).

(Z)-2-((4-cyanophenyl)imino)-2H-pyrano[2,3-c]pyridine-3-carboxamide (63)

Following Procedure C: To a flask was added 4-aminobenzonitrile (31.2 mg, 264 µmol, 1 eq), **5s** (50.0 mg, 264 µmol, 1 eq), and acetic acid (2.11 mL, 0.125 M). Reaction was let stir for 18 hours at RT. Following the wash steps, **63** (30.5 mg, 105 µmol, 29.8%) was isolated as a yellow solid. Crude material was used without further purification.^{1}H NMR (499 MHz, DMSO-d_6) δ 10.59 (s, 1H), 9.52 – 9.48 (m, 1H), 8.65 – 8.61 (m, 1H), 8.29 (s, 1H), 8.00 (d, *J* = 8.7 Hz, 0H), 7.60 (s,

1H), 7.54 (d, *J* = 8.5 Hz, 1H), 6.66 (dd, *J* = 8.5, 2.2 Hz, 1H), 6.53 (d, *J* = 2.2 Hz, 1H), 6.42 – 6.35 (m, 1H).

(Z)-2-((4-cyano-2-fluorophenyl)imino)-2H-pyrano[2,3-c]pyridine-3-carboxamide (64)

Following Procedure C: To a flask was added 4-amino-3-fluorobenzene (122 mg, 894 µmol, 1.1 eq), **5s** (154 mg, 812 µmol, 1 eq), and acetic acid (6.5 mL, 0.125 M). Reaction was let stir for 18 hrs at RT. Following the wash steps,the crude material purified via column chromatography (0-30% MeOH:DCM) to yield **64 (**4 mg, 10 µmol, 2% yield)as a yellow solid ^{1}H NMR (499 MHz, DMSO-d_6) δ 8.77 (s, 1H), 8.50 (d, *J* = 4.9 Hz, 1H), 8.10 – 8.05 (m, 1H), 7.94 (dd, *J* = 10.4, 1.8 Hz, 1H), 7.79 (d, *J* = 4.9 Hz, 1H), 7.72 (dd, *J* = 8.3, 1.8 Hz, 1H), 7.59 (t, *J* = 8.1 Hz, 1H), 3.27 (s, 7H).

(Z)-7-cyano-2-((4-cyanophenyl)imino)-2H-chromene-3-carboxamide (65)

Following Procedure C: To a flask was added 4-aminobenzonitrile (17 mg, 0.14 mmol, 1 eq), **5r** (30 mg, 0.14 mmol, 1 eq), and acetic acid (1.1 mL, 0.125 M). Reaction was let stir for 18 hrs at RT. Following the wash steps, **65** (28 mg, 89 µmol, 63% yield) was isolated as a bright yellow solid. Crude material was used without further purification.1H NMR (499 MHz, dmso) δ 8.83 (s, 1H), 8.54 (s, 1H), 8.01 – 7.93 (m, 2H), 7.82 (d, J = 7.8 Hz, 2H), 7.73 (d, J = 8.5 Hz, 2H), 7.41 (d, J = 8.1 Hz, 2H).

(Z)-7-cyano-2-(p-tolylimino)-2H-chromene-3-carboxamide (66)

Following Procedure C: To a flask was added p-toluidine (15 mg, 0.14 mmol, 1 eq), **5r** (30 mg, 0.14 mmol, 1 eq), and acetic acid (1.1 mL, 0.125 M). Reaction was let stir for 18 hrs at RT. Following the wash steps, **66** (37.7 mg, 0.124 mmol, 88% yield) was isolated as a bright yellow solid. Crude material was used without further purification. 1H NMR (400 MHz, dmso) δ 9.19 (s, 1H), 8.47 (s, 1H), 7.99 (s, 1H), 7.94 (d, J = 7.9 Hz, 1H), 7.77 – 7.63 (m, 2H), 7.23 (d, J = 8.2 Hz, 2H), 7.18 (d, J = 8.2 Hz, 2H), 2.31 (s, 3H).

(Z)-7-cyano-2-((4-(trifluoromethoxy)phenyl)imino)-2H-chromene-3-carboxamide (67)

Following Procedure C: To a flask was added 4-cyclopropyl aniline (33 mg, 0.24 mmol, 1 eq), **5r** (50 mg, 0.24 mmol, 1 eq), and acetic acid (2.0 mL, 0.125 M). Reaction was let stir for 18 hrs at RT. Following the wash steps, **67** (39 mg, 0.10 mmol, 74% yield) was isolated as a bright yellow solid. Crude material was used without further purification. 1H NMR (499 MHz, dmso) δ 9.05 – 8.98 (m, 1H), 8.52 (s, 1H), 8.03 – 7.92 (m, 2H), 7.76 (s, 1H), 7.72 (d, J = 7.9 Hz, 1H), 7.42 (d, J = 8.7 Hz, 2H), 7.35 (d, J = 8.6 Hz, 2H).

(Z)-7-butoxy-2-(p-tolylimino)-2H-chromene-3-carboxamide (68)

Following Procedure C: To a flask was added p-toluidine (17 mg, 0.16 mmol, 1 eq), **5t** (41 mg, 0.16 mmol, 1 eq), and acetic acid (1.3 mL, 0.125 M). Reaction was let stir for 18 hrs at RT. Following the wash steps, **68** (7.6 mg, 22 µmol, 14% yield) was isolated as a bright yellow solid.

Crude material was used without further purification. 1H NMR (499 MHz, cdcl3) δ 10.06 (s, 1H), 8.49 (s, 1H), 7.38 (d, J = 8.6 Hz, 1H), 7.20 (d, J = 8.0 Hz, 2H), 7.14 (d, J = 8.2 Hz, 2H), 6.75 (dd, J = 8.6, 2.4 Hz, 1H), 6.57 (d, J = 2.3 Hz, 1H), 5.80 (s, 1H), 3.97 (t, J = 6.5 Hz, 2H), 2.38 (s, 3H), 1.76 (p, J = 6.6 Hz, 2H), 1.54 (d, J = 1.5 Hz, 2H), 1.47 (dt, J = 14.8, 7.4 Hz, 2H), 0.97 (t, J = 7.4 Hz, 3H).

Chapter 4 Conclusions

This dissertation represents the bulk of the work we completed at the University of Michigan during the acquisition of my PhD. The first chapter was an in-depth summary of the recently developing field of beta-cell regeneration through the use of small molecules. The bulk of screening efforts to identify these compounds have happened in either luciferase-based assays or low-content fluorescence assays. Only this year was a method for high-throughput mass spectrometry-based insulin quantification published. Additionally, only one other group has published a high-content islet assay platform comparable to our own. Overall, almost all of the research to discover small molecules capable of initiating beta-cell proliferation has occurred in the last decade and a half, demonstrating just how cutting edge this field is.

Chapter 2 describes our development of a novel high-content imaging platform for pancreatic islets. The primary innovation of this platform was the use of two-pass imaging to vastly improve the efficiency of imaging. Furthermore, an analysis of cell height allowed us to further streamline the number and depth of imaging planes. The combination of these techniques led to a pseudo-3D imaging technique with vast improvements in imaging speed and analysis over true three-dimensional imaging while dramatically reducing the size on disk. After streamlining data acquisition, we could then start to analyze islet morphology on an unprecedented scale. We are able to parse whole islet size and shape morphometrics while also

maintaining the resolution to evaluate changes in cellular composition and organization within the same islets.

Chapter 3 describes the evaluation and exploration of the GNF-9228 scaffold as a potential small molecule modulator of beta-cell proliferation. During the course of this work, we were able to apply the new islet imaging technology to assess *in vivo* efficacy of our lead compound. Classically, evaluation of effects on pancreatic islets has been done through histologic slicing. Only glimpsing various planes within the three-dimensional structure of the pancreas leads to the loss of so much dimensional data. On top of that, the process is time consuming, technically challenging, and expensive. Ultimately, we were only able to observe an effect in some of the animals, but we found that encouraging enough to start an SAR campaign. The first forty something compounds were synthesized using a novel high-throughput method. Subsequent work led to the synthesis of an additional thirty compounds so we could effectively probe three different regions of the scaffold. While some of the compounds showed promise, overall, the results were largely mediocre.

These projects provided an amazing opportunity to work on cutting edge research for a disease that is globally known and endured. Through this experience, it became clear that the field of diabetes research is still learning the depth of the problem it seeks to solve and is struggling to adopt many of the emerging technologies today to address it. Many of the published assays remain simple and fail to replicate the complexity of the disease. For far too long has the focus been on just the beta-cells. Reality shows that the beta-cells are just one part of a much larger and delicate system. One that simply cannot be replicated with a rat insulinoma cell line in a dish. Until extremely recently, the next best option to a murine insulinoma cell line was cadaveric islets.

Fortunately, advances in both high-content imaging and stem cell research provide an extremely promising path for diabetes research. Refinement of these techniques will provide labs with the ability to develop islets from a diverse biobank of donors, when needed, in a way that allows the diversity of the problem we face to be accurately replicated and studied. There is so much more that can occur within an islet than merely the increase in beta-cell proliferation. More studies are showing the ability of endocrine cell types to convert to another endocrine cell type partially or completely. This paired with the ability for the islet substructure to dramatically change displays the importance of continuing this research in three dimensions.

Finally, the future of the GNF-9228 scaffold as a therapeutic is slim at best. While the research here does provide some avenues forward through modification of the core hydroxyl and further exploration of electron-donating substituents on the aniline could produce more metabolically stable analogs. Furthermore, the methoxy core held so much promise but we never tested it *in vivo* to see if clearance was slowed. The most valuable contribution of GNF-9228 to the field of beta-cell replication will likely come from discerning what pathway it acts on that is separate to DYRK1A. Unfortunately, at this time, it is hard to envision any modifications that would take this scaffold down to the nanomolar potency required to be therapeutic. That's if it proves to be beta cell or even endocrine specific as the kinome analysis would suggest otherwise. Nonetheless, the exploration of this molecule has provided not only a probe for beta-cell modulation, but also led to the generation of a series of tools that should be widely applicable to this research field as a whole

Bibliography

(1) Magliano, D.; Boyko, E. J. *IDF Diabetes Atlas*; International Diabetes Federation, 2021.
(2) Christensen, A. A.; Gannon, M. The Beta Cell in Type 2 Diabetes. *Curr. Diab. Rep.* **2019**, *19* (9), 81.
(3) Lytrivi, M.; Castell, A.-L.; Poitout, V.; Cnop, M. Recent Insights Into Mechanisms of β-Cell Lipo- and Glucolipotoxicity in Type 2 Diabetes. *J. Mol. Biol.* **2020**, *432* (5), 1514–1534.
(4) Chera, S.; Baronnier, D.; Ghila, L.; Cigliola, V.; Jensen, J. N.; Gu, G.; Furuyama, K.; Thorel, F.; Gribble, F. M.; Reimann, F.; Herrera, P. L. Diabetes Recovery by Age-Dependent Conversion of Pancreatic δ-Cells into Insulin Producers. *Nature* **2014**, *514* (7523), 503–507.
(5) Thorel, F.; Népote, V.; Avril, I.; Kohno, K.; Desgraz, R.; Chera, S.; Herrera, P. L. Conversion of Adult Pancreatic Alpha-Cells to Beta-Cells after Extreme Beta-Cell Loss. *Nature* **2010**, *464* (7292), 1149–1154.
(6) Wingfield, J. Bioassays | High-Throughput Screening. In *Encyclopedia of Analytical Science (Third Edition)*; Worsfold, P., Poole, C., Townshend, A., Miró, M., Eds.; Academic Press: Oxford, 2019; pp 278–282.
(7) Hohmeier, H. E.; Newgard, C. B. Cell Lines Derived from Pancreatic Islets. *Mol. Cell. Endocrinol.* **2004**, *228* (1–2), 121–128.
(8) Ravassard, P.; Hazhouz, Y.; Pechberty, S.; Bricout-Neveu, E.; Armanet, M.; Czernichow, P.; Scharfmann, R. A Genetically Engineered Human Pancreatic β Cell Line Exhibiting Glucose-Inducible Insulin Secretion. *J. Clin. Invest.* **2011**, *121* (9), 3589–3597.
(9) *PubChem Classification Browser*. https://pubchem.ncbi.nlm.nih.gov/classification/ (accessed 2023-08-18).
(10) Wang, W.; Walker, J. R.; Wang, X.; Tremblay, M. S.; Lee, J. W.; Wu, X.; Schultz, P. G. Identification of Small-Molecule Inducers of Pancreatic β-Cell Expansion. *Proceedings of the National Academy of Sciences* **2009**, *106* (5), 1427–1432.
(11) Shen, W.; Tremblay, M. S.; Deshmukh, V. A.; Wang, W.; Filippi, C. M.; Harb, G.; Zhang, Y.-Q.; Kamireddy, A.; Baaten, J. E.; Jin, Q.; Wu, T.; Swoboda, J. G.; Cho, C. Y.; Li, J.; Laffitte, B. A.; McNamara, P.; Glynne, R.; Wu, X.; Herman, A. E.; Schultz, P. G. Small-Molecule Inducer of β Cell Proliferation Identified by High-Throughput Screening. *J. Am. Chem. Soc.* **2013**, *135* (5), 1669–1672.
(12) Shen, W.; Taylor, B.; Jin, Q.; Nguyen-Tran, V.; Meeusen, S.; Zhang, Y.-Q.; Kamireddy, A.; Swafford, A.; Powers, A. F.; Walker, J.; Lamb, J.; Bursalaya, B.; DiDonato, M.; Harb, G.; Qiu, M.; Filippi, C. M.; Deaton, L.; Turk, C. N.; Suarez-Pinzon, W. L.; Liu, Y.; Hao, X.; Mo, T.; Yan, S.; Li, J.; Herman, A. E.; Hering, B. J.; Wu, T.; Martin Seidel, H.; McNamara, P.; Glynne, R.; Laffitte, B. Inhibition of DYRK1A and GSK3B Induces Human β-Cell Proliferation. *Nat. Commun.* **2015**, *6*, 8372.

(13) Boden, G. Obesity and Free Fatty Acids. *Endocrinol. Metab. Clin. North Am.* **2008**, *37* (3), 635–646, viii–ix.
(14) Lee, S.-H.; Cunha, D.; Piermarocchi, C.; Paternostro, G.; Pinkerton, A.; Ladriere, L.; Marchetti, P.; Eizirik, D. L.; Cnop, M.; Levine, F. High-Throughput Screening and Bioinformatic Analysis to Ascertain Compounds That Prevent Saturated Fatty Acid-Induced β-Cell Apoptosis. *Biochem. Pharmacol.* **2017**, *138*, 140–149.
(15) Vogel, J.; Yin, J.; Su, L.; Wang, S. X.; Zessis, R.; Fowler, S.; Chiu, C.-H.; Wilson, A. C.; Chen, A.; Zecri, F.; Turner, G.; Smith, T. M.; DeChristopher, B.; Xing, H.; Rothman, D. M.; Cai, X.; Berdichevsky, A. A Phenotypic Screen Identifies Calcium Overload as a Key Mechanism of β-Cell Glucolipotoxicity. *Diabetes* **2020**, *69* (5), 1032–1041.
(16) Chou, D. H.-C.; Bodycombe, N. E.; Carrinski, H. A.; Lewis, T. A.; Clemons, P. A.; Schreiber, S. L.; Wagner, B. K. Small-Molecule Suppressors of Cytokine-Induced Beta-Cell Apoptosis. *ACS Chem. Biol.* **2010**, *5* (8), 729–734.
(17) Wang, P.; Alvarez-Perez, J.-C.; Felsenfeld, D. P.; Liu, H.; Sivendran, S.; Bender, A.; Kumar, A.; Sanchez, R.; Scott, D. K.; Garcia-Ocaña, A.; Stewart, A. F. A High-Throughput Chemical Screen Reveals That Harmine-Mediated Inhibition of DYRK1A Increases Human Pancreatic Beta Cell Replication. *Nat. Med.* **2015**, *21* (4), 383–388.
(18) Rudnick, A.; Ling, T. Y.; Odagiri, H.; Rutter, W. J.; German, M. S. Pancreatic Beta Cells Express a Diverse Set of Homeobox Genes. *Proc. Natl. Acad. Sci. U. S. A.* **1994**, *91* (25), 12203–12207.
(19) Schisler, J. C.; Jensen, P. B.; Taylor, D. G.; Becker, T. C.; Knop, F. K.; Takekawa, S.; German, M.; Weir, G. C.; Lu, D.; Mirmira, R. G.; Newgard, C. B. The Nkx6.1 Homeodomain Transcription Factor Suppresses Glucagon Expression and Regulates Glucose-Stimulated Insulin Secretion in Islet Beta Cells. *Proc. Natl. Acad. Sci. U. S. A.* **2005**, *102* (20), 7297–7302.
(20) Schisler, J. C.; Fueger, P. T.; Babu, D. A.; Hohmeier, H. E.; Tessem, J. S.; Lu, D.; Becker, T. C.; Naziruddin, B.; Levy, M.; Mirmira, R. G.; Newgard, C. B. Stimulation of Human and Rat Islet Beta-Cell Proliferation with Retention of Function by the Homeodomain Transcription Factor Nkx6.1. *Mol. Cell. Biol.* **2008**, *28* (10), 3465–3476.
(21) Stephens, S. B.; Schisler, J. C.; Hohmeier, H. E.; An, J.; Sun, A. Y.; Pitt, G. S.; Newgard, C. B. A VGF-Derived Peptide Attenuates Development of Type 2 Diabetes via Enhancement of Islet β-Cell Survival and Function. *Cell Metab.* **2012**, *16* (1), 33–43.
(22) Hohmeier, H. E.; Zhang, L.; Taylor, B.; Stephens, S.; Lu, D.; McNamara, P.; Laffitte, B.; Newgard, C. B. Identification of a Small Molecule That Stimulates Human β-Cell Proliferation and Insulin Secretion, and Protects against Cytotoxic Stress in Rat Insulinoma Cells. *PLoS One* **2020**, *15* (3), e0224344.
(23) Thorne, N.; Shen, M.; Lea, W. A.; Simeonov, A.; Lovell, S.; Auld, D. S.; Inglese, J. Firefly Luciferase in Chemical Biology: A Compendium of Inhibitors, Mechanistic Evaluation of Chemotypes, and Suggested Use as a Reporter. *Chem. Biol.* **2012**, *19* (8), 1060–1072.
(24) Thorne, N.; Inglese, J.; Auld, D. S. Illuminating Insights into Firefly Luciferase and Other Bioluminescent Reporters Used in Chemical Biology. *Chem. Biol.* **2010**, *17* (6), 646–657.
(25) Zamaraeva, M. V.; Sabirov, R. Z.; Maeno, E.; Ando-Akatsuka, Y.; Bessonova, S. V.; Okada, Y. Cells Die with Increased Cytosolic ATP during Apoptosis: A Bioluminescence Study with Intracellular Luciferase. *Cell Death Differ.* **2005**, *12* (11), 1390–1397.
(26) Auld, D. S.; Inglese, J. *Interferences with Luciferase Reporter Enzymes*; Eli Lilly & Company and the National Center for Advancing Translational Sciences, 2018.

(27) Sherf, B. A.; Navarro, S. L.; Hannah, R. R.; Wood, K. V. *Dual-LuciferaseTM reporter assay: An advanced co-reporter technology integrating firefly and Renilla Luciferase assays*. https://citeseerx.ist.psu.edu/document?repid=rep1&type=pdf&doi=a798b2a51acc2a146bbeb4705a4168f15baf3b6f (accessed 2023-10-05).
(28) England, C. G.; Ehlerding, E. B.; Cai, W. NanoLuc: A Small Luciferase Is Brightening Up the Field of Bioluminescence. *Bioconjug. Chem.* **2016**, *27* (5), 1175–1187.
(29) Fonseca, V. A. Defining and Characterizing the Progression of Type 2 Diabetes. *Diabetes Care* **2009**, *32* (Suppl 2), S151.
(30) Weyer, C.; Tataranni, P. A.; Bogardus, C.; Pratley, R. E. Insulin Resistance and Insulin Secretory Dysfunction Are Independent Predictors of Worsening of Glucose Tolerance during Each Stage of Type 2 Diabetes Development. *Diabetes Care* **2001**, *24* (1), 89–94.
(31) Festa, A.; Williams, K.; D'Agostino, R., Jr; Wagenknecht, L. E.; Haffner, S. M. The Natural Course of Beta-Cell Function in Nondiabetic and Diabetic Individuals: The Insulin Resistance Atherosclerosis Study. *Diabetes* **2006**, *55* (4), 1114–1120.
(32) Bielefeld-Sevigny, M. AlphaLISA Immunoassay Platform- the "No-Wash" High-Throughput Alternative to ELISA. *Assay Drug Dev. Technol.* **2009**, *7* (1), 90–92.
(33) Degorce, F. HTRF(®): Pioneering Technology for High-Throughput Screening. *Expert Opin. Drug Discov.* **2006**, *1* (7), 753–764.
(34) Coussens, N. P.; Auld, D.; Roby, P.; Walsh, J.; Baell, J. B.; Kales, S.; Hadian, K.; Dahlin, J. L. *Compound-Mediated Assay Interferences in Homogeneous Proximity Assays*; Eli Lilly & Company and the National Center for Advancing Translational Sciences, 2020.
(35) Watkins, S.; Geng, X.; Li, L.; Papworth, G.; Robbins, P. D.; Drain, P. Imaging Secretory Vesicles by Fluorescent Protein Insertion in Propeptide Rather than Mature Secreted Peptide. *Traffic* **2002**, *3* (7), 461–471.
(36) Burns, S. M.; Vetere, A.; Walpita, D.; Dančík, V.; Khodier, C.; Perez, J.; Clemons, P. A.; Wagner, B. K.; Altshuler, D. High-Throughput Luminescent Reporter of Insulin Secretion for Discovering Regulators of Pancreatic Beta-Cell Function. *Cell Metab.* **2015**, *21* (1), 126–137.
(37) Kalwat, M. A.; Wichaidit, C.; Nava Garcia, A. Y.; McCoy, M. K.; McGlynn, K.; Hwang, I. H.; MacMillan, J. B.; Posner, B. A.; Cobb, M. H. Insulin Promoter-Driven Gaussia Luciferase-Based Insulin Secretion Biosensor Assay for Discovery of β-Cell Glucose-Sensing Pathways. *ACS Sens* **2016**, *1* (10), 1208–1212.
(38) Hager, R.; Pitsch, J.; Kerbl-Knapp, J.; Neuhauser, C.; Ollinger, N.; Iken, M.; Ranner, J.; Mittermeier-Kleßinger, V.; Dawid, C.; Lanzerstorfer, P.; Weghuber, J. A High-Content Screen for the Identification of Plant Extracts with Insulin Secretion-Modulating Activity. *Pharmaceuticals* **2021**, *14* (8). https://doi.org/10.3390/ph14080809.
(39) Delannoy, C. P.; Heuson, E.; Herledan, A.; Oger, F.; Thiroux, B.; Chevalier, M.; Gromada, X.; Rolland, L.; Froguel, P.; Deprez, B.; Paul, S.; Annicotte, J.-S. High-Throughput Quantitative Screening of Glucose-Stimulated Insulin Secretion and Insulin Content Using Automated MALDI-TOF Mass Spectrometry. *Cells* **2023**, *12* (6). https://doi.org/10.3390/cells12060849.
(40) Bickle, M. The Beautiful Cell: High-Content Screening in Drug Discovery. *Anal. Bioanal. Chem.* **2010**, *398* (1), 219–226.
(41) Singh, S.; Carpenter, A. E.; Genovesio, A. Increasing the Content of High-Content Screening: An Overview. *J. Biomol. Screen.* **2014**, *19* (5), 640–650.

(42) Stirling, D. R.; Swain-Bowden, M. J.; Lucas, A. M.; Carpenter, A. E.; Cimini, B. A.; Goodman, A. CellProfiler 4: Improvements in Speed, Utility and Usability. *BMC Bioinformatics* **2021**, *22* (1), 433.
(43) Zhang, J. H.; Chung, T. D.; Oldenburg, K. R. A Simple Statistical Parameter for Use in Evaluation and Validation of High Throughput Screening Assays. *J. Biomol. Screen.* **1999**, *4* (2), 67–73.
(44) Mpindi, J.-P.; Swapnil, P.; Dmitrii, B.; Jani, S.; Saeed, K.; Wennerberg, K.; Aittokallio, T.; Östling, P.; Kallioniemi, O. Impact of Normalization Methods on High-Throughput Screening Data with High Hit Rates and Drug Testing with Dose-Response Data. *Bioinformatics* **2015**, *31* (23), 3815–3821.
(45) Brideau, C.; Gunter, B.; Pikounis, B.; Liaw, A. Improved Statistical Methods for Hit Selection in High-Throughput Screening. *J. Biomol. Screen.* **2003**, *8* (6), 634–647.
(46) Sexton, J. Z.; Fursmidt, R.; O'Meara, M. J.; Omta, W.; Rao, A.; Egan, D. A.; Haney, S. A. *Machine Learning and Assay Development for Image-Based Phenotypic Profiling of Drug Treatments*; Eli Lilly & Company and the National Center for Advancing Translational Sciences, 2023.
(47) Kiselyuk, A.; Farber-Katz, S.; Cohen, T.; Lee, S.-H.; Geron, I.; Azimi, B.; Heynen-Genel, S.; Singer, O.; Price, J.; Mercola, M.; Itkin-Ansari, P.; Levine, F. Phenothiazine Neuroleptics Signal to the Human Insulin Promoter as Revealed by a Novel High-Throughput Screen. *J. Biomol. Screen.* **2010**, *15* (6), 663–670.
(48) Kiselyuk, A.; Lee, S.-H.; Farber-Katz, S.; Zhang, M.; Athavankar, S.; Cohen, T.; Pinkerton, A. B.; Ye, M.; Bushway, P.; Richardson, A. D.; Hostetler, H. A.; Rodriguez-Lee, M.; Huang, L.; Spangler, B.; Smith, L.; Higginbotham, J.; Cashman, J.; Freeze, H.; Itkin-Ansari, P.; Dawson, M. I.; Schroeder, F.; Cang, Y.; Mercola, M.; Levine, F. HNF4α Antagonists Discovered by a High-Throughput Screen for Modulators of the Human Insulin Promoter. *Chem. Biol.* **2012**, *19* (7), 806–818.
(49) Szabat, M.; Luciani, D. S.; Piret, J. M.; Johnson, J. D. Maturation of Adult Beta-Cells Revealed Using a Pdx1/Insulin Dual-Reporter Lentivirus. *Endocrinology* **2009**, *150* (4), 1627–1635.
(50) Hill, J. A.; Szabat, M.; Hoesli, C. A.; Gage, B. K.; Yang, Y. H. C.; Williams, D. E.; Riedel, M. J.; Luciani, D. S.; Kalynyak, T. B.; Tsai, K.; Ao, Z.; Andersen, R. J.; Warnock, G. L.; Piret, J. M.; Kieffer, T. J.; Johnson, J. D. A Multi-Parameter, High-Content, High-Throughput Screening Platform to Identify Natural Compounds That Modulate Insulin and Pdx1 Expression. *PLoS One* **2010**, *5* (9), e12958.
(51) Szabat, M.; Modi, H.; Ramracheya, R.; Girbinger, V.; Chan, F.; Lee, J. T. C.; Piske, M.; Kamal, S.; Carol Yang, Y. H.; Welling, A.; Rorsman, P.; Johnson, J. D. High-Content Screening Identifies a Role for Na(+) Channels in Insulin Production. *R Soc Open Sci* **2015**, *2* (12), 150306.
(52) Chakravarthy, H.; Gu, X.; Enge, M.; Dai, X.; Wang, Y.; Damond, N.; Downie, C.; Liu, K.; Wang, J.; Xing, Y.; Chera, S.; Thorel, F.; Quake, S.; Oberholzer, J.; MacDonald, P. E.; Herrera, P. L.; Kim, S. K. Converting Adult Pancreatic Islet α Cells into β Cells by Targeting Both Dnmt1 and Arx. *Cell Metab.* **2017**, *25* (3), 622–634.
(53) Li, J.; Casteels, T.; Frogne, T.; Ingvorsen, C.; Honoré, C.; Courtney, M.; Huber, K. V. M.; Schmitner, N.; Kimmel, R. A.; Romanov, R. A.; Sturtzel, C.; Lardeau, C.-H.; Klughammer, J.; Farlik, M.; Sdelci, S.; Vieira, A.; Avolio, F.; Briand, F.; Baburin, I.; Májek, P.; Pauler, F. M.; Penz, T.; Stukalov, A.; Gridling, M.; Parapatics, K.; Barbieux, C.; Berishvili, E.;

Spittler, A.; Colinge, J.; Bennett, K. L.; Hering, S.; Sulpice, T.; Bock, C.; Distel, M.; Harkany, T.; Meyer, D.; Superti-Furga, G.; Collombat, P.; Hecksher-Sørensen, J.; Kubicek, S. Artemisinins Target GABAA Receptor Signaling and Impair α Cell Identity. *Cell* **2017**, *168* (1–2), 86-100.e15.

(54) Campbell, I. L.; Colman, P. G.; Harrison, L. C. Adult Human Pancreatic Islet Cells in Tissue Culture: Function and Immunoreactivity. *J. Clin. Endocrinol. Metab.* **1985**, *61* (4), 681–685.

(55) Peakman, M.; McNab, G. L.; Heaton, N. D.; Tan, K. C.; Vergani, D. Development of Techniques for Obtaining Monodispersed Human Islet Cells. *Transplantation* **1994**, *57* (3), 384–393.

(56) Otonkoski, T.; Banerjee, M.; Korsgren, O.; Thornell, L.-E.; Virtanen, I. Unique Basement Membrane Structure of Human Pancreatic Islets: Implications for Beta-Cell Growth and Differentiation. *Diabetes Obes. Metab.* **2008**, *10 Suppl 4*, 119–127.

(57) Walpita, D.; Wagner, B. K. Evaluation of Compounds in Primary Human Islet Cell Culture. *Curr. Protoc. Chem. Biol.* **2014**, *6* (3), 157–168.

(58) Mullooly, N.; Smith, D. M.; Gianni, D. A Multi-Parametric High Throughput Assay for Detecting Beta-Cell Proliferation in Dispersed Primary Islets. *SLAS Discov* **2023**, *28* (2), 3–12.

(59) Walpita, D.; Hasaka, T.; Spoonamore, J.; Vetere, A.; Takane, K. K.; Fomina-Yadlin, D.; Fiaschi-Taesch, N.; Shamji, A.; Clemons, P. A.; Stewart, A. F.; Schreiber, S. L.; Wagner, B. K. A Human Islet Cell Culture System for High-Throughput Screening. *J. Biomol. Screen.* **2012**, *17* (4), 509–518.

(60) Cully, M. Zebrafish Earn Their Drug Discovery Stripes. *Nat. Rev. Drug Discov.* **2019**, *18* (11), 811–813.

(61) Wang, G.; Rajpurohit, S. K.; Delaspre, F.; Walker, S. L.; White, D. T.; Ceasrine, A.; Kuruvilla, R.; Li, R.-J.; Shim, J. S.; Liu, J. O.; Parsons, M. J.; Mumm, J. S. First Quantitative High-Throughput Screen in Zebrafish Identifies Novel Pathways for Increasing Pancreatic β-Cell Mass. *Elife* **2015**, *4*. https://doi.org/10.7554/eLife.08261.

(62) Sakaue-Sawano, A.; Kurokawa, H.; Morimura, T.; Hanyu, A.; Hama, H.; Osawa, H.; Kashiwagi, S.; Fukami, K.; Miyata, T.; Miyoshi, H.; Imamura, T.; Ogawa, M.; Masai, H.; Miyawaki, A. Visualizing Spatiotemporal Dynamics of Multicellular Cell-Cycle Progression. *Cell* **2008**, *132* (3), 487–498.

(63) Tsuji, N.; Ninov, N.; Delawary, M.; Osman, S.; Roh, A. S.; Gut, P.; Stainier, D. Y. R. Whole Organism High Content Screening Identifies Stimulators of Pancreatic Beta-Cell Proliferation. *PLoS One* **2014**, *9* (8), e104112.

(64) Charbord, J.; Ren, L.; Sharma, R. B.; Johansson, A.; Ågren, R.; Chu, L.; Tworus, D.; Schulz, N.; Charbord, P.; Stewart, A. F.; Wang, P.; Alonso, L. C.; Andersson, O. In Vivo Screen Identifies a SIK Inhibitor That Induces β Cell Proliferation through a Transient UPR. *Nat Metab* **2021**, *3* (5), 682–700.

(65) Blackburn, J. S.; Liu, S.; Raimondi, A. R.; Ignatius, M. S.; Salthouse, C. D.; Langenau, D. M. High-Throughput Imaging of Adult Fluorescent Zebrafish with an LED Fluorescence Macroscope. *Nat. Protoc.* **2011**, *6* (2), 229–241.

(66) Kulkarni, R. N.; Mizrachi, E.-B.; Ocana, A. G.; Stewart, A. F. Human β-Cell Proliferation and Intracellular Signaling: Driving in the Dark without a Road Map. *Diabetes* **2012**, *61* (9), 2205–2213.

(67) Segerstolpe, Å.; Palasantza, A.; Eliasson, P.; Andersson, E.-M.; Andréasson, A.-C.; Sun, X.; Picelli, S.; Sabirsh, A.; Clausen, M.; Bjursell, M. K.; Smith, D. M.; Kasper, M.; Ämmälä, C.; Sandberg, R. Single-Cell Transcriptome Profiling of Human Pancreatic Islets in Health and Type 2 Diabetes. *Cell Metab.* **2016**, *24* (4), 593–607.
(68) Friedlander, M. S. H.; Nguyen, V. M.; Kim, S. K.; Bevacqua, R. J. Pancreatic Pseudoislets: An Organoid Archetype for Metabolism Research. *Diabetes* **2021**, *70* (5), 1051–1060.
(69) Mir-Coll, J.; Moede, T.; Paschen, M.; Neelakandhan, A.; Valladolid-Acebes, I.; Leibiger, B.; Biernath, A.; Ämmälä, C.; Leibiger, I. B.; Yesildag, B.; Berggren, P.-O. Human Islet Microtissues as an In Vitro and an In Vivo Model System for Diabetes. *Int. J. Mol. Sci.* **2021**, *22* (4). https://doi.org/10.3390/ijms22041813.
(70) Caton, D.; Calabrese, A.; Mas, C.; Serre-Beinier, V.; Charollais, A.; Caille, D.; Zufferey, R.; Trono, D.; Meda, P. Lentivirus-Mediated Transduction of Connexin CDNAs Shows Level- and Isoform-Specific Alterations in Insulin Secretion of Primary Pancreatic Beta-Cells. *J. Cell Sci.* **2003**, *116* (Pt 11), 2285–2294.
(71) Arda, H. E.; Li, L.; Tsai, J.; Torre, E. A.; Rosli, Y.; Peiris, H.; Spitale, R. C.; Dai, C.; Gu, X.; Qu, K.; Wang, P.; Wang, J.; Grompe, M.; Scharfmann, R.; Snyder, M. S.; Bottino, R.; Powers, A. C.; Chang, H. Y.; Kim, S. K. Age-Dependent Pancreatic Gene Regulation Reveals Mechanisms Governing Human β Cell Function. *Cell Metab.* **2016**, *23* (5), 909–920.
(72) Cavallari, G.; Zuellig, R. A.; Lehmann, R.; Weber, M.; Moritz, W. Rat Pancreatic Islet Size Standardization by the "Hanging Drop" Technique. *Transplant. Proc.* **2007**, *39* (6), 2018–2020.
(73) Liu, D.; Chen, S.; Win Naing, M. A Review of Manufacturing Capabilities of Cell Spheroid Generation Technologies and Future Development. *Biotechnol. Bioeng.* **2021**, *118* (2), 542–554.
(74) Title, A. C.; Karsai, M.; Mir-Coll, J.; Grining, Ö. Y.; Rufer, C.; Sonntag, S.; Forschler, F.; Jawurek, S.; Klein, T.; Yesildag, B. Evaluation of the Effects of Harmine on β-Cell Function and Proliferation in Standardized Human Islets Using 3D High-Content Confocal Imaging and Automated Analysis. *Front. Endocrinol.* **2022**, *13*, 854094.
(75) McCarty, S. M.; Clasby, M. C.; Sexton, J. Z. Automated High-Throughput, High-Content 3D Imaging of Intact Pancreatic Islets. *SLAS Discov* **2023**. https://doi.org/10.1016/j.slasd.2023.07.003.
(76) Balboa, D.; Iworima, D. G.; Kieffer, T. J. Human Pluripotent Stem Cells to Model Islet Defects in Diabetes. *Front. Endocrinol.* **2021**, *12*, 642152.
(77) Wang, X.; Gao, M.; Wang, Y.; Zhang, Y. The Progress of Pluripotent Stem Cell-Derived Pancreatic β-Cells Regeneration for Diabetic Therapy. *Front. Endocrinol.* **2022**, *13*, 927324.
(78) Bealer, E.; Crumley, K.; Clough, D.; King, J.; Behrend, M.; Annulis, C.; Li, F.; Soleimanpour, S.; Shea, L. D. Extrahepatic Transplantation of 3D Cultured Stem Cell-Derived Islet Organoids on Microporous Scaffolds. *Biomater Sci* **2023**, *11* (10), 3645–3655.
(79) *Novel Therapy to Preserve Beta Cell Function in New Onset Type 1 Diabetes*. https://clinicaltrials.gov/study/NCT00837759?cond=Diabetes&term=Beta-cell%20Function&page=7&rank=61 (accessed 2023-10-03).
(80) *Verapamil SR in Adults With Type 1 Diabetes (Ver-A-T1D)*. https://clinicaltrials.gov/study/NCT04545151?cond=Diabetes&aggFilters=results:without,status:rec&term=Beta-cell%20Function&rank=24 (accessed 2023-10-03).

(81) Yin, T.; Kuo, S.-C.; Chang, Y.-Y.; Chen, Y.-T.; Wang, K.-W. K. Verapamil Use Is Associated With Reduction of Newly Diagnosed Diabetes Mellitus. *J. Clin. Endocrinol. Metab.* **2017**, *102* (7), 2604–2610.
(82) Xu, G.; Chen, J.; Jing, G.; Shalev, A. Preventing β-Cell Loss and Diabetes with Calcium Channel Blockers. *Diabetes* **2012**, *61* (4), 848–856.
(83) Thompson, P. J.; Shah, A.; Ntranos, V.; Van Gool, F.; Atkinson, M.; Bhushan, A. Targeted Elimination of Senescent Beta Cells Prevents Type 1 Diabetes. *Cell Metab.* **2019**, *29* (5), 1045-1060.e10.
(84) *LIraglutide and Beta-cell RepAir (LIBRA) Study (LIBRA)*. https://clinicaltrials.gov/study/NCT01270789?cond=Diabetes&term=Beta-cell%20Function&page=3&rank=23 (accessed 2023-10-03).
(85) *Effects of Liraglutide on ER Stress in Obese Patients With Type 2 Diabetes*. https://clinicaltrials.gov/study/NCT02344186?cond=Diabetes&aggFilters=results:without,status:act&term=Beta-cell%20Function&rank=10 (accessed 2023-10-03).
(86) *Fingolimod for Type 2 Diabetes Mellitus*. https://clinicaltrials.gov/study/NCT05307731?cond=Diabetes&aggFilters=results:without,status:rec&term=Beta-cell%20Function&rank=37 (accessed 2023-10-03).
(87) Khan, M. A. B.; Hashim, M. J.; King, J. K.; Govender, R. D.; Mustafa, H.; Al Kaabi, J. Epidemiology of Type 2 Diabetes - Global Burden of Disease and Forecasted Trends. *J. Epidemiol. Glob. Health* **2020**, *10* (1), 107–111.
(88) International Diabetes Federation. *IDF Diabetes Atlas*; International Diabetes Federation, 2015.
(89) Saisho, Y. β-Cell Dysfunction: Its Critical Role in Prevention and Management of Type 2 Diabetes. *World J. Diabetes* **2015**, *6* (1), 109–124.
(90) Cerf, M. E. Beta Cell Dysfunction and Insulin Resistance. *Front. Endocrinol.* **2013**, *4*, 37.
(91) Crunkhorn, S. Gene Therapy: Reprogramming α-Cells Reverses Diabetes. *Nat. Rev. Drug Discov.* **2018**, *17* (2), 93.
(92) Xiao, X.; Guo, P.; Shiota, C.; Zhang, T.; Coudriet, G. M.; Fischbach, S.; Prasadan, K.; Fusco, J.; Ramachandran, S.; Witkowski, P.; Piganelli, J. D.; Gittes, G. K. Endogenous Reprogramming of Alpha Cells into Beta Cells, Induced by Viral Gene Therapy, Reverses Autoimmune Diabetes. *Cell Stem Cell* **2018**, *22* (1), 78-90.e4.
(93) Guo, P.; Zhang, T.; Lu, A.; Shiota, C.; Huard, M.; Whitney, K. E.; Huard, J. Specific Reprogramming of Alpha Cells to Insulin-Producing Cells by Short Glucagon Promoter-Driven Pdx1 and MafA. *Mol Ther Methods Clin Dev* **2023**, *28*, 355–365.
(94) Clough, D. W.; King, J. L.; Li, F.; Shea, L. D. Integration of Islet/Beta-Cell Transplants with Host Tissue Using Biomaterial Platforms. *Endocrinology* **2020**, *161* (11). https://doi.org/10.1210/endocr/bqaa156.
(95) Kalwat, M. A. High-Throughput Screening for Insulin Secretion Modulators. In *Exocytosis and Endocytosis: Methods and Protocols*; Niedergang, F., Vitale, N., Gasman, S., Eds.; Springer US: New York, NY, 2021; pp 131–138.
(96) *Liu et al., 2020*. https://sciwheel.com/work/item/9128176/resources/8704123/pdf (accessed 2023-03-17).
(97) Hilderink, J.; Spijker, S.; Carlotti, F.; Lange, L.; Engelse, M.; van Blitterswijk, C.; de Koning, E.; Karperien, M.; van Apeldoorn, A. Controlled Aggregation of Primary Human Pancreatic Islet Cells Leads to Glucose-Responsive Pseudoislets Comparable to Native Islets. *J. Cell. Mol. Med.* **2015**, *19* (8), 1836–1846.

(98) Amin, J.; Ramachandran, K.; Williams, S. J.; Lee, A.; Novikova, L.; Stehno-Bittel, L. A Simple, Reliable Method for High-Throughput Screening for Diabetes Drugs Using 3D β-Cell Spheroids. *J. Pharmacol. Toxicol. Methods* **2016**, *82*, 83–89.
(99) Stringer, C.; Wang, T.; Michaelos, M.; Pachitariu, M. Cellpose: A Generalist Algorithm for Cellular Segmentation. *Nat. Methods* **2021**, *18* (1), 100–106.
(100) Berthold, M. R.; Cebron, N.; Dill, F.; Gabriel, T. R.; Kötter, T.; Meinl, T.; Ohl, P.; Sieb, C.; Thiel, K.; Wiswedel, B. KNIME: The KOnstanz INformation MIner. In *Studies in Classification, Data Analysis, and Knowledge Organization (GfKL 2007)*; Springer, 2007.
(101) Dekkers, J. F.; Alieva, M.; Wellens, L. M.; Ariese, H. C. R.; Jamieson, P. R.; Vonk, A. M.; Amatngalim, G. D.; Hu, H.; Oost, K. C.; Snippert, H. J. G.; Beekman, J. M.; Wehrens, E. J.; Visvader, J. E.; Clevers, H.; Rios, A. C. High-Resolution 3D Imaging of Fixed and Cleared Organoids. *Nat. Protoc.* **2019**, *14* (6), 1756–1771.
(102) Zmuda, E. J.; Powell, C. A.; Hai, T. A Method for Murine Islet Isolation and Subcapsular Kidney Transplantation. *J. Vis. Exp.* **2011**, No. 50. https://doi.org/10.3791/2096.
(103) Kim, A.; Miller, K.; Jo, J.; Kilimnik, G.; Wojcik, P.; Hara, M. Islet Architecture: A Comparative Study. *Islets* **2009**, *1* (2), 129–136.
(104) Steiner, D. J.; Kim, A.; Miller, K.; Hara, M. Pancreatic Islet Plasticity: Interspecies Comparison of Islet Architecture and Composition. *Islets* **2010**, *2* (3), 135–145.
(105) Elayat, A. A.; el-Naggar, M. M.; Tahir, M. An Immunocytochemical and Morphometric Study of the Rat Pancreatic Islets. *J. Anat.* **1995**, *186 (Pt 3)* (Pt 3), 629–637.
(106) Kharouta, M.; Miller, K.; Kim, A.; Wojcik, P.; Kilimnik, G.; Dey, A.; Steiner, D. F.; Hara, M. No Mantle Formation in Rodent Islets -- the Prototype of Islet Revisited. *Diabetes Res. Clin. Pract.* **2009**, *85* (3), 252–257.
(107) Dirice, E.; Walpita, D.; Vetere, A.; Meier, B. C.; Kahraman, S.; Hu, J.; Dančík, V.; Burns, S. M.; Gilbert, T. J.; Olson, D. E.; Clemons, P. A.; Kulkarni, R. N.; Wagner, B. K. Inhibition of DYRK1A Stimulates Human β-Cell Proliferation. *Diabetes* **2016**, *65* (6), 1660–1671.
(108) Kumar, K.; Wang, P.; Wilson, J.; Zlatanic, V.; Berrouet, C.; Khamrui, S.; Secor, C.; Swartz, E. A.; Lazarus, M.; Sanchez, R.; Stewart, A. F.; Garcia-Ocana, A.; DeVita, R. J. Synthesis and Biological Validation of a Harmine-Based, Central Nervous System (CNS)-Avoidant, Selective, Human β-Cell Regenerative Dual-Specificity Tyrosine Phosphorylation-Regulated Kinase A (DYRK1A) Inhibitor. *J. Med. Chem.* **2020**, *63* (6), 2986–3003.
(109) *Diabetes*. https://www.who.int/news-room/fact-sheets/detail/diabetes (accessed 2023-08-15).
(110) Chen, C.; Cohrs, C. M.; Stertmann, J.; Bozsak, R.; Speier, S. Human Beta Cell Mass and Function in Diabetes: Recent Advances in Knowledge and Technologies to Understand Disease Pathogenesis. *Mol Metab* **2017**, *6* (9), 943–957.
(111) Defronzo, R. A. Banting Lecture. From the Triumvirate to the Ominous Octet: A New Paradigm for the Treatment of Type 2 Diabetes Mellitus. *Diabetes* **2009**, *58* (4), 773–795.
(112) Kahn, S. E.; Haffner, S. M.; Heise, M. A.; Herman, W. H.; Holman, R. R.; Jones, N. P.; Kravitz, B. G.; Lachin, J. M.; O'Neill, M. C.; Zinman, B.; Viberti, G.; ADOPT Study Group. Glycemic Durability of Rosiglitazone, Metformin, or Glyburide Monotherapy. *N. Engl. J. Med.* **2006**, *355* (23), 2427–2443.
(113) Yki-Järvinen, H. Thiazolidinediones. *N. Engl. J. Med.* **2004**, *351* (11), 1106–1118.

(114) Shirakawa, J.; Kulkarni, R. N. Novel Factors Modulating Human β-Cell Proliferation. *Diabetes Obes. Metab.* **2016**, *18 Suppl 1* (Suppl 1), 71–77.
(115) Annes, J. P.; Ryu, J. H.; Lam, K.; Carolan, P. J.; Utz, K.; Hollister-Lock, J.; Arvanites, A. C.; Rubin, L. L.; Weir, G.; Melton, D. A. Adenosine Kinase Inhibition Selectively Promotes Rodent and Porcine Islet β-Cell Replication. *Proc. Natl. Acad. Sci. U. S. A.* **2012**, *109* (10), 3915–3920.
(116) Ogawa, Y.; Nonaka, Y.; Goto, T.; Ohnishi, E.; Hiramatsu, T.; Kii, I.; Yoshida, M.; Ikura, T.; Onogi, H.; Shibuya, H.; Hosoya, T.; Ito, N.; Hagiwara, M. Development of a Novel Selective Inhibitor of the Down Syndrome-Related Kinase Dyrk1A. *Nat. Commun.* **2010**, *1*, 86.
(117) Liu, Y. A.; Jin, Q.; Zou, Y.; Ding, Q.; Yan, S.; Wang, Z.; Hao, X.; Nguyen, B.; Zhang, X.; Pan, J.; Mo, T.; Jacobsen, K.; Lam, T.; Wu, T. Y.-H.; Petrassi, H. M.; Bursulaya, B.; DiDonato, M.; Gordon, W. P.; Liu, B.; Baaten, J.; Hill, R.; Nguyen-Tran, V.; Qiu, M.; Zhang, Y.-Q.; Kamireddy, A.; Espinola, S.; Deaton, L.; Ha, S.; Harb, G.; Jia, Y.; Li, J.; Shen, W.; Schumacher, A. M.; Colman, K.; Glynne, R.; Pan, S.; McNamara, P.; Laffitte, B.; Meeusen, S.; Molteni, V.; Loren, J. Selective DYRK1A Inhibitor for the Treatment of Type 1 Diabetes: Discovery of 6-Azaindole Derivative GNF2133. *J. Med. Chem.* **2020**, *63* (6), 2958–2973.
(118) Carmean, C. M.; Zhao, L.; Landeche, M.; Chellan, B.; Sargis, R. M. Dimethyl Sulfoxide Acutely Enhances Regulated Insulin Secretion in the MIN6-K8 Mouse Insulinoma Cell Line. *Histochem. Cell Biol.* **2021**, *156* (1), 69–73.
(119) McCarty, S.; Sexton, J. *Automated High-Throughput, High-Content Imaging of Intact Pancreatic Islets*; 2023. https://doi.org/10.5281/zenodo.7864552.
(120) Albanese, A.; Swaney, J. M.; Yun, D. H.; Evans, N. B.; Antonucci, J. M.; Velasco, S.; Sohn, C. H.; Arlotta, P.; Gehrke, L.; Chung, K. Multiscale 3D Phenotyping of Human Cerebral Organoids. *Sci. Rep.* **2020**, *10* (1), 21487.
(121) Vilsmeier, A.; Haack, A. Über Die Einwirkung von Halogenphosphor Auf Alkyl-formanilide. Eine Neue Methode Zur Darstellung Sekundärer Und Tertiärer p -Alkylamino-benzaldehyde. *Ber. dtsch. Chem. Ges. A/B* **1927**, *60* (1), 119–122.
(122) Jones, G.; Stanforth, S. P. The Vilsmeier Reaction of Fully Conjugated Carbocycles and Heterocycles. *Organic Reactions*; John Wiley & Sons, Inc.: Hoboken, NJ, USA, 1996; pp 1–330. https://doi.org/10.1002/0471264180.or049.01.
(123) Wang, K.; Nguyen, K.; Huang, Y.; Dömling, A. Cyanoacetamide Multicomponent Reaction (I): Parallel Synthesis of Cyanoacetamides. *J. Comb. Chem.* **2009**, *11* (5), 920–927.
(124) Burke, T. R., Jr; Lim, B.; Marquez, V. E.; Li, Z. H.; Bolen, J. B.; Stefanova, I.; Horak, I. D. Bicyclic Compounds as Ring-Constrained Inhibitors of Protein-Tyrosine Kinase P56lck. *J. Med. Chem.* **1993**, *36* (4), 425–432.
(125) Zubkov, V. A.; Kovalenko, S. N.; Chernykh, V. P.; Ivkov, S. M. New Derivatives of Coumarin: 2-(N-R-Imino)-2H-1-Benzopyrans. *Chem. Heterocycl. Compd.* **1994**, *30* (6), 665–670.
(126) Ackeifi, C.; Swartz, E.; Kumar, K.; Liu, H.; Chalada, S.; Karakose, E.; Scott, D. K.; Garcia-Ocaña, A.; Sanchez, R.; DeVita, R. J.; Stewart, A. F.; Wang, P. Pharmacologic and Genetic Approaches Define Human Pancreatic β Cell Mitogenic Targets of DYRK1A Inhibitors. *JCI Insight* **2020**, *5* (1). https://doi.org/10.1172/jci.insight.132594.

(127) Schittek, B.; Sinnberg, T. Biological Functions of Casein Kinase 1 Isoforms and Putative Roles in Tumorigenesis. *Mol. Cancer* **2014**, *13*, 231.
(128) Varjosalo, M.; Keskitalo, S.; Van Drogen, A.; Nurkkala, H.; Vichalkovski, A.; Aebersold, R.; Gstaiger, M. The Protein Interaction Landscape of the Human CMGC Kinase Group. *Cell Rep.* **2013**, *3* (4), 1306–1320.
(129) Camunas-Soler, J.; Dai, X.-Q.; Hang, Y.; Bautista, A.; Lyon, J.; Suzuki, K.; Kim, S. K.; Quake, S. R.; MacDonald, P. E. Patch-Seq Links Single-Cell Transcriptomes to Human Islet Dysfunction in Diabetes. *Cell Metab.* **2020**, *31* (5), 1017-1031.e4.
(130) Shaik, J. B.; Palaka, B. K.; Penumala, M.; Kotapati, K. V.; Devineni, S. R.; Eadlapalli, S.; Darla, M. M.; Ampasala, D. R.; Vadde, R.; Amooru, G. D. Synthesis, Pharmacological Assessment, Molecular Modeling and in Silico Studies of Fused Tricyclic Coumarin Derivatives as a New Family of Multifunctional Anti-Alzheimer Agents. *Eur. J. Med. Chem.* **2016**, *107*, 219–232.
(131) *KINOMEscan Technology*. https://www.eurofinsdiscovery.com/solution/kinomescan-technology (accessed 2023-10-18).
(132) Hao, Y.; Hao, S.; Andersen-Nissen, E.; Mauck, W. M., 3rd; Zheng, S.; Butler, A.; Lee, M. J.; Wilk, A. J.; Darby, C.; Zager, M.; Hoffman, P.; Stoeckius, M.; Papalexi, E.; Mimitou, E. P.; Jain, J.; Srivastava, A.; Stuart, T.; Fleming, L. M.; Yeung, B.; Rogers, A. J.; McElrath, J. M.; Blish, C. A.; Gottardo, R.; Smibert, P.; Satija, R. Integrated Analysis of Multimodal Single-Cell Data. *Cell* **2021**, *184* (13), 3573-3587.e29.